



**AFRL-RX-WP-TR-2008**

**DEVELOPMENT OF A HIGH TEMPERATURE SENSOR  
BASED ON TRANSFORMATION-INDUCED  
RESISTIVITY  
PHASE II**

**Pavel Mogilevsky and Peter Nagy**

**UES, Inc.  
University of Cincinnati**

**February 2010**

**Final Report**

**This is a Small Business Innovation Research (STTR) Phase II Report**

**“Distribution Statement A, Approved for public release; distribution is unlimited.”**

**AIR FORCE RESEARCH LABORATORY  
AFOSR/PK 875 North Randolph Street Suite 325 Room 3112  
Arlington VA 22203**

REPORT DOCUMENTATION PAGE				Form Approved OMB No. 0704-0188	
Public reporting burden for this collection of information is estimated to average 1 hour per response, including the time for reviewing instructions, searching existing data sources, gathering and maintaining the data needed, and completing and reviewing this collection of information. Send comments regarding this burden estimate or any other aspect of this collection of information, including suggestions for reducing this burden to Department of Defense, Washington Headquarters Services, Directorate for Information Operations and Reports (0704-0188), 1215 Jefferson Davis Highway, Suite 1204, Arlington, VA 22202-4302. Respondents should be aware that notwithstanding any other provision of law, no person shall be subject to any penalty for failing to comply with a collection of information if it does not display a currently valid OMB control number. <b>PLEASE DO NOT RETURN YOUR FORM TO THE ABOVE ADDRESS.</b>					
1. REPORT DATE (DD-MM-YYYY) <b>February 2010</b>		2. REPORT TYPE <b>Final</b>		3. DATES COVERED (From - To) <b>15 November 2007-14 November 2010</b>	
4. TITLE AND SUBTITLE <b>DEVELOPMENT OF A HIGH TEMPERATURE SENSOR BASED ON TRANSFORMATION-INDUCED RESISTIVITY CHANGES IN ORDERED ALLOYS</b>				5a. CONTRACT NUMBER <b>FA9550-08-C-0040</b>	
				5b. GRANT NUMBER	
				5c. PROGRAM ELEMENT NUMBER	
6. AUTHOR(S)  <b>Pavel Mogilevsky and Peter Nagy</b>				5d. PROJECT NUMBER	
				5e. TASK NUMBER	
				5f. WORK UNIT NUMBER	
7. PERFORMING ORGANIZATION NAME(S) AND ADDRESS(ES)  <b>UES, Inc. 4401 Dayton-Xenia Road Dayton, OH 45432-1894</b>				8. PERFORMING ORGANIZATION REPORT NUMBER	
9. SPONSORING / MONITORING AGENCY NAME(S) AND ADDRESS(ES) <b>Air Force Research Laboratory AFOSR/NA 875 North Randolph Street Suite 325, Room 3112 Arlington, VA 22203</b>				10. SPONSOR/MONITOR'S ACRONYM(S)  <b>AFOSR/PKR2</b>	
				11. SPONSOR/MONITOR'S REPORT NUMBER(S)	
12. DISTRIBUTION / AVAILABILITY STATEMENT  <b>Approved for Public release; distribution is unlimited</b>					
13. SUPPLEMENTARY NOTES <b>This is a Small Business Innovation Research (STTR) Phase II Report. This document has color content</b>					
14. ABSTRACT: <b>A thermal history sensor based on variations in physical properties accompanying microstructural changes in Ni-Ni3Al-based alloys has been demonstrated. The operation of such sensor is based on the established correlation between microhardness and/or electrical resistivity, and the material damage parameter, expressed in the form of Larson-Miller Parameter (LMP). From the characteristic LMP vs. property plot for the particular alloy, one can read the value of LMP and get a measure of the incurred material damage. Knowing the exposure time, the equivalent temperature can be calculated. Furthermore, it has been demonstrated that with a sensor comprised of two different alloys, the equivalent temperature and duration of the thermal exposures can be extracted independently from the microhardness data. The key attribute to extend this approach to a practical application is structural and compositional homogeneity of the sensor alloys. A process that yields such homogeneity will need to be identified. Thin film deposition techniques, plasma spray coating methods, laser deposition followed by well defined heat treatment are some processes that are suggested. Multiple sensors with varying chemistries and heat treatments will further improve the accuracy by reducing the effect of measurement errors and eliminating multiple possible solutions for a given sensor read-out.</b>					
15. SUBJECT TERMS <b>High temperature sensor ,Thermal history, Superalloys, Phase transformation, Larson-Miller Parameter Material damage ,Electrical resistivity, Microhardness</b>					
16. SECURITY CLASSIFICATION OF:			17. LIMITATION OF ABSTRACT	18. NUMBER OF PAGES	19a. NAME OF RESPONSIBLE PERSON
a. REPORT	b. ABSTRACT	c. THIS PAGE			<b>Dr. Joan Fuller</b>
<b>Unclassified</b>	<b>Unclassified</b>	<b>Unclassified</b>	<b>SAR</b>	<b>70</b>	19b. TELEPHONE NUMBER (include area code) <b>703-696-7236</b>

## Contents

1.0	INTRODUCTION .....	1
2.0	RESULTS AND DISCUSSION .....	2
2.1.1.	Concept of Alloy Development .....	2
2.1.2.	Alloy Selection .....	4
2.1.3.	Resistivity Measurements .....	9
2.2.1.	Alloy Preparation and Heat Treatment .....	11
2.2.2.	Microstructural Analysis.....	13
2.2.3.	In-Situ High temperature Resistivity Measurements of Ar-Cooled Samples .....	17
2.2.4.	Room Temperature Resistivity Measurements Of Water Quenched And Aged Alloys .....	22
2.2.5.	Microhardness Measurements .....	38
2.2.6.	Thermal History Sensor Development.....	52
2.2.7.	In Situ Aging and Room Temperature Resistivity Measurements Of Water Quenched Alloys .....	61
3.	CONCLUSIONS AND SUMMARY .....	67
	REFERENCES .....	69

## LIST OF FIGURES

Figure 1: Pandat-Calculated Section of the Ni-Al-2.5at%Ti Phase Diagram .....	4
Figure 2. Kinetics of $\gamma'$ Precipitation During Continuous Cooling of Ni-Al Alloys as a Function of Cooling Rate [7] .....	6
Figure 3: Kinetics of Isothermal $\gamma'$ Precipitation in 80.5 Ni-5.2 Al-14.2 Cr (at.%) Alloy at 600°C (after [8]).....	6
Figure 4: Composition Selection in the Ni-Al-Ti System.....	8
Figure 5: Schematics of Alternating Current Potential Drop (ACPD, left) and Eddy Current Conductivity (ECC, right) Measurements.....	11
Figure 6: (a) Furnace for the Heat Treatment and Forced Ar Cooling; (b) Temperature Profiles in the Hot Zone and in the Forced Ar Cooling Zone of the Furnace .....	13
Figure 7: XRD spectra of Samples Annealed at and Ar-Cooled from 1220°C.....	14
Figure 8: Examples of the EDX Spectra from Samples A2 (left) and A6 (right) .....	14
Figure 9: SEM Images of Sample A6 (Ni-Al-2.5%Ti), Ar cooled from 1220°C: Core (left) and Surface (right) .....	15
Figure 10: SEM Images of the A3 Alloy Water Quenched (a) and Aged 700°C, 2 hours (b). .....	16
Figure 11: Absolute Resistivity of Samples A1 – A6 During 24-hour Thermal Exposure at Three Different Temperatures.....	18
Figure 12: Low-Temperature Processed (Normalized) Resistivity of Samples A1 – A6 During 24-hour Thermal Exposure at Three Different Temperatures .....	19
Figure 13: Examples of Full-Range Absolute Resistivity of Samples A1 and A4 During 24-hour Thermal Exposure at 800°C .....	20
Figure 14. Examples of XRD Spectra of Samples After In-Situ Resistivity Measurements .....	22
Figure 15: Magnetic Susceptibility of A1, A2, A3 And Rene88 Specimens .....	26
Figure 16: Room Temperature Resistivity ( $\mu\Omega\text{m}$ ) Of Samples A1-A3 and A4-A6 Water Quenched From 1220°C and Aged At 700°C For Different Times. The Samples That Exhibited Most Inhomogeneity Are Indicated.....	27
Figure 17: Room Temperature Resistivity ( $\mu\Omega\text{m}$ ) of Commercial IN-718, Rene88, and LSHR Aged At 700°C For Different Times .....	28
Figure 18: Absolute Resistivity Measurements on Samples A1-A4, IN718, Rene88 and LSHR For The Top (Medium Blue) And Bottom (Dark Blue) Values Separately (Top Chart), and The Average Value With Uncertainty Bars (Bottom Chart) .....	30
Figure 19: Conductivity Difference between Top and Bottom Surfaces of A3 and Rene88 Materials .....	30
Figure 20: Eddy Current Conductivity Images For A3m, A3k and Rene88 R4 Specimens .....	31
Figure 21: Resistance Ratio Variation with Aspect Ratio For Samples A1-A6 And Commercial Alloys IN718, Rene88, And LSHR (For Samples Shown In Figure 16 And Figure 17).....	32
Figure 22: Normalized Resistivity And The Resistance Ratio Variation With Aspect Ratio For Sets Of 5 Specimens For Alloys A3, A5, And Rene 88 Aged At 700°C For Different Times .....	34
Figure 23: Typical Dependence of Microhardness of Ni-Based Superalloy on Aging Time .....	39
Figure 24: Vickers Microhardness Values for Alloys A3 and A5 Aged At 700°C For Different Times .....	40
Figure 25: Vickers Microhardness Values for Rene 88 Alloy Aged at 700°C for 4 Hours Measured at Different Locations from the Edge.....	41
Figure 26: Vickers Microhardness Values for Alloys A1, A2, and A3 Aged at 700°C for Various Times.....	42
Figure 27: Vickers Microhardness Values for Alloys A4, A5, and A6 Aged At 700°C for Various Times.....	43
Figure 28: Initial Drop Of Vickers Microhardness Values for Water Quenched Alloys A4, A5, and A6 Aged At 700°C for 30 Minutes as A Function of Composition .....	43
Figure 29: Vickers Microhardness Values for Water Quenched Alloys A4, A5, and A6 Aged At 700°C For 30 Minutes As A Function Of Equilibrium Weight Fraction of $\gamma''$ .....	44
Figure 30: Vickers Microhardness Of Rene88 DP After Heat Treatments At 800°C, 850°C, and 900°C .....	47
Figure 31: Vickers Microhardness Of Rene88 DP In As-Received Condition .....	47
Figure 32: Vickers Microhardness of Rene88 Solutionized At Subsolvus Temperature after Aging at 700°C and 800°C .....	48

<b>Figure 33: Vickers Microhardness Of Rene88 Solutionized At Supersolvus Temperature after Aging At 700°C. The Data for Subsolvus Treatment Is Added For Comparison .....</b>	<b>49</b>
<b>Figure 34: Vickers Microhardness IN718 Alloy Solutionized at Subsolvus Temperature after Aging at 550°C, 650°C and 750°C .....</b>	<b>50</b>
<b>Figure 35: Vickers Microhardness IN718 Alloy Solutionized at Supersolvus Temperature after Aging at 550°C, 650°C and 750°C.....</b>	<b>51</b>
<b>Figure 36: Correlation Between Microhardness and Electrical Resistivity of IN718 After Aging at 700°C.....</b>	<b>52</b>
<b>Figure 37: Vickers Microhardness of Alloy A1-i After Aging at 600°C, 700°C, and 800°C .....</b>	<b>53</b>
<b>Figure 38: Vickers Microhardness Of Alloy A4-i After Aging At 600°C, 700°C, and 800°C .....</b>	<b>54</b>
<b>Figure 39: Vickers Microhardness Of Alloy A5-i After Aging At 600°C, 700°C, and 800°C .....</b>	<b>55</b>
<b>Figure 40: Relative Microhardness Of Alloys A1-i, A4-i, and A5-i After various Thermal Exposures between 600°C and 800°C.....</b>	<b>Error! Bookmark not defined.</b>
<b>Figure 41: LMP vs. Microhardness Plots Of Alloys A1-i and A5-i After various Thermal Exposures between 600°C and 800°C.....</b>	<b>58</b>
<b>Figure 42: Evaluation of Thermal Exposure From The Microhardness Of Alloys A1-i and A5-I Using Larsen-Miller Parameter .....</b>	<b>59</b>
<b>Figure 43: LMP vs. Microhardness Plots for IN-718 Alloy After various Thermal Exposures between 550°C and 750°C .....</b>	<b>60</b>
<b>Figure 44: Normalized Room Temperature Resistance of Alloys A1i, A2i, A4i and A5i After Thermal Cycling at 600°C, 700°C, and 800°C .....</b>	<b>62</b>
<b>Figure 45: Average Normalized Average Room Temperature Resistivity of Alloys A1i, A2i, A4i and A5i vs. Cycle Number at 600°C, 700°C, and 800°C.....</b>	<b>64</b>

## LIST OF TABLES

<b>Table 1: Nominal Composition of Alloys in Weight and Atomic %.....</b>	<b>9</b>
<b>Table 2: Composition of the A6 Alloy Forced Ar Cooled from 1220°C.....</b>	<b>16</b>
<b>Table 3: Oxidation ratings of the samples after in-situ resistivity measurements.....</b>	<b>21</b>
<b>Table 4: A1 Specimen Dimensions And Heat Treatment Parameters .....</b>	<b>23</b>
<b>Table 5: A2 Specimen Dimension And Heat Treatment Parameters.....</b>	<b>23</b>
<b>Table 6: A3 Specimen Dimensions And Heat Treatment Parameters .....</b>	<b>23</b>
<b>Table 7: A4 Specimen Dimensions And Heat Treatment Parameters .....</b>	<b>24</b>
<b>Table 8: A5 Specimen Dimensions And Heat Treatment Parameters .....</b>	<b>24</b>
<b>Table 9: A6 Specimen Dimensions And Heat Treatment Parameters .....</b>	<b>24</b>
<b>Table 10: Rene88 Specimen Dimensions And Heat Treatment Parameters .....</b>	<b>25</b>
<b>Table 11: Equivalent Ferrite content in A4 specimens.....</b>	<b>25</b>
<b>Table 12: Equivalent Ferrite content in A5 specimens.....</b>	<b>25</b>
<b>Table 13: Equivalent Ferrite content in A6 specimens.....</b>	<b>26</b>
<b>Table 14: Empirical LMP Parameters A and B, and Linearization Parameters C and D for Alloys A1-i and A5-i.....</b>	<b>58</b>

## 1.0 INTRODUCTION

Aerospace and aircraft industries have numerous instances of critical components functioning in harsh thermal environments, where sensors are required to help monitor the health of the component(s) and thus reduce the cost of maintenance and minimize the risks of operating the vehicle(s). The continuous demand for increasing the operational efficiency necessitates components to perform at or close to their limiting temperatures. Failures often occur as a result of material degradation with time at service or from unexpected thermal fluctuations. The remaining useful life of a component depends on the extent of degradation during service. There is an increasing need to be able to know the level of degradation of a component and remaining life. It is anticipated that this area of challenging technology will progress steadily through innovative solutions and a systematic understanding of the capabilities of sensors [1-6].

The degradation of high temperature materials during service is time and temperature dependent (although the actual failure may appear sudden). Many metallurgical phenomena, such as phase transformations, are also time and temperature dependant (the temperature dependence is typically exponential, while the time dependence is more gradual).

It was proposed in this project to use an empirical parameter similar to Larson-Miller parameter (LMP) used for correlation of creep stress with temperature and time to failure as a parameter describing accumulated damage in Ni-based superalloys. Thus if one can measure a property (or properties) of a material that is sensitive to the phase transformation it is undergoing and correlate it to a Larson-Miller type parameter, one can evaluate the thermal history of the material and use that to predict the degradation of the component of interest.

In this work it was proposed to explore the changes in resistivity and microhardness accompanying a phase transformation, specifically, an order-disorder transformation in Ni-based superalloys, to record the thermal history experienced in service. For such an application, alloys that are already in design or use are attractive since their stability in the operating conditions is

already established. For example, Ni<sub>3</sub>Al alloys suitably modified with ternary alloying additions are attractive as a sensor material; Ni<sub>3</sub>Al is a major component of the superalloys. NiAl is often used as bond-coat in high-temperature superalloys used in turbine blades of aircraft engines. Microhardness is very sensitive to the alloy phase composition and microstructure, and as such is a property that can be used to monitor the thermal history. Furthermore, it is directly related to the mechanical properties (and thus the “health”) of the alloy. Resistivity is also very sensitive to phase composition and microstructure, and its changes can be monitored with high precision by electromagnetic methods which allow the contactless measurement of electrical resistivity. Among them, eddy current spectroscopy (ECS) is a robust method with an established track record as a non-contact measurement in a range of engineering materials. In addition, it is adaptable to long-term in-situ field inspection, at least in aerospace materials and components, without the need for electro-mechanical or other types of transducers or sensors. It is expected that this technique will also work well at high operational temperatures.

## **2.0 RESULTS AND DISCUSSION**

### **2.1. Experimental Approach**

#### **2.1.1. Concept of Alloy Development**

During Phase 1 of this project, it was established that microstructural changes in Ni-Al alloys induced by thermal exposure results in significant variations of the electrical properties, in particular electrical resistivity. Thus, under certain conditions, measurements of the electrical resistivity can be used to evaluate the cumulative thermal exposure and provide data that can be correlated with the degree of degradation of an engine component exposed to the same thermal history. However, this concept requires that the microstructural changes that occur in the sensor are irreversible under the conditions to which the sensor can be potentially exposed. To illustrate this point, an alloy that is fully  $\gamma'$  (such as Ni<sub>3</sub>Al-Ta alloy (NAT) with the composition of Ni-21.5at%Al-1.3at%Ta-1.1at%Fe-0.1at%Cr investigated during Phase 1) cannot be a suitable sensor, since in this alloy the resistivity changes are associated exclusively with the variation in the ordering parameter and are therefore reversible over the temperature range that an engine



component can see in service. Therefore, the resistivity of a sensor that was exposed to an unusually high temperature during service would gradually return to normal values during subsequent service at normal operating conditions. Such a sensor, therefore, might not properly record the exposure to temperature overshoot, or, in other words, the sensor's "memory" of such an event might be even completely erased. In that respect, the sensor would function as no more than a temperature probe (not unlike, but more difficult to use than, a thermocouple) that can read the current temperature but without the ability to retain "memory" of the thermal history

On the contrary, under certain conditions an alloy with a composition in the two phase  $\gamma/\gamma'$  field can be used as a sensor with memory. As an example, consider the alloy with the composition ~0.15 at.% Al in **Figure 1**. If such an alloy is homogenized above the solutionizing temperature (~1300°C) and then rapidly quenched retaining it single  $\gamma$  microstructure, the predominant microstructural change during subsequent thermal exposure will be precipitation of primary  $\gamma'$  phase with the attendant change in electrical resistivity. So long as the alloy is not exposed to temperatures above the solutionizing temperature, the precipitation of  $\gamma'$  will not be reversed. Minor variations in the equilibrium  $\gamma/\gamma'$  ratio that do occur with temperature may likely be ignored so long as the sensor is still relatively far from the equilibrium (continuous precipitation of  $\gamma'$  dominates the microstructure development).

Thus, the suggested concept of alloy design is to work with alloys having equilibrium  $\gamma/\gamma'$  compositions. The compositions should be chosen in such a way that the solutionizing temperature is guaranteed to considerably exceed the highest temperature that the sensor can see during normal service and even under abnormal, yet non-catastrophic conditions. The new sensor should be quenched from temperatures above the solutionizing temperature, preferably retaining single  $\gamma$  phase composition. Heat exposure will cause  $\gamma'$  precipitation with attendant change in conductivity. Sensor should be used far from equilibrium when precipitation of primary  $\gamma'$  is the main process. When "too close" to equilibrium, the sensor should be replaced and can be recycled by re-annealing and quenching.

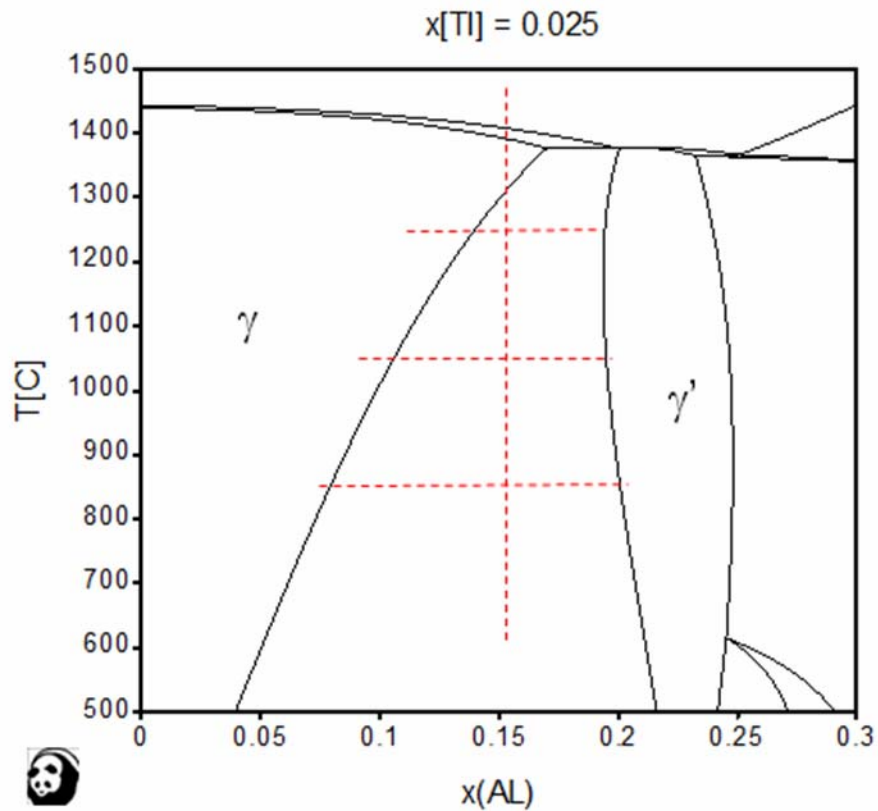


**Figure 1: Pandat-Calculated Section of the Ni-Al-2.5at%Ti Phase Diagram**

### 2.1.2. Alloy Selection

Based on the discussion in the previous section, two main factors should be taken into account when choosing the alloy compositions. First, the temperature range of interest to be monitored needs to be established. In consultations with the government project monitors, it was decided that at this stage of the project, the temperature range of interest is between 500°C to 800°C. Second, the compositions of the alloys need to be chosen in such a way that for the temperature range of interest, the kinetics of  $\gamma'$  precipitation from quenched  $\gamma$  is such that useful life times of the sensor can be achieved. Once again, in consultation with the government project monitors, it was established that the goal for the useful life of the sensor should be at least 10-20 hours of operation.

Unfortunately, despite large amount of research on microstructural evolution of Ni-based superalloys, very little study has been aimed at the kinetics of the  $\gamma'$  precipitation. The reason for this is that Ni-based superalloys are typically used under phase equilibrium conditions. Indeed, since these materials are designed for high temperature applications, they obviously cannot be expected to deliver stable performance under strongly non-equilibrium phase compositions. Instead, the primary subject of interest in their research is the morphological evolution (i.e., the size distribution, shape, and coherency of  $\gamma'$  precipitates), since these factors are primary responsible for the mechanical properties of the alloy. Among the few studies devoted to the kinetics of the  $\gamma'$  precipitation (as opposed to the kinetics of the coarsening of fully precipitated  $\gamma'$ ), Jackson et al. [7] studied the kinetics in Ni-Al alloys during continuous cooling as a function of the alloy composition and the cooling rate (**Figure 2**). The study demonstrated that the precipitation rate is strongly dependent on the Al content, but only weakly influenced by the cooling rate. Sudbrack et al. investigated the kinetics of isothermal  $\gamma'$  precipitation in 80.5 Ni-5.2 Al-14.2 Cr (at.%) alloy at 600°C [8]. This study demonstrated the precipitation kinetics that was sluggish enough for a potential sensor to function hundreds of hours (**Figure 3**). However, the study was conducted at a single temperature, such that no projections could be made for the rate of precipitation at higher temperatures.

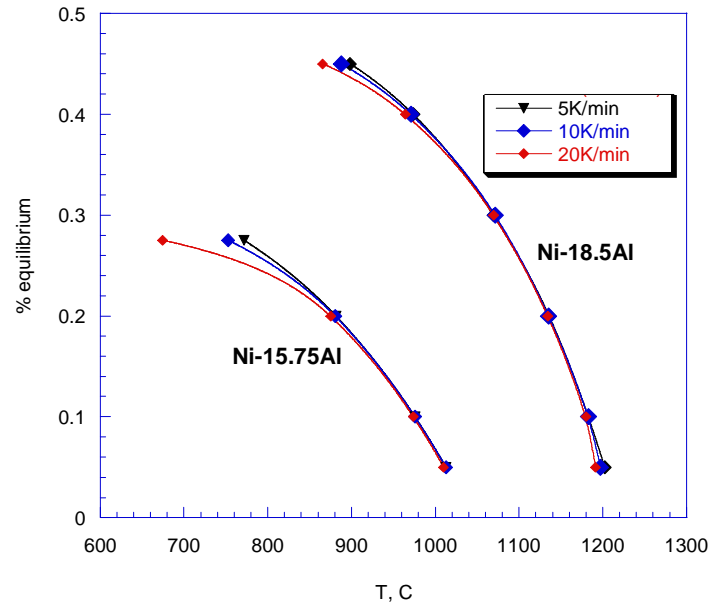


**Figure 2. Kinetics of  $\gamma'$  Precipitation During Continuous Cooling of Ni-Al Alloys as a Function of Cooling Rate [7]**

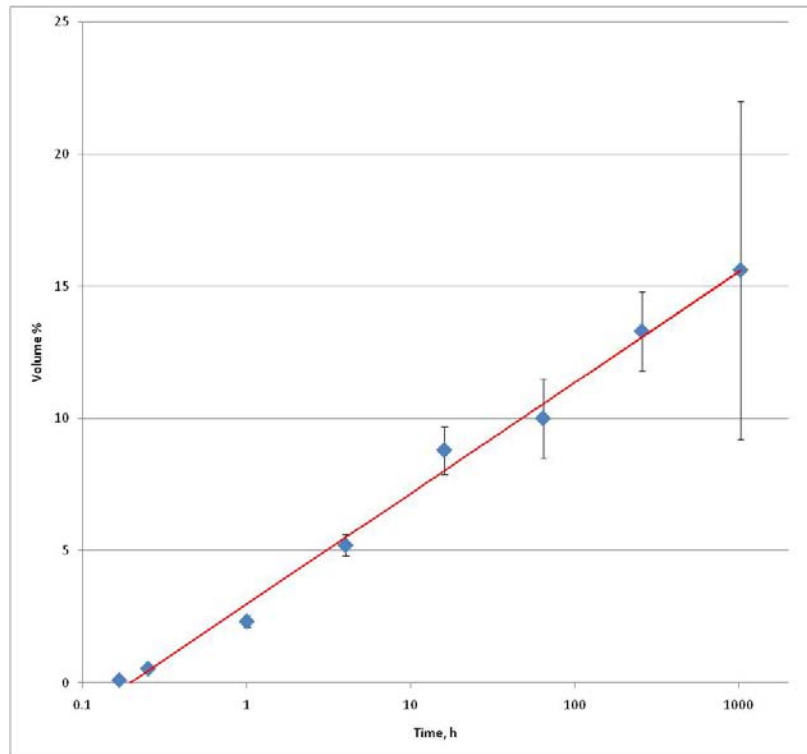


**Figure 3: Kinetics of Isothermal  $\gamma'$  Precipitation in 80.5 Ni-5.2 Al-14.2 Cr (at.%) Alloy at 600°C (after [8])**

In general, the selection of the alloy compositions should be based on the following considerations. As the data Jackson et al. demonstrate, in binary Ni-Al alloys, the precipitation kinetics depend strongly on the Al content (**Figure 2**). The addition of the alloying elements may alter the precipitation kinetics in a number of ways. The alloying elements that stabilize  $\gamma'$  may speed up its precipitation kinetics through increasing the transformation thermodynamic driving force and increasing the nucleation rate. The alloying elements that stabilize  $\gamma$  may have the opposite effect. On the other hand, those elements that partition preferentially to either  $\gamma$  or  $\gamma'$  may slow down the transformation, as considerable diffusion of such elements that would have to occur during  $\gamma'$  precipitation may become a rate controlling factor. Elements that partition evenly between  $\gamma$  and  $\gamma'$  would not require long range diffusion during transformation and therefore would not affect the precipitation kinetics through this mechanism. In addition, common alloying elements can be preferentially incorporated either into the Al sublattice (Nb, V, W, and Ti) or Ni sublattice (Co) of the ordered  $\text{Ni}_3\text{Al}$  phase, or be evenly incorporated in both (Fe, Cr). Furthermore, the precipitation kinetics might be affected by the  $\gamma/\gamma'$  interfacial energy and the coherency of the interface, which in turn depends greatly on the alloy composition.

Many of these factors (such as the thermodynamic phase stability and the effect of the composition on the coherency of the  $\gamma'/\gamma'$  interface) are known from the extensive available research or can be calculated using the existing thermodynamic data (in this work, we use the Pandat software and database for this purpose). However, given the lack of literature data on the kinetics of  $\gamma'$  precipitation in Ni-Al alloys in the temperature range of interest, and of the general understanding of the synergy between the above factors affecting it, it was decided to first investigate two families of model ternary alloys from Ni-Al-Ti and Ni-Al-Cr systems. Based on the previous experience during the Phase 1 project, we chose alloys with either 2.5 at.% Ti and 5at.% Cr. For each alloying element, 3 compositions with varying Ni/Al ratio were selected. The actual Ni/Al ratios were selected based on the following considerations. As mentioned above, the operational temperature range of 500 to 900°C was suggested for the sensor development in consultations with the government project monitors. The sensor is supposed to be used at temperatures below the solutionizing temperature ( $\gamma/\gamma'$  phase boundary). Thus, it was decided for

consistency to chose the alloys with the solutionizing temperatures of 900, 1050, and 1200°C. Those were determined using the Pandat-calculated sections of the Ni-Al-Ti and Ni-Al-Cr phase diagram. An example of the phase diagram section and the compositions selected in the Ni-Al-Ti system is shown in **Figure 4**, and the summary of the composition of the six alloys selected is given in Table 1.

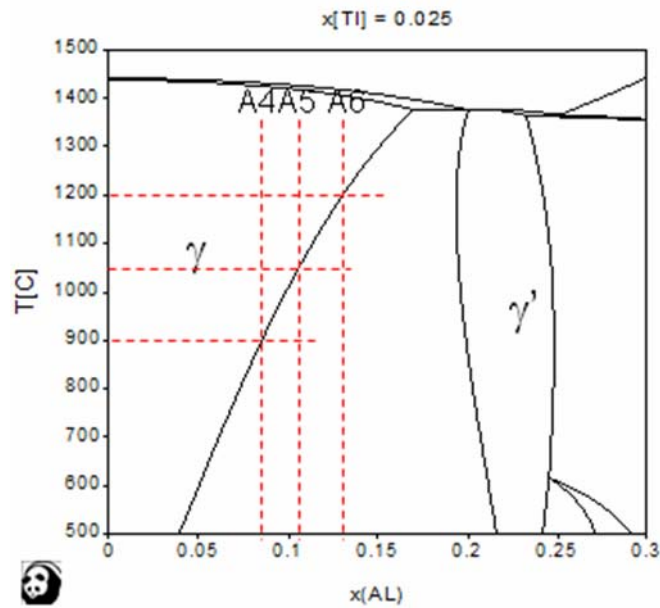


**Figure 4: Composition Selection in the Ni-Al-Ti System**

**Table 1: Nominal Composition of Alloys in Weight and Atomic %**

	Ni		Al		Cr (5 at.%)	Ti (2.5 at.%)	$\gamma'$ solvus, T°C	HT1 Time @ 1220°C Hrs	HT2 Time @ 1220°C Hrs
	wt.%	at.%	wt.%	at.%	wt.%	wt.%			
A1	89.58	83.5	5.67	11.5	4.75	--	900	58	2
A2	88.40	81.4	6.79	13.6	4.81	--	1050	58	2
A3	86.78	78.6	8.32	16.4	4.89	--	1200	58	2
A4	93.74	89.0	4.12	8.5	--	2.15	900	58	2
A5	92.68	87.0	5.14	10.5	--	2.17	1050	58	2
A6	91.28	84.4	6.51	13.1	--	2.21	1200	58	2

One of the strategies for sensor development proposed in this program was to use the sensor materials to alloys that are similar or identical to the materials used in service as well. Accordingly, in addition to alloys A1-A6, samples from 3 commercial ( $\gamma + \gamma'$ ) superalloys IN-718, Rene88, and LSHR were also prepared in a similar manner.

### 2.1.3. Resistivity Measurements

The overall aim of this project was to demonstrate the feasibility of high-temperature sensors based on microstructural changes caused by phase transformations. It was shown previously (Phase 1) that the accompanying changes in various physical properties can be measured using existing nondestructive evaluation (NDE) instrumentation. However, microstructural evolution is rather difficult to detect in the early stages and even more difficult to reliably quantify using conventional NDE methods. The two most important issues are the (i) sensitivity and (ii) selectivity of different physical parameters and individual measurement techniques for microstructural evolution that is a function of both temperature and time. In this work two specialized nondestructive evaluation (NDE) techniques for assessing microstructural evolution

in nickel-based superalloys caused by thermal aging were used. The chosen approach was a multi-sensor method in which low-frequency alternating-current potential drop (ACPD) and high-frequency eddy current conductivity (ECC) methods were researched with the aim of identifying the most effective monitoring method. These techniques are either high-temperature in-situ monitoring or room-temperature post-exposure inspection technique that can be used to “read out” features of the past thermal history of the material. These methods were selected during Phase 1 of the project from a larger group of candidate technologies with established track record in nondestructive monitoring of environmentally-assisted degradation in nickel-base superalloys based on their unique adaptability to in-situ monitoring.

#### **2.1.3.1. Alternating Current Potential Drop (ACPD) Measurement**

The alternating current potential drop technique uses a pair of injection electrodes in combination with a pair of sensing electrodes to measure the complex electrical impedance of a conducting material (see Figure 5a). Generally, the frequency-dependence of the measured impedance provides valuable information on the electrical conductivity and magnetic permeability as well as their depth-dependence below the surface, which in turn can be exploited for nondestructively monitoring microstructural evolution. Galvanic coupling, usually through simple spring-loaded pins or spot-welded electrodes, assures that measurements can be done over a wide frequency range from a few tenths of Hz up to tenths of kHz. This method allows the selective assessment of reversible and irreversible temperature effects on the electric resistivity of the material. Using thermocouple wires as connectors, measurement of the dc potential drop without current injection allows parallel monitoring of the local temperature. This method can be used for in-situ resistivity measurements at temperature.

#### **2.1.3.2. Eddy Current Conductivity (ECC) Measurement**

The physical principle of eddy current spectroscopy is rather similar to that of ACPD, except that it uses an inductive coil to measure the complex electric impedance of a conducting material (Figure 5b). Instead of contacting electrodes, the electrical current is both induced and detected by magnetic means. Although the frequency range that can be covered by a single probe coil is usually limited to only one decade, the advantage of monitoring material variations in a non-contact manner often well compensates for this bandwidth limitation. With multiple probes,



ECC can be also extended over a very large frequency range from tens of Hertz to tens of MHz. The relevant yardstick that determines the penetration depth of electromagnetic inspection is the so-called skin-depth that is inversely proportional to the square root of frequency. By virtue of its higher operation frequency, ECC offers roughly one order of magnitude better sensitivity to near-surface variations in material properties than ACPD measurements, which can be exploited for selective monitoring of material degradation in very shallow surface layers.

In the current research, eddy current technique is used for room temperatures resistivity measurements. Room-temperature experiments, however, measure only the remnant, irreversible changes of resistivity and do not allow monitoring microstructural evolution during the often rather complex temperature history of the material. In order to understand how electric conductivity changes with temperature and time, we have to conduct in-situ monitoring throughout the whole heat cycle. Such high-temperature monitoring can be most easily achieved using the ACPD technique. Thus, in the present study, both techniques are used in a complimentary manner.

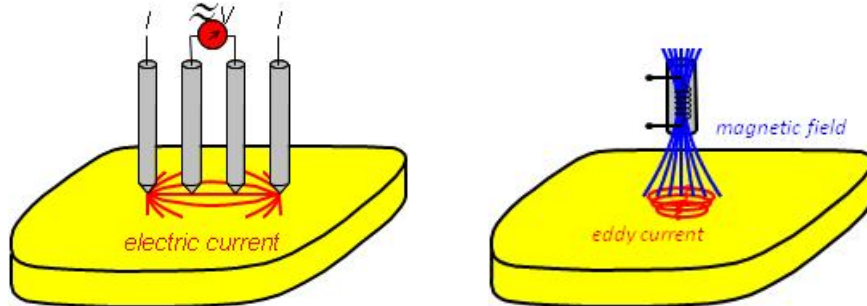


**Figure 5: Schematics of Alternating Current Potential Drop (ACPD, left) and Eddy Current Conductivity (ECC, right) Measurements**

## 2.2. Experimental Results

### 2.2.1. Alloy Preparation and Heat Treatment

The six alloys (compositions given in **Table 1**) were arc-melted under Ar, after which samples from these alloys were prepared for microstructural characterization and conductivity

measurements. All samples for microstructural characterization were approximately  $12 \times 12 \times 3$  mm in size and those for conductivity measurements were  $25 \times 6.5 \times 3$  mm in size. The samples were then homogenized by heat-treating them at  $1220^{\circ}\text{C}$  in Ar atmosphere. Based on the previous experience (Phase 1 of the project), extended homogenization time of 58 hours was chosen (heat treatment HT1 in Table 1).. The samples were furnace cooled and subjected to the XRD, SEM, and EDX analysis. Another solutionizing heat treatment at  $1220^{\circ}\text{C}$  for 2 hours followed by a rapid cooling using forced Ar (heat treatment HT2 in Table 1) was then conducted to produce samples retaining non-equilibrium  $\gamma'$  phase.

In order to conduct this heat treatment, a standard tube furnace was used in which the tube was offset from its normal central position to create a cooling area where the sample boat could be rapidly moved to from the hot zone and where Ar could be directed at the samples (**Figure 6a**). The temperature of the cooling zone during a  $1220^{\circ}\text{C}$  heat treatment was measured and determined to be  $\sim 430^{\circ}\text{C}$  (**Figure 6b**).

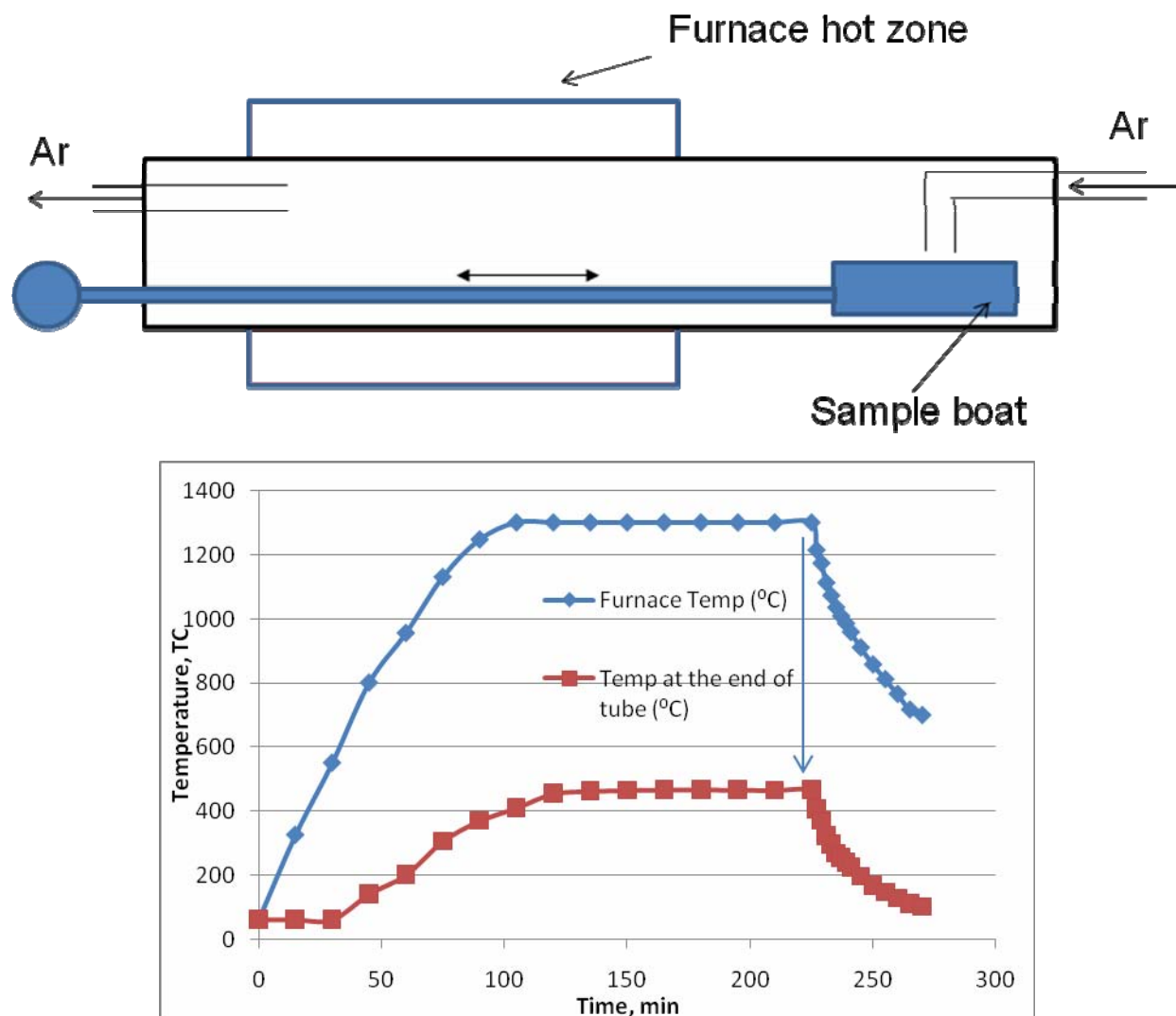


**Figure 6: (a) Furnace for the Heat Treatment and Forced Ar Cooling; (b) Temperature Profiles in the Hot Zone and in the Forced Ar Cooling Zone of the Furnace**

The forced Ar cooled samples were subjected to XRD, SEM, and EPMA analysis. Another set of samples was subjected to the identical heat treatment with the exception that the samples were water quenched instead of cooling with forced Ar.

### 2.2.2. Microstructural Analysis

X-ray diffraction of all alloys annealed at and Ar-cooled from 1220 $^{\circ}\text{C}$  showed them to be predominantly composed of the  $\gamma$  phase with only trace amount of  $\gamma'$  visible in the spectra from

sample A3. An example of diffraction pattern is shown in Figure 1 where all the peaks corresponding to the  $\gamma$  and  $\gamma'$  phases are indicated. EDX analysis of the homogenized and forced Ar cooled samples reveal expected elements, though an elevated O content was noticeable in sample A2 (Figure 8).

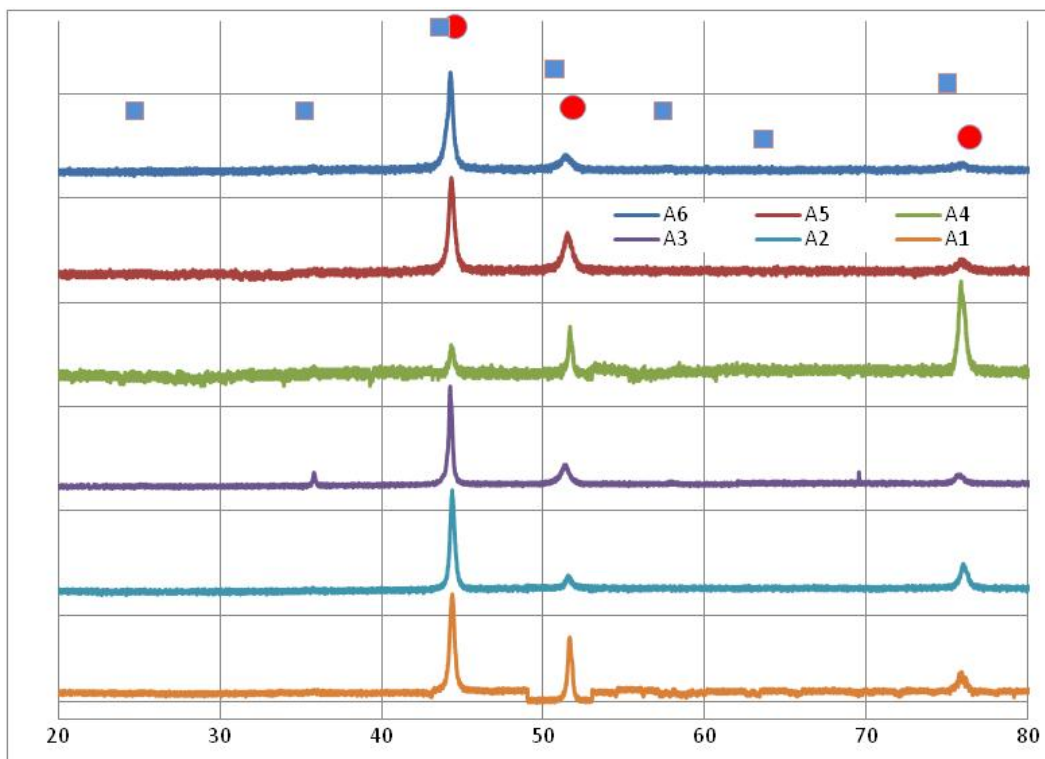


**Figure 7: XRD spectra of Samples Annealed at and Ar-Cooled from 1220°C**

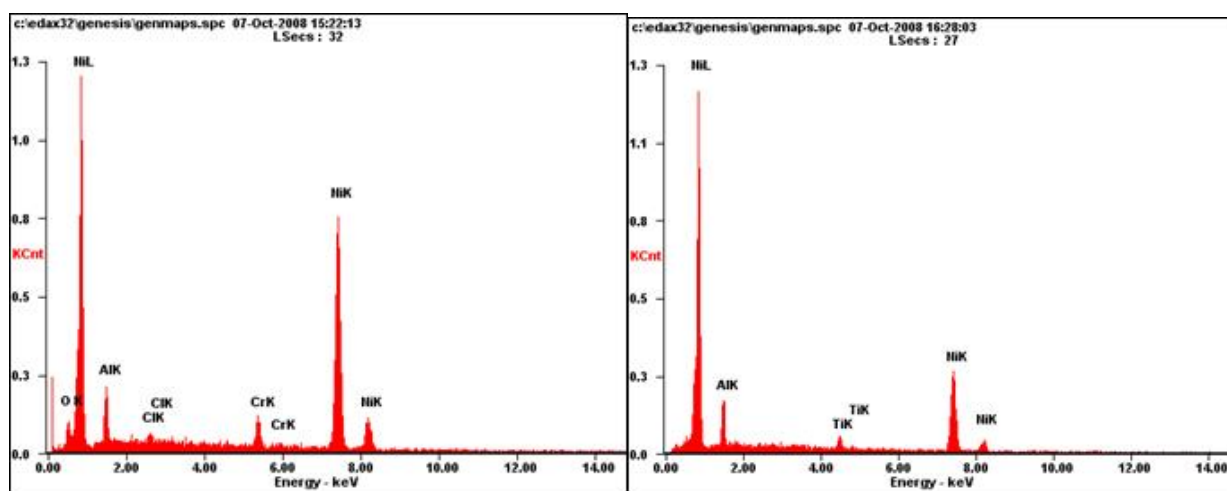


**Figure 8: Examples of the EDX Spectra from Samples A2 (left) and A6 (right)**

However, the SEM analysis of samples after forced Ar cooling demonstrated that, despite earlier encouraging XRD results that showed no  $\gamma'$  in the as-cooled material (Figure 7), the material indeed did contain a large fraction of  $\gamma'$  (Figure 9). The precipitates had a typical cuboid morphology in Ti containing samples (Figure 9). The average precipitate size was much smaller at the surface of the samples than in the core, consistent with higher cooling rates experienced at the surface. An example of the results of EDX analysis conducted on sample A6 is shown in Table 3. It shows that the general composition of the sample is close to the target composition, though it is somewhat richer in Ti. The compositions of both  $\gamma$  and  $\gamma'$  phases are close to those expected from the phase diagram calculations, with the Ti distribution coefficient between  $\gamma$  and  $\gamma'$  approximately 0.71. It should be noted that the small size of the precipitates makes accurate quantitative analysis of their composition impossible. Statistical analysis of the precipitates in the core of sample A6 based on the image analysis of the SEM pictures indicated the volume fraction of  $\gamma'$  precipitates approximately 46%, which is close to the equilibrium amount of approximately 50% (according to the phase diagram calculations performed using Pandat software).

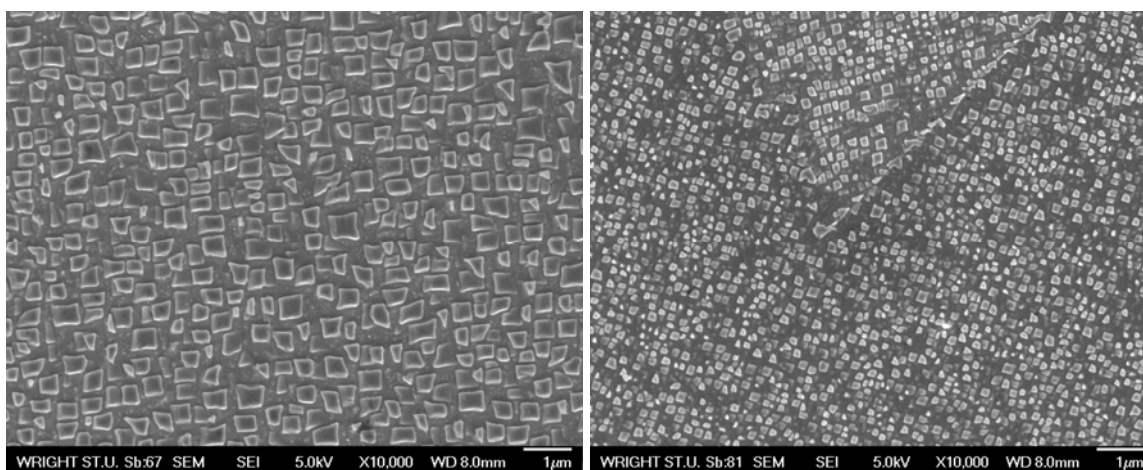


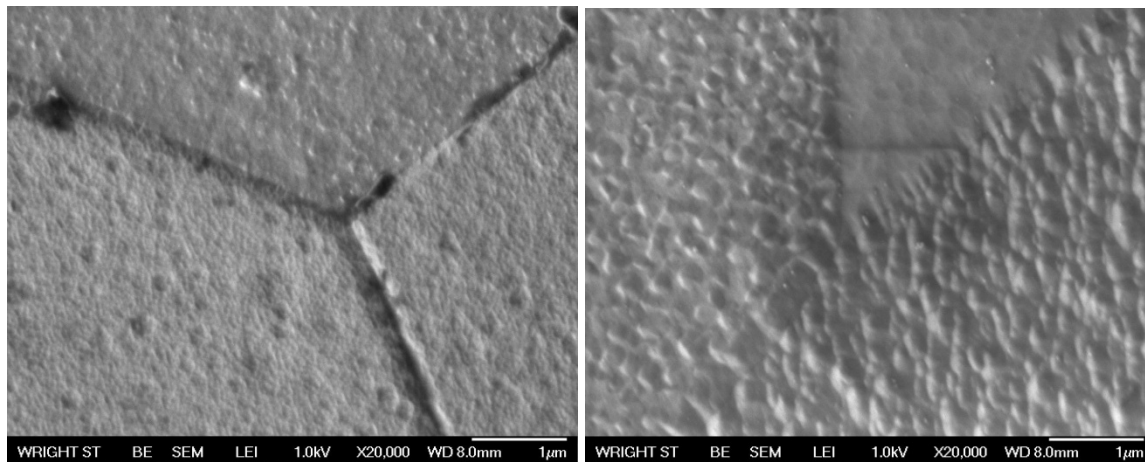
**Figure 9: SEM Images of Sample A6 (Ni-Al-2.5%Ti), Ar cooled from 1220C: Core (left) and Surface (right)**

**Table 2: Composition of the A6 Alloy Forced Ar Cooled from 1220°C.**

Element	Average		$\gamma'$		$\gamma$	
	Wt%	At%	Wt%	At%	Wt%	At%
AlK	7.3	14.5(13.1)	9.8	17.9(17)	6.6	13.2(13)
TiK	2.9	3.3(2.5)	3.1	3.4(4.1)	2.1	2.4(2.4)
NiK	89.8	82.2(84.4)	87.71	78.7(78)	91.3	84.4(84)

\* The numbers in red represent the values calculated using Pandat software. The numbers in blue represent the target average composition

It is not clear why XRD analysis failed to pick up such relatively large volume fraction of the  $\gamma'$  phase. The most likely reason is the high level of the residual stress present in the samples. Based on these results, however, it has become apparent that the forced Ar does not provide the cooling rate necessary to sufficiently suppress the precipitation of  $\gamma'$ . Therefore, samples for the room temperature resistivity measurements were water quenched to increase the cooling rate beyond what was achievable with forced Ar. The smallest specimen thickness suitable for eddy current measurements (2 mm) was chosen to minimize through thickness variation of the cooling rate. The quenched samples were then annealed at 700°C for various times to simulate continuous ageing and sent to the University of Cincinnati for room temperature resistivity measurements. **Figure 10** shows SEM images of the A3 alloy water quenched and aged 700°C, 2 hours.

**Figure 10: SEM Images of the A3 Alloy Water Quenched (a) and Aged 700°C, 2 hours (b).**

### **2.2.3. In-Situ High temperature Resistivity Measurements of Ar-Cooled Samples**

The in-situ resistivity measurements were performed on A1 through A6 specimens (see Table 1) that were forced Ar cooled from 1220°C to room temperature to continuously monitor the changes of resistivity in these samples during ageing at elevated temperatures. Based on the temperature range of interest, for the first runs it was decided to conduct isothermal measurements at 700°C, 800°C and 900°C. The samples were heated in a furnace under Ar flow, and the resistivity was measured using Linear Research Inc. AC Resistance Bridge (model LR-700) in the low-frequency ACPD (16 Hz) mode, Linear Research Inc. multiplexer (Model LR-720-8), and Stanford Research Systems thermocouple monitor (Model SR630). Specimens were heated to target temperatures at the maximum furnace power and then held at temperature for 24 hours, after which they were allowed to cool down in the furnace.

Figure 11 shows measured resistivity of samples A1 – A6 during 24-hour thermal exposure at three different temperatures. In this method, the measured absolute values depend on specimen geometry and electrode position and therefore do not represent absolute resistivity variations.

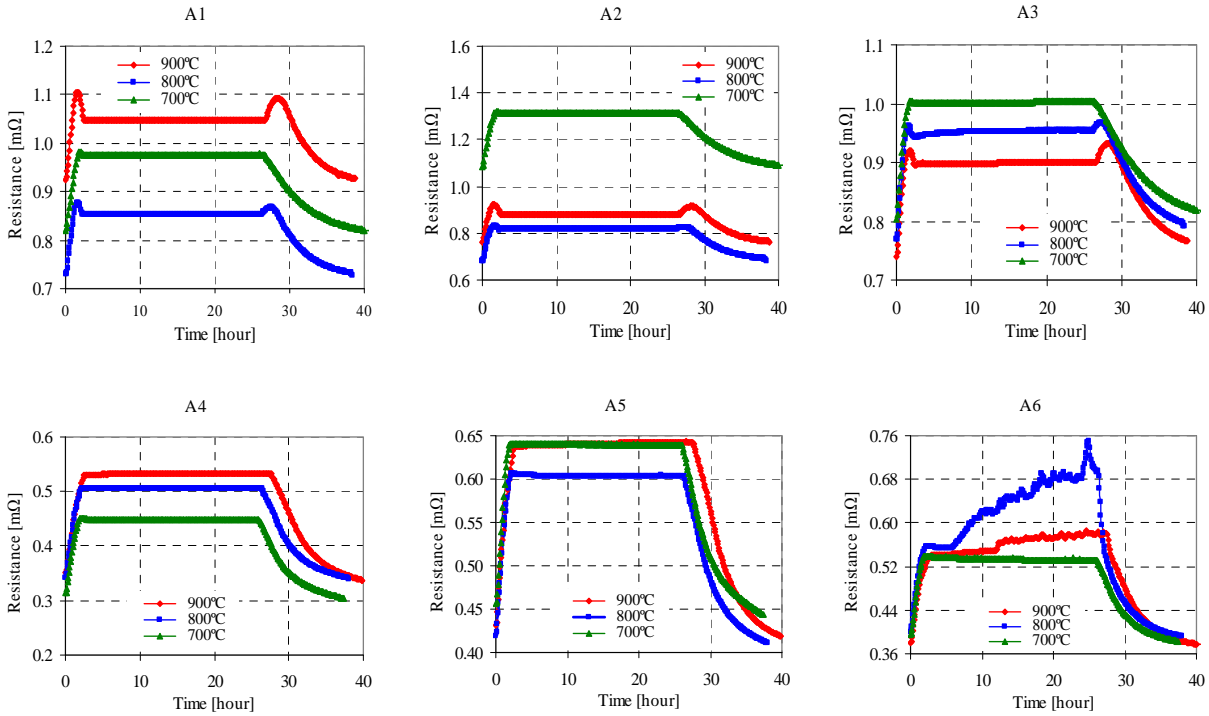


**Figure 11: Absolute Resistivity of Samples A1 – A6 During 24-hour Thermal Exposure at Three Different Temperatures.**

With the exception of sample A6, no resistivity changes are apparent during the 24 hour hold at temperature, indicating that any microstructural changes and attending irreversible changes of resistivity must have occurred during the heating segment. Moreover, the low-temperature processed (normalized) resistivity of samples A1 – A6 during the heating and cooling segments (Figure 12) indicate no temperature dependence of the residual resistivity for samples A1 and A2 with the net decrease of the resistivity after the heat treatment, while for the sample A3 the resistivity increased and depended on the peak temperature. The data in Figure 12 is zoomed in near room temperature range to illustrate the irreversible variation in resistivity. Black lines – heating phase, colored lines - cooling phase.



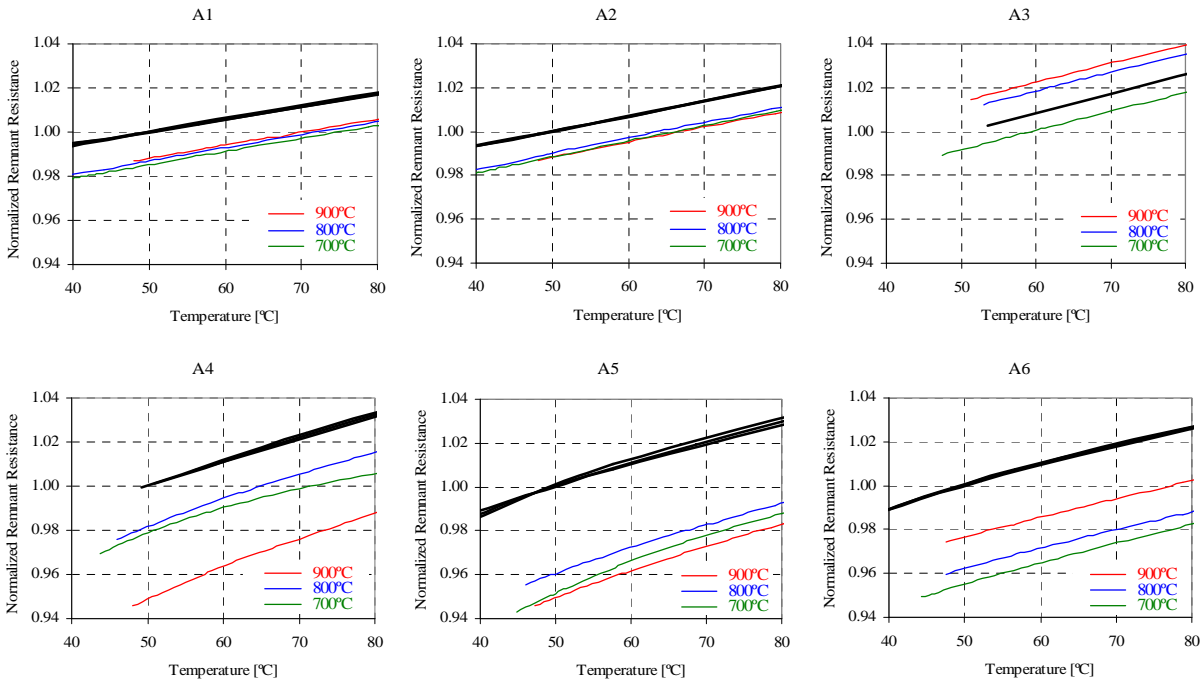


**Figure 12: Low-Temperature Processed (Normalized) Resistivity of Samples A1 – A6 During 24-hour Thermal Exposure at Three Different Temperatures**

For the Ti containing samples (samples A4-A6), the situation is different. All samples exhibited a substantial decrease in resistivity after the ageing heat treatment, and the extent of the resistivity decrease was dependent on the peak temperature (Figure 12). However, the effect was not consistent between samples with different Al content and with different peak temperatures. Thus, the irreversible resistivity change was the largest after 900°C heat treatment for samples A4 and A5, and after 700°C heat treatment for sample A6. This could be explained by some irregularity during the testing of sample A6, as this sample exhibited an unusual resistivity changes during the hold segment of the heat treatment (Figure 11). However, samples A4 and A5 also demonstrated irreversible resistivity changes inconsistent with peak temperature. Thus, while the largest irreversible resistivity change occurred after 900°C heat treatment for both samples, the smallest effect was observed not at 700°C, as could have been expected, but at 800°C.

Figure 13 shows examples of full-range absolute resistivity of samples A1 and A4 during 24-hour thermal exposure at 800°C. It demonstrates that in all samples reversible variation in resistivity due to temperature is pre-dominant and non-linear. In particular, the temperature dependence of resistivity for Cr containing samples is strongly non-linear with a maximum occurring at approximately 600°C. However, it should be noted that although the maximum resistivity occurred at 600°C, this phenomenon was only observed for runs to higher peak temperatures, such as 800°C and 900°C. No resistivity maximum was observed for runs to 700°C peak temperature. Less aggressive non-linearity was observed for Ti containing samples (Figure 13b).

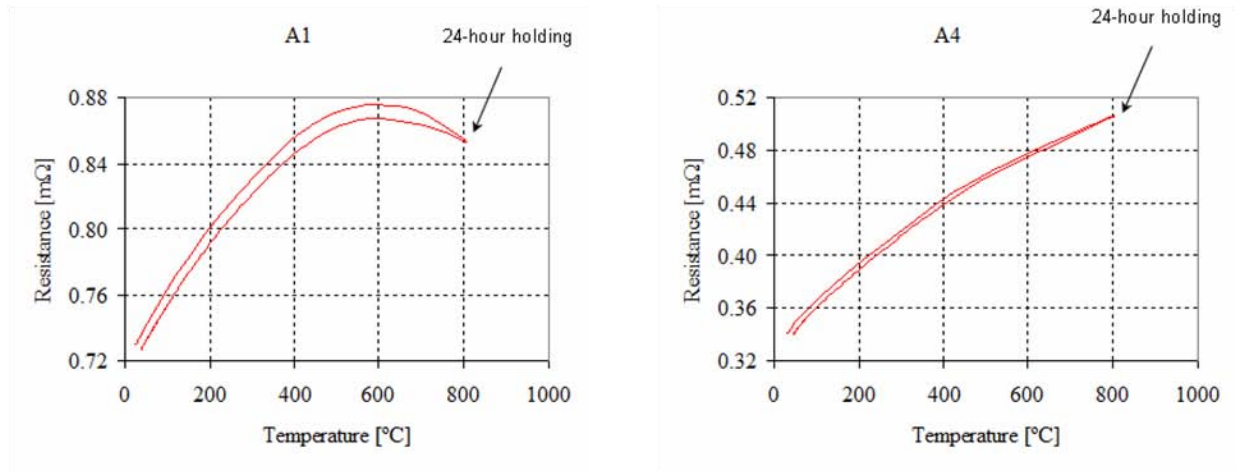


**Figure 13: Examples of Full-Range Absolute Resistivity of Samples A1 and A4 During 24-hour Thermal Exposure at 800°C**

Such complex response of resistivity of Ni-Al alloys to ageing can be understood if all the different factors affecting the resistivity of these alloys are considered. On one hand, the ordered  $\gamma'$  phase has higher resistivity than  $\gamma$ , and its precipitation should be expected to increase the total electrical resistivity. At the same time, the resistivity of  $\gamma$  phase increases sharply with the content of aluminum [9]. Precipitation of higher Al content  $\gamma'$  will decrease the Al content in  $\gamma$ , decreasing its resistivity. Thus, the temperature dependence of the resistivity in these alloys can be quite complex.

In addition to these intrinsic factors, the visual inspection of the samples after in-situ experiments demonstrated considerable surface oxidation of the samples. The degree of oxidation was rated based on the samples' appearance and is presented in Table 3. It shows that the oxidation extent generally increased at higher temperatures, though for Cr containing samples less oxidation was observed after runs to 800°C peak temperature than for the 700°C runs. The Ti containing samples were generally heavier oxidized than those with Cr.

**Table 3: Oxidation ratings of the samples after in-situ resistivity measurements.**

Alloying element	Alloy	700°C	800°C	900°C
Cr	A1	M	L	H
	A2	M	L	H
	A3	M-	L-	H
Ti	A4	M+	H+	H+
	A5	M+	H+	H++
	A6	M+	H+	H

Legend: L-Light Oxidation; M-Medium Oxidation; H-Heavy Oxidation; “-” lighter; “+” heavier

The XRD analysis conducted on the samples after in-situ resistivity measurements, both on the surface and the cross-sections of the samples indicated the presence of NiO, though the degree of oxidation varied (Figure 14). These results demonstrated that the current experimental set-up for in-situ resistivity measurements, based on box furnace flushed with Ar, is inadequate for long term experiments due to insufficient oxidation protection. A better design of the furnace used in these tests would be needed to resolve this issue. In addition, the current experimental set up does not allow the fast heating of the sample (heating ramp to temperatures of interest of ~2 hours at maximum power) and relies on relative rather absolute resistivity. It was therefore decided to conduct ageing heat treatments of samples utilizing the tube furnace with demonstrated capacity for long term heat treatment in Ar atmosphere and virtually no detectable

oxidation. Room temperature resistivity measurements would then be used for absolute room temperature measurements of irreversible changes in resistivity.

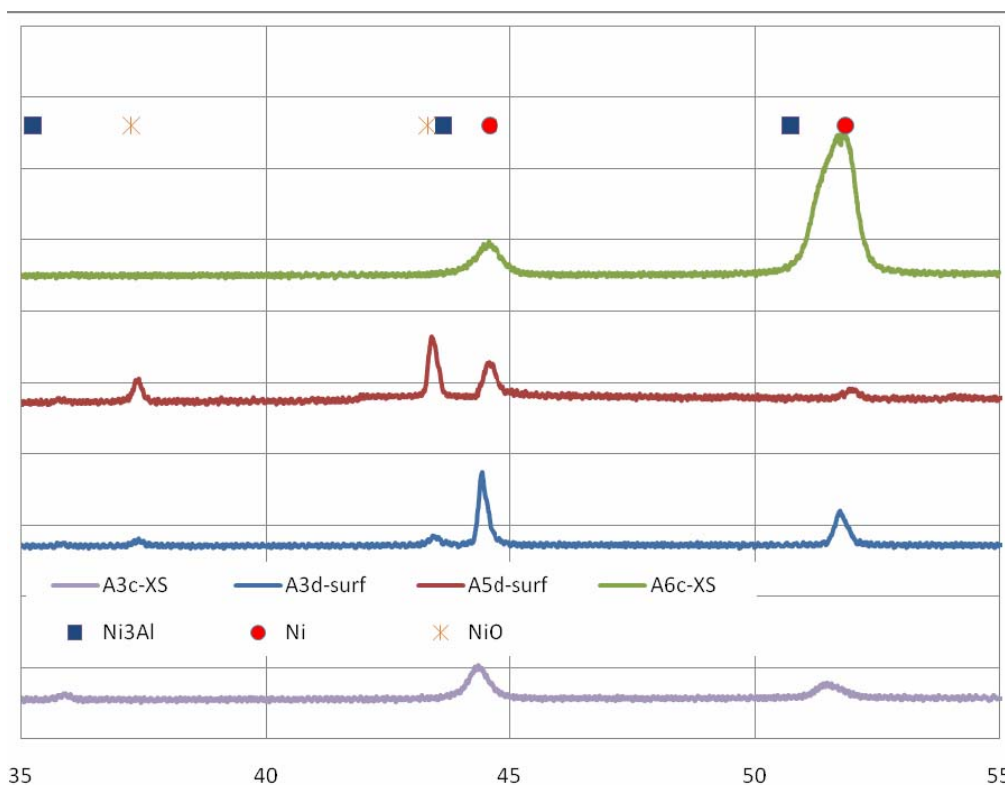


**Figure 14. Examples of XRD Spectra of Samples After In-Situ Resistivity Measurements**

#### 2.2.4. Room Temperature Resistivity Measurements Of Water Quenched And Aged Alloys

Low-frequency ACPD measurements were conducted on the A1, A2, A3, A4, A5, and A6, as well as commercial alloys IN-718, Rene88, and LSHR material specimens, as summarized in Table 4-Table 10. All samples were solutionized in Ar, water quenched, and then aged in Ar atmosphere at various temperatures (600°C, 700°C, and 800°C) for different times. Electrical resistivity measurements were conducted on samples aged at 700°C.

**Table 4: A1 Specimen Dimensions And Heat Treatment Parameters**

Specimen	A1i	A1f	A1g	A1h	A1k	A1l	A1m	A1j
Heat Treatment [hr]	0	0.5	1	2	4	10	20	“infinite”
Length, $l$ [mm]	10.12	9.84	11.01	10.00	9.88	10.65	10.50	11.43
Width, $b$ [mm]	9.69	9.58	9.49	9.75	9.49	10.30	10.39	10.56
Thickness, $t$ [mm]	2.53	2.55	2.63	2.57	2.34	3.18	3.05	2.38
Aspect ratio, $c$	1.04	1.03	1.16	1.03	1.04	1.03	1.01	1.08

**Table 5: A2 Specimen Dimension And Heat Treatment Parameters**

Specimen	A2i	A2f	A2g	A2h	A2k	A2l	A2m	A2j
Heat Treatment [hr]	0	0.5	1	2	4	10	20	“infinite”
Length, $l$ [mm]	10.41	9.69	10.01	9.91	9.86	10.08	9.98	10.05
Width, $b$ [mm]	10.21	9.68	9.58	9.83	9.80	10.00	9.63	9.69
Thickness, $t$ [mm]	2.59	2.60	2.48	2.56	3.75	3.73	3.73	2.56
Aspect ratio, $c$	1.02	1.00	1.04	1.01	1.01	1.01	1.04	1.04

**Table 6: A3 Specimen Dimensions And Heat Treatment Parameters**

Specimen	A3i	A3f	A3g	A3h	A3k	A3l	A3m	A3j
Heat Treatment [hr]	0	0.5	1	2	4	10	20	“infinite”
Length, $l$ [mm]	10.98	10.36	10.42	11.66	10.40	10.44	10.29	10.95
Width, $b$ [mm]	10.80	9.71	9.99	10.25	9.96	10.41	9.97	10.47
Thickness, $t$ [mm]	2.88	2.85	3.49	3.05	2.44	2.61	2.62	3.40
Aspect ratio, $c$	1.02	1.07	1.04	1.14	1.04	1.00	1.03	1.05

**Table 7: A4 Specimen Dimensions And Heat Treatment Parameters**

Specimen	A4i	A4f	A4g	A4h	A4k	A4l	A4m	A4j
Heat Treatment [hr]	0	0.5	1	2	4	10	20	“infinite”
Length, $l$ [mm]	9.91	10.95	10.25	10.04	10.35	10.40	10.43	9.90
Width, $b$ [mm]	9.43	10.16	10.25	9.53	9.79	9.93	10.22	9.50
Thickness, $t$ [mm]	2.92	3.19	2.97	2.81	3.22	2.38	3.24	2.81
Aspect ratio, $c$	1.05	1.08	1.00	1.05	1.06	1.05	1.02	1.04

**Table 8: A5 Specimen Dimensions And Heat Treatment Parameters**

Specimen	A5i	A5f	A5g	A5h	A5k	A5l	A5m	A5j
Heat Treatment [hr]	0	0.5	1	2	4	10	20	“infinite”
Length, $l$ [mm]	9.91	10.95	10.25	10.04	10.10	10.16	9.95	9.90
Width, $b$ [mm]	9.43	10.16	10.25	9.53	9.34	10.06	9.43	9.50
Thickness, $t$ [mm]	2.92	3.19	2.97	2.81	2.46	2.62	3.67	2.81
Aspect ratio, $c$	1.05	1.08	1.00	1.05	1.08	1.01	1.06	1.04

**Table 9: A6 Specimen Dimensions And Heat Treatment Parameters**

Specimen	A6i	A6f	A6g	A6h	A6j
Heat Treatment [hr]	0	0.5	1	2	“infinite”
Length, $l$ [mm]	9.91	10.95	10.25	10.04	9.90
Width, $b$ [mm]	9.43	10.16	10.25	9.53	9.50
Thickness, $t$ [mm]	2.92	3.19	2.97	2.81	2.81
Aspect ratio, $c$	1.05	1.08	1.00	1.05	1.04

**Table 10: Rene88 Specimen Dimensions And Heat Treatment Parameters**

Specimen	R1	R2	R3	R4	Ri
Heat Treatment [hr]	0	0.5	1	2	“infinite”
Length, $l$ [mm]	9.96	10.67	10.82	10.35	10.82
Width, $b$ [mm]	9.92	9.89	10.37	9.09	10.41
Thickness, $t$ [mm]	3.18	2.59	2.38	2.94	2.63
Aspect ratio, $c$	1.00	1.08	1.04	1.14	1.04

It is important to note that the dimensions of the samples provided were all within the acceptable limits of the VDPM for a rectangular plate. It was found computationally that below a thickness to length ratio of 0.4, the error in the VDPM resistivity measurements is negligible. Beyond this point, the accuracy of VDPM drops dramatically. This finding was confirmed experimentally using the specimens in the present project. Also, A5, A6 and most of A4 specimens were found to be ferromagnetic and their ferrite content can be found in Table 11 Table 13. A1, A2, A3 and Rene88 specimens had low magnetic permeability (paramagnetic). The plot of the magnetic permeability plot for samples A1, A2, A3 and Rene88 is shown in Figure 15.

**Table 11: Equivalent Ferrite content in A4 specimens**

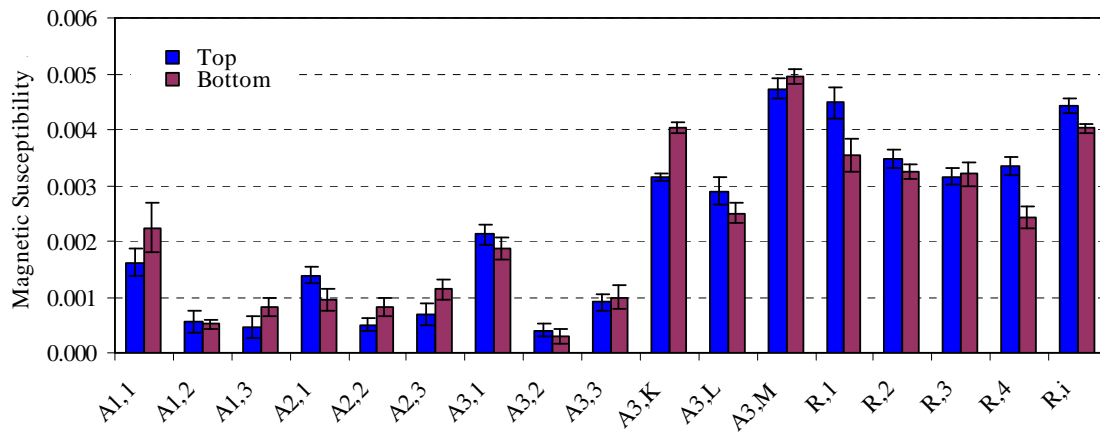
Specimen ID	A4f	A4h	A4k	A4l	A4m	A4j
Heat treatment [hr]	0.5	2	4	10	20	“infinite”
Equivalent Fe content [%]	77.06	87.65	68.44	79.91	85.09	77.37

**Table 12: Equivalent Ferrite content in A5 specimens**

Specimen ID	A5i	A5f	A5g	A5h	A5k	A5l	A5m	A5j
Heat treatment [hr]	0	0.5	1	2	4	10	20	“infinite”
Equivalent Fe content [%]	53.13	44.58	73.28	76.55	81.18	79.91	83.87	32.83

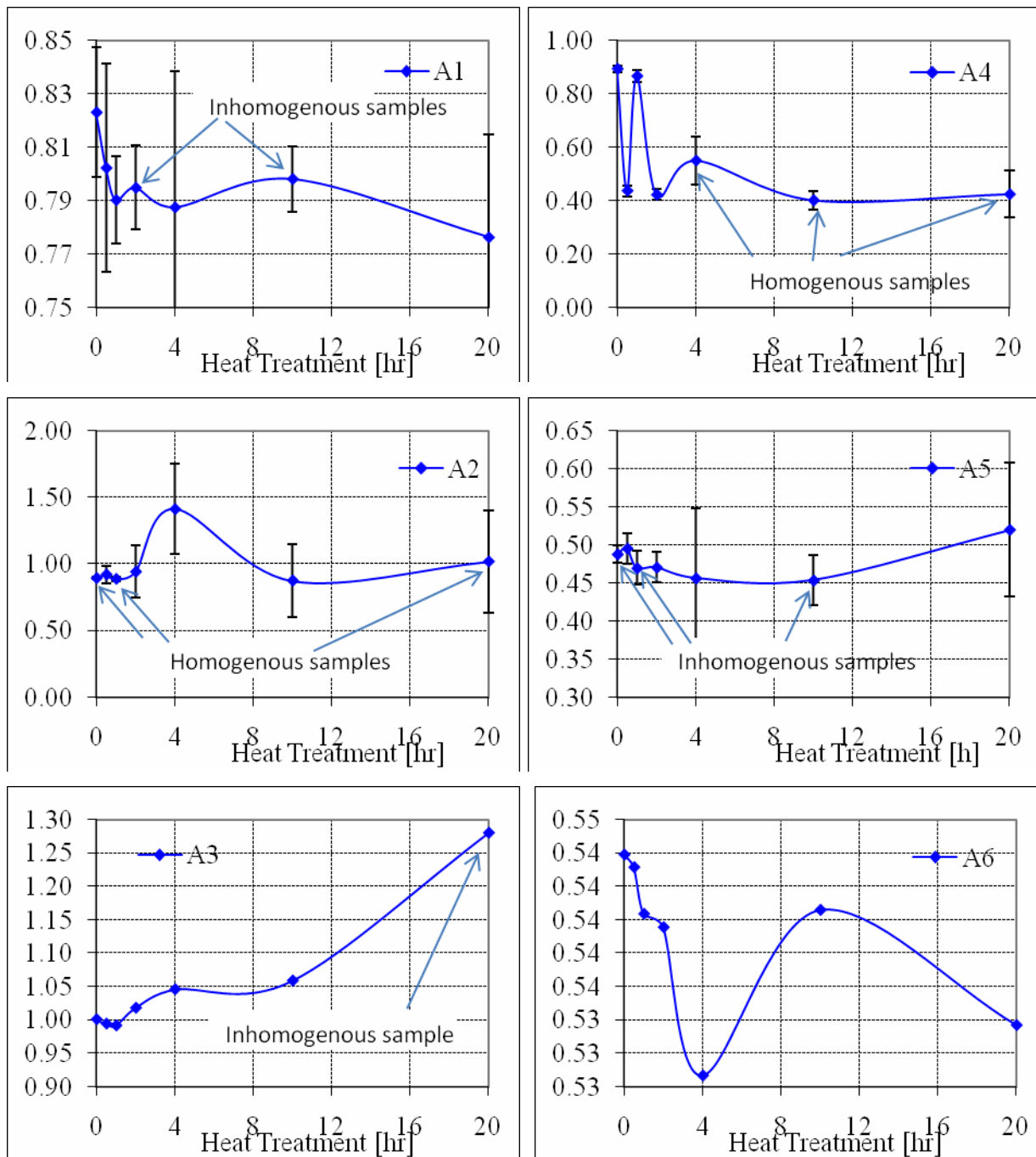
**Table 13: Equivalent Ferrite content in A6 specimens**

Specimen ID	A6i	A6f	A6g	A6h	A6j
Heat treatment [hr]	0	0.5	1	2	“infinite”
Equivalent Fe content [%]	44.92	23.76	31.74	31.66	17.94

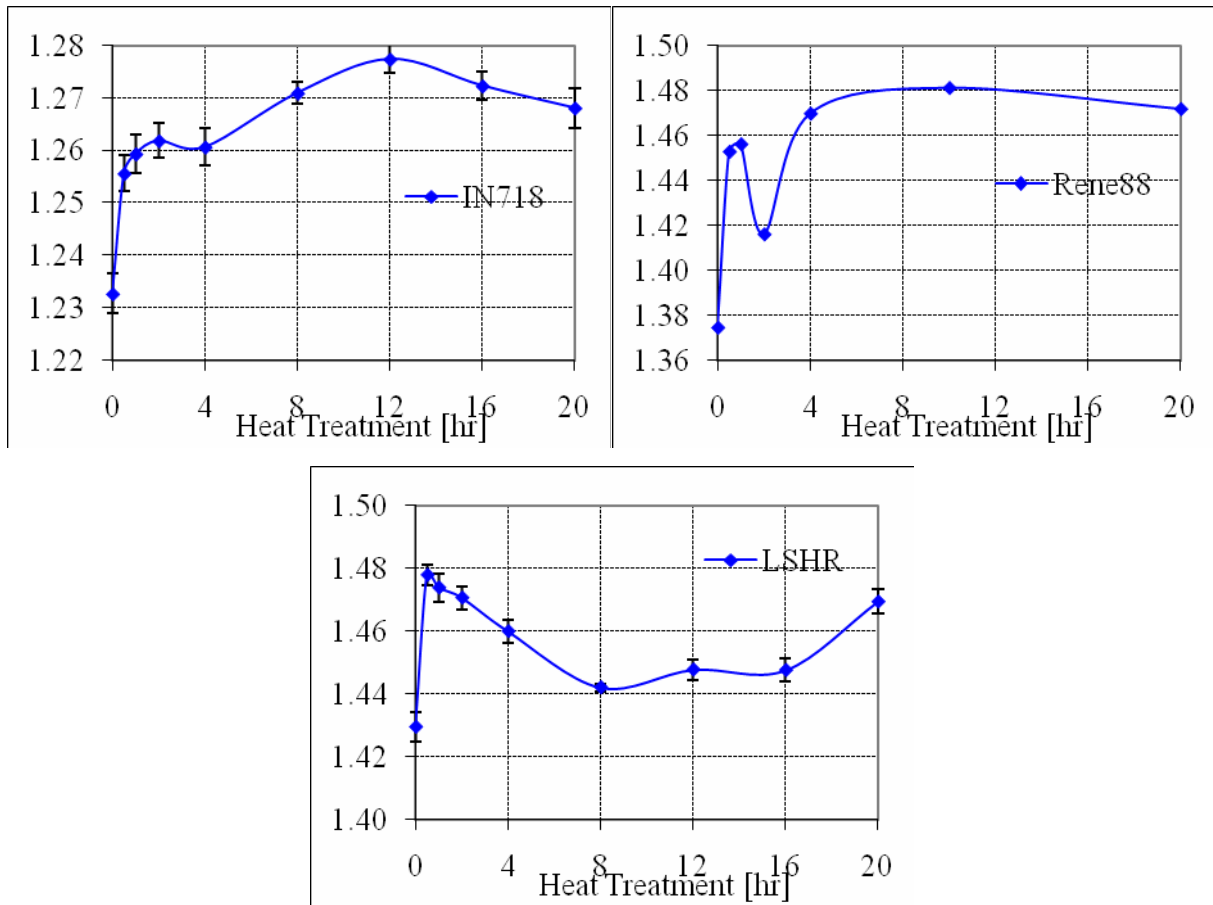


**Figure 15: Magnetic Susceptibility of A1, A2, A3 And Rene88 Specimens**





**Figure 16: Room Temperature Resistivity ( $\mu\Omega m$ ) Of Samples A1-A3 and A4-A6 Water Quenched From 1220°C and Aged At 700°C For Different Times. The Samples That Exhibited Most Inhomogeneity Are Indicated**



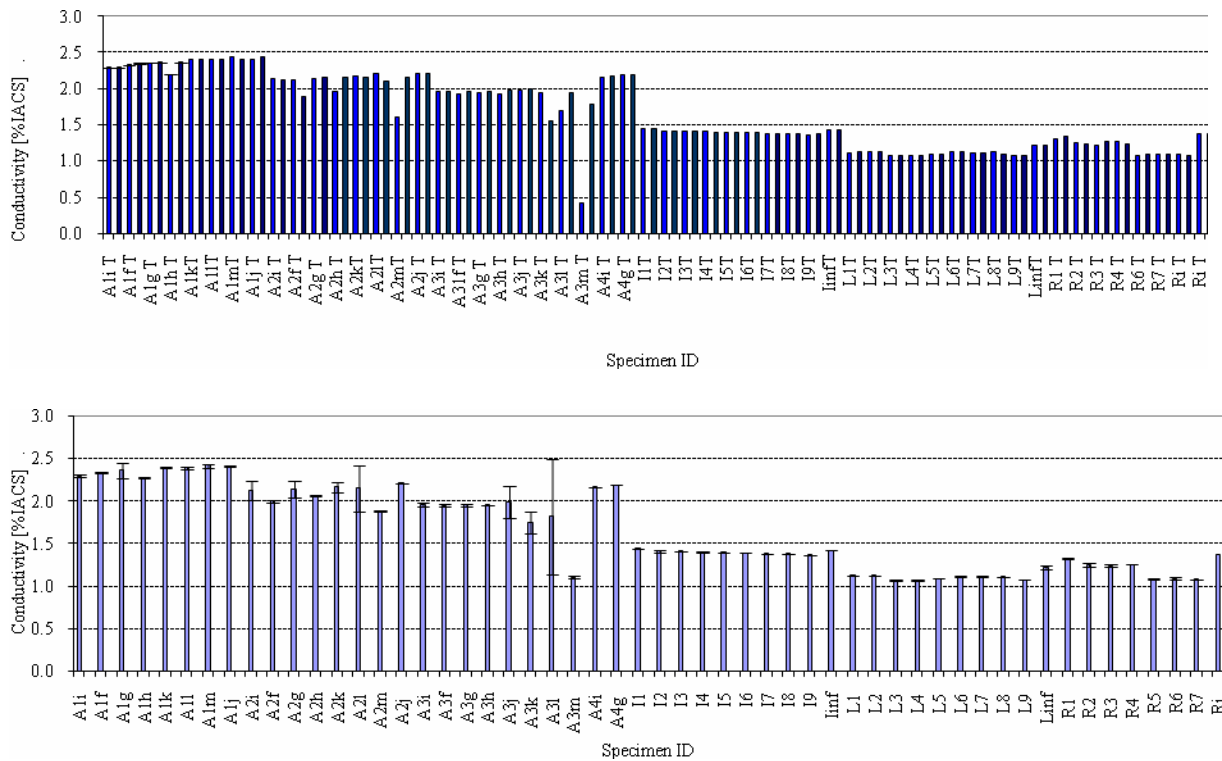
**Figure 17: Room Temperature Resistivity ( $\mu\Omega\text{m}$ ) of Commercial IN-718, Rene88, and LSHR Aged At 700°C For Different Times**

Figure 16 shows the room temperature resistivity for samples A1-A3 and A4-A6 solutionized and water quenched, and then aged at 700°C for various times. Figure 17 shows Room temperature resistivity of commercial IN-718, Rene88, and LSHR, solutionized, water quenched, and aged at 700°C for different times. The measurements were based on the low-frequency Alternating Current Potential Drop (ACPD) technique.

Overall the specimens showed different and complex resistivity variation with heat treatment (Figure 16 and Figure 17). Clearly, most alloys exhibit strongly non-monotonic dependence on resistivity on the thermal exposure (ageing time), which would preclude the use of them as thermal sensors. In order to better understand the origins of this complex behavior, tests were conducted to evaluate the possibility that measurements are affected by factors other than

intrinsic material properties that are known to influence the electrical resistivity (phase composition, stress levels, etc.). The most suspected factors were materials inhomogeneity (pores, cracks, chemical inhomogeneity). Such factors were much more likely to affect the arc melted experimental alloys (A1-A6) than the commercial alloys.

To evaluate the possibility that our resistivity measurements were indeed affected by material inhomogeneity, additional studies were conducted using eddy current electrical conductivity measurements at a frequency of 2 MHz. In particular, among the A3 samples, the specimen that was heat treated for 20 hours was found to be extremely inhomogeneous. As shown in Figure 19, A3m (20h heat treatment) shows a conductivity difference in excess of 75% between the top and bottom surfaces. A3k (4h) and A3l (10h) specimens also show relatively high conductivity difference between the top and bottom surfaces, but A3m shows by far the largest inhomogeneity. In contrast, commercial alloy Rene 88 has very low level of inhomogeneity, as demonstrated by the very small differences between the top and bottom surfaces for all tested specimens (Figure 19).



**Figure 18: Absolute Resistivity Measurements on Samples A1-A4, IN718 Rene88, and LSHR For The Top (Medium Blue) And Bottom (Dark Blue) Values Separately (Top Chart), and The Average Value With Uncertainty Bars (Bottom Chart)**

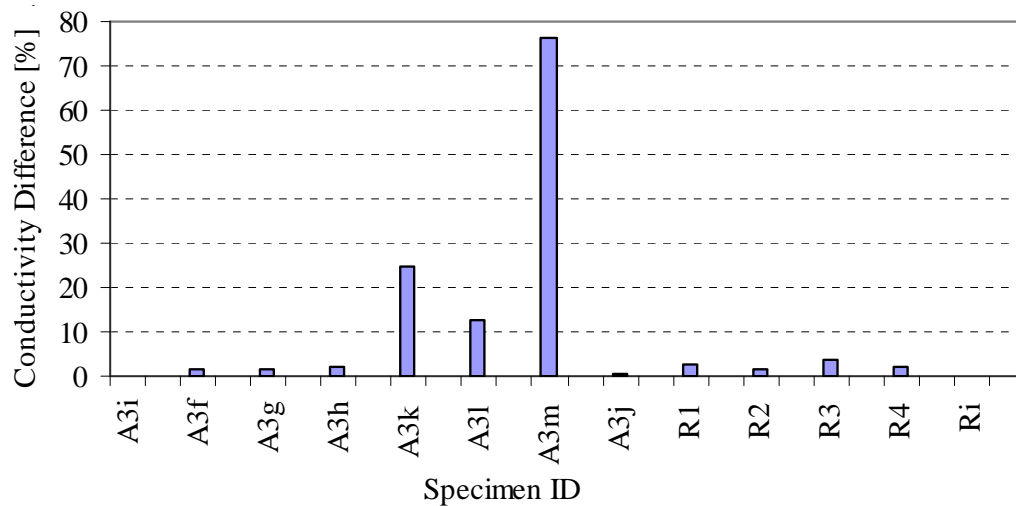


**Figure 19: Conductivity Difference between Top and Bottom Surfaces of A3 and Rene88 Materials**

To confirm this finding, eddy current conductivity images of the samples were taken by a ~0.5 mm pencil probe at 2 MHz using a Nortec 2000S Eddyscope. The specimens were scanned on an x-y table driven by a VELMEX 86 mm motor controller. The results are presented in Figure 20, which shows the high variation in conductivity within each surface of the A3m as well as between the top and bottom surfaces. A less significant variation is observed in A3k sample, while practically no variation is noted in Rene88 (R4) sample, which asserts its homogeneity. Since ACPD resistivity measurements give only a volumetric average of the material resistivity, it is only accurate when the samples are homogeneous, which gives very little confidence to the A3m data point.

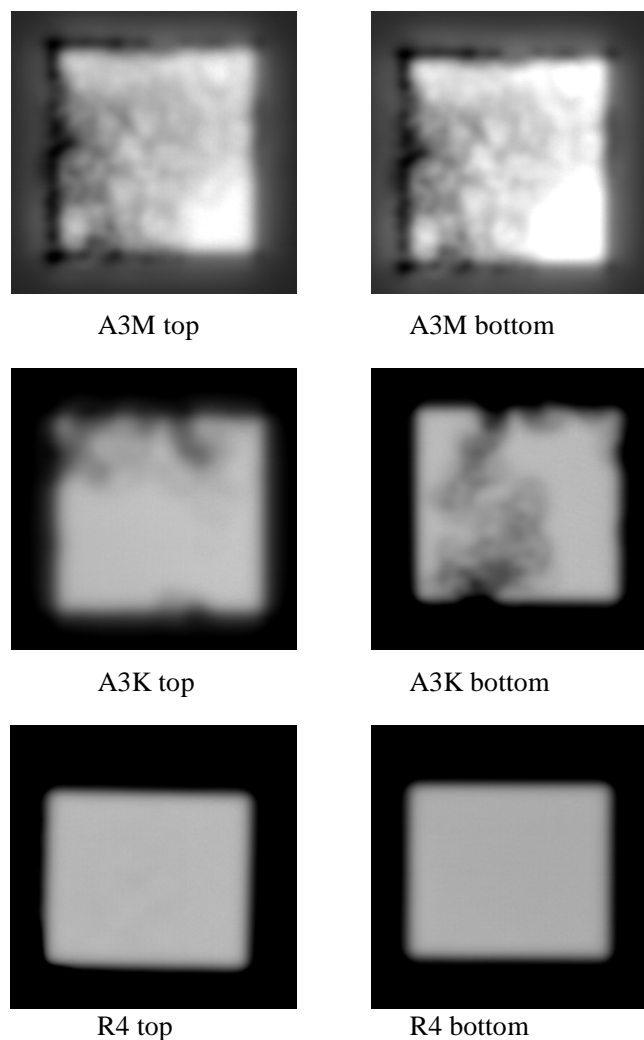


**Figure 20: Eddy Current Conductivity Images For A3m, A3k and Rene88 R4 Specimens**

As noted above, the homogeneity of the material to be tested using the VDPM is detrimental to the accuracy of the resistivity measurement. This technique is only reliable on specimens that are homogeneous and isotropic enough to satisfy a well-defined criterion. An effective test for the homogeneity of the specimen is to compare the ratio of the vertical to horizontal resistances to the aspect (length-to-width) ratio,  $c$ . It was verified numerically that this relationship is in the form of

$$r \approx c^n, \quad (1)$$

where  $r$  is the ratio of the horizontal resistance to the vertical resistance,  $c$  is the geometrical aspect ratio of the specimen, and the power coefficient  $n \approx 6.3$ . All homogeneous samples in this study scatter closely around this regression line as shown in Figure 21. As a first indication of the accuracy of the results, the further the  $r$  value is from this curve line, the more inhomogeneous the sample is and thus the more inaccuracy is introduced into the resistivity measurement. Specimens showing a resistance ratio with more than 10% difference from its expected value should be considered outliers.

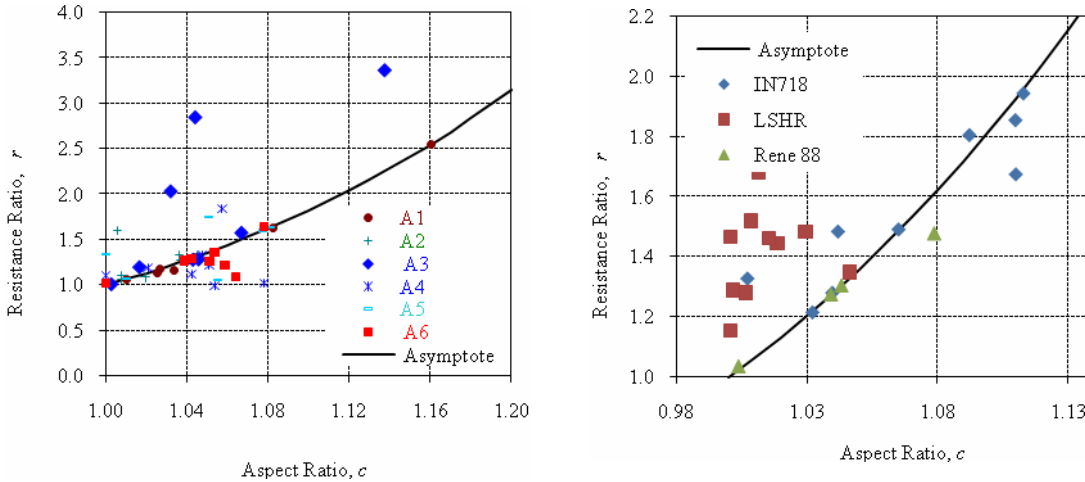


**Figure 21: Resistance Ratio Variation with Aspect Ratio For Samples A1-A6 And Commercial Alloys IN718, Rene88, And LSHR (For Samples Shown In Figure 16 And Figure 17)**

To further evaluate the reproducibility of the resistivity measurements, and the effect of material inhomogeneity, additional samples of A3 (aged for 1, 4, and 20 hours), A5 (aged 0.5, 4, and 10 hours), and Rene88 (aged for 2 and 50 hours) were prepared. Each alloy/heat treatment category

was represented by 5 identically prepared specimens. The results of this investigation are shown in Figure 22. As can be seen, all A3 samples are well outside the 10% threshold. In contrast, all A5 and Rene 88 samples show acceptable values of the resistance ratio. The large scatter exhibited by the A3 series of specimens cannot be attributed to geometrical deviations and are certainly caused by material anomalies. The measurement technique employed in this study not only corrects for inevitable variations in the geometrical aspect ratio of the specimens, but also provides a clear indication when this correction is not expected to work because of material anomalies. This independent indicator, which is based on the resistivity ratio between orthogonal measurements and the geometrical aspect ratio, flagged all of the A3 specimens as anomalous. This indication is perfectly consistent with the large scatter found among the A3 specimens. The present results indicate that specimens of the same arc-melted material heat-treated for the same period of time may present considerable material anomalies and do not likely have the same initial microstructure. Moreover, some of these specimens show large resistivity variations within themselves (Figure 20). Chemical inhomogeneity could potentially result in significant differences in resistivity values. However, the immense resistivity variation (over ~100%) in many A3 samples is unlikely to be caused by chemical inhomogeneity alone. Other reasons like porosity and cracks should also be considered to explain the significantly different levels of conductivity/resistivity between samples of the same material heat-treated at the same temperature. Indeed, evidence of significant porosity was later observed in cross-sectional samples even under a low-magnification microscope during microhardness measurements. Overall most specimens with unusual values of mass density show odd resistivity readings.

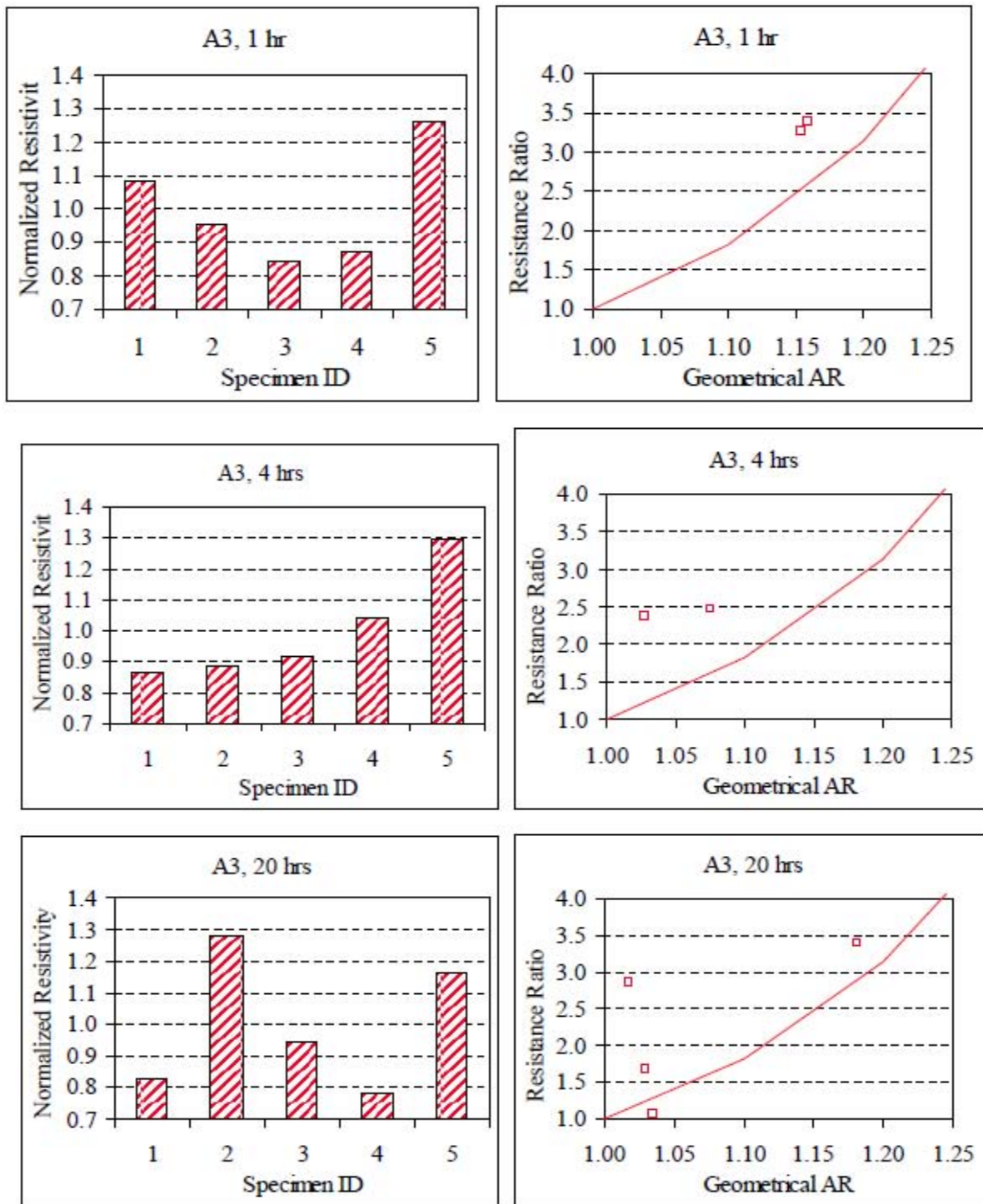


**Figure 22: Normalized Resistivity And The Resistance Ratio Variation With Aspect Ratio For Sets Of 5 Specimens For Alloys A3, A5, And Rene 88 Aged At 700°C For Different Times**



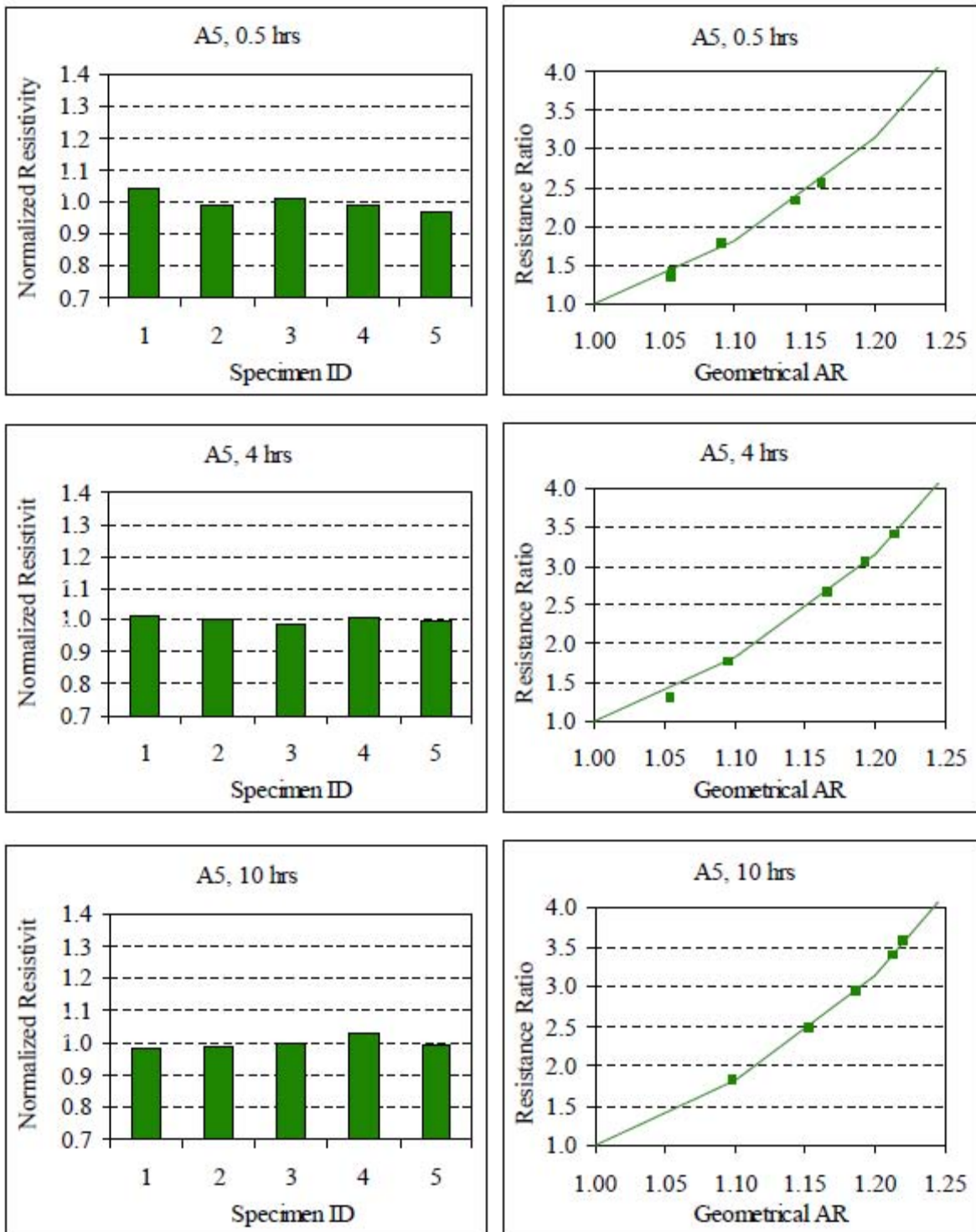


Figure 22 (Continued).

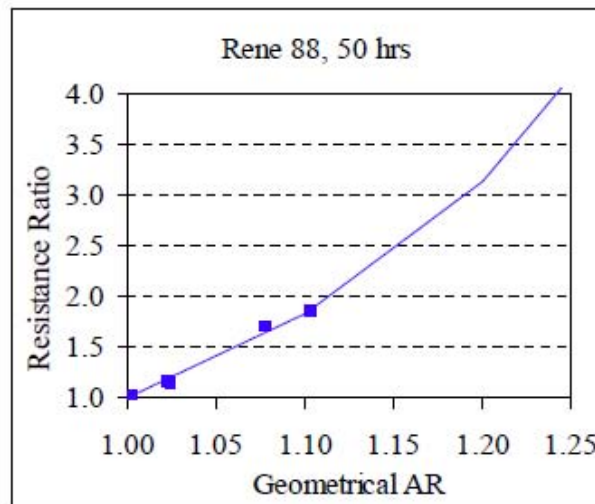
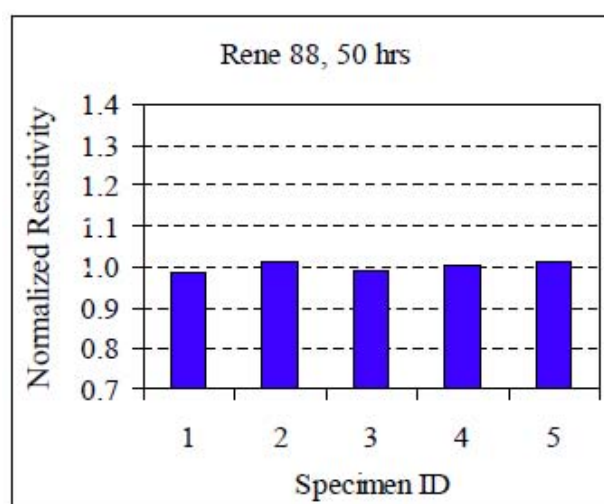
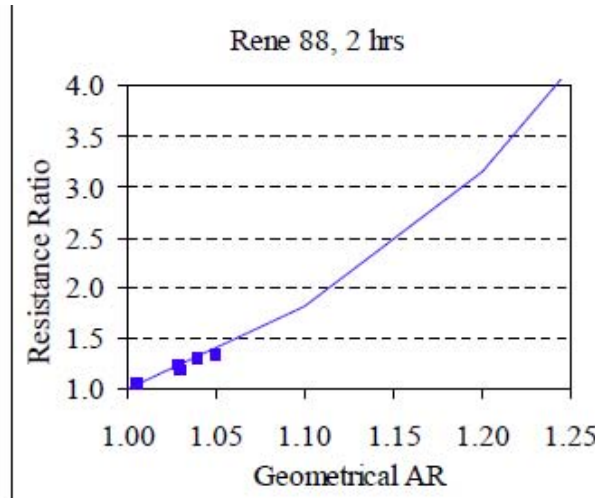
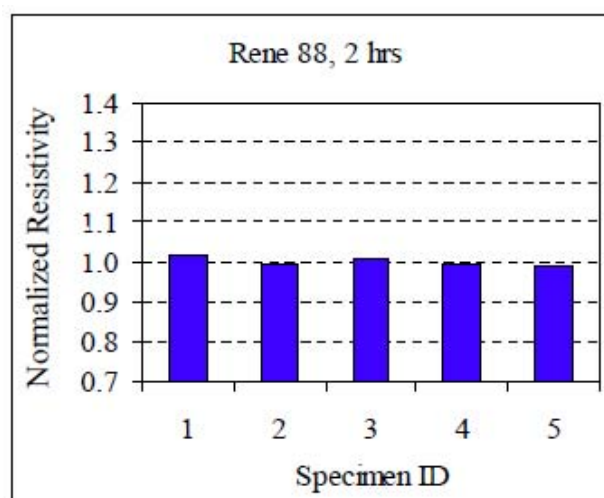
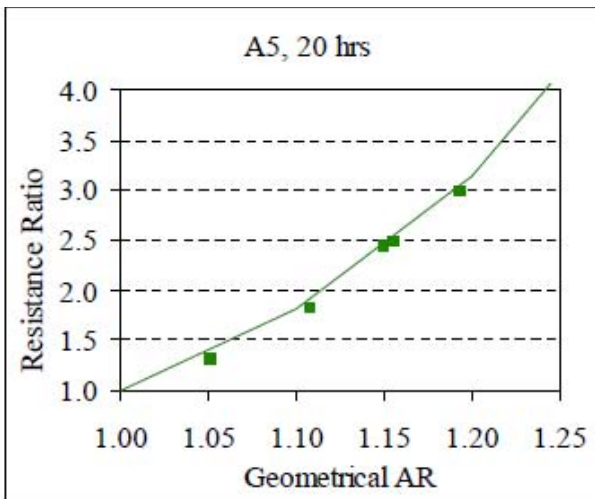
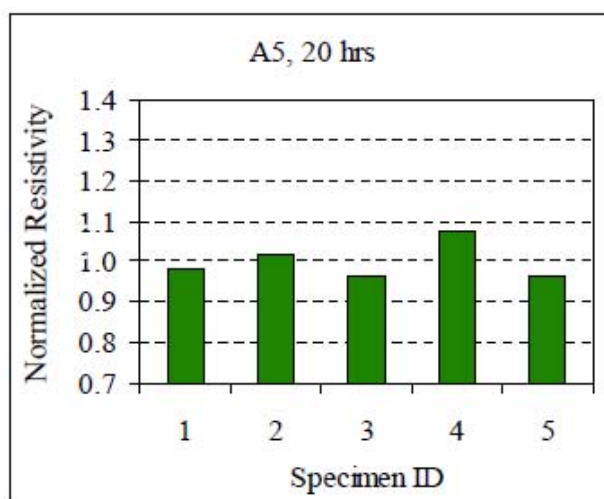


Figure 22 (Continued).

As expected, inhomogeneity in the specimens affected enormously the outcome of the low-frequency resistivity measurements in these materials. Among the initially tested arc melted compositions, (alloys A1-A6, Figure 16), the most affected compositions were A1, A2, A4, A5 materials. Among the initially tested A3 samples (Figure 16) the sample heat treated for 20 hours was the only one that clearly had gross inhomogeneity (based on the eddy current conductivity scanning images), while three out of 7 tested A5 samples exhibited considerable inhomogeneity (Figure 16 and Figure 21). However, additional experiments with A3 and A5 samples contradicted these initial findings. Thus, all 15 additional A3 samples (heat treated in groups of 5 for 3 different times) showed gross deviation from the expected dependency of normalized resistivity on the aspect ratio (Figure 22). On the contrary, the 20 additional A5 (heat treated in groups of 5 for 4 different times) were in a very good agreement with the expected dependency of normalized resistivity on the aspect ratio (Figure 22), indicating no material inhomogeneity. Thus, it is apparent that material inhomogeneity may be present in all these alloys, and its presence varies from batch to batch and depending on the location in the ingot. Therefore, for the purposes of sensor development based on resistivity measurements, these alloys are not suitable until subjected to further processing that would eliminate the material inhomogeneity.

Furthermore, while the dependency of normalized resistivity on the aspect ratio tests of additional Rene 88 specimens aged for 2 h and 50 hours (5 specimens each for each heat treatment), and the eddy current conductivity scanning of the initial Rene 88 samples did not reveal any material inhomogeneity or deviation from the expected dependency of the resistance ratio on the aspect ratio (**Figure 21** and **Figure 19**, respectively), most initially tested specimens of commercial alloys, including Rene 88, IN718, and LSHR did exhibit substantial deviation from the expected dependency of the resistance ratio on the aspect ratio (**Figure 20**).

Thus, it is apparent that material inhomogeneity may be present in all these alloys, and its presence varies from batch to batch, depending possibly on the location in the ingot and subsequent heat treatment. Therefore, for the purposes of sensor development based on resistivity measurements, these alloys may not be suitable until subjected to further processing and/or selection that would eliminate the material inhomogeneity.

### 2.2.5. Microhardness Measurements

In view of the inconsistent results obtained using the electrical resistivity methods, and to understand the sources of the problem, more experiments were conducted to measure the hardness values of all alloys under investigation. It needs to be pointed out, that microhardness measurements have their advantages and disadvantages as compared to the electrical measurements. Obviously, microhardness measurements are more time consuming and cannot be done remotely. Second, they can be considerably affected by the crystallographic anisotropy of plastic deformation [10,11], especially in materials subjected to prolonged heat treatment with the resulting grain growth. However, in non-homogenous materials containing pores, cracks, or inclusion phases, indentations can be placed in areas not affected by the inhomogeneity, thus providing more reliable data on the intrinsic material properties.

A typical dependence of the microhardness of a solutionized Ni-based super-alloy (IN-718, after [10]) is shown in **Figure 23**. The processes taking place during aging of a Ni-based super-alloys are very complex, and include relaxation of the residual thermal stresses, annealing of quenched-in vacancies, precipitation of the second phase (first order phase transformation), diffusion-controlled compositional changes in both matrix and precipitates, and growth and, eventually, coarsening of the precipitates. All of these changes affect the microhardness (as well as other physical properties) in a complex manner. In general, the microhardness increases with the continuous precipitation of the strengthening phase ( $\gamma'$  in Ni-Al-Ti and Ni-Al-Cr alloys considered here). The microhardness reaches maximum as the amount of the precipitates approaches its equilibrium value and then typically begin to decrease as coarsening of the precipitates sets in (over-aging).

For the purpose of sensor development, it is essential that the target property (in this case, microhardness) changes monotonically with thermal exposure within the sensor useful life. Thus, provided that the kinetics of the  $\gamma'$  precipitation is sluggish enough at the temperatures of interest to provide sufficient sensor life span, the initial increase of hardness of a quenched alloy with aging can be used to monitor the extent of thermal exposure. Alternatively, an alloy pre-aged to maximum hardness can be used to monitor thermal exposure through the attendant decrease of

microhardness (over-aging) The later is likely to better work for higher temperature exposure due to its relatively more sluggish kinetics, while the former may be better suited for lower temperatures, where the kinetics of the  $g'$  precipitation may be slow enough to provide a reasonable life time of the sensor.

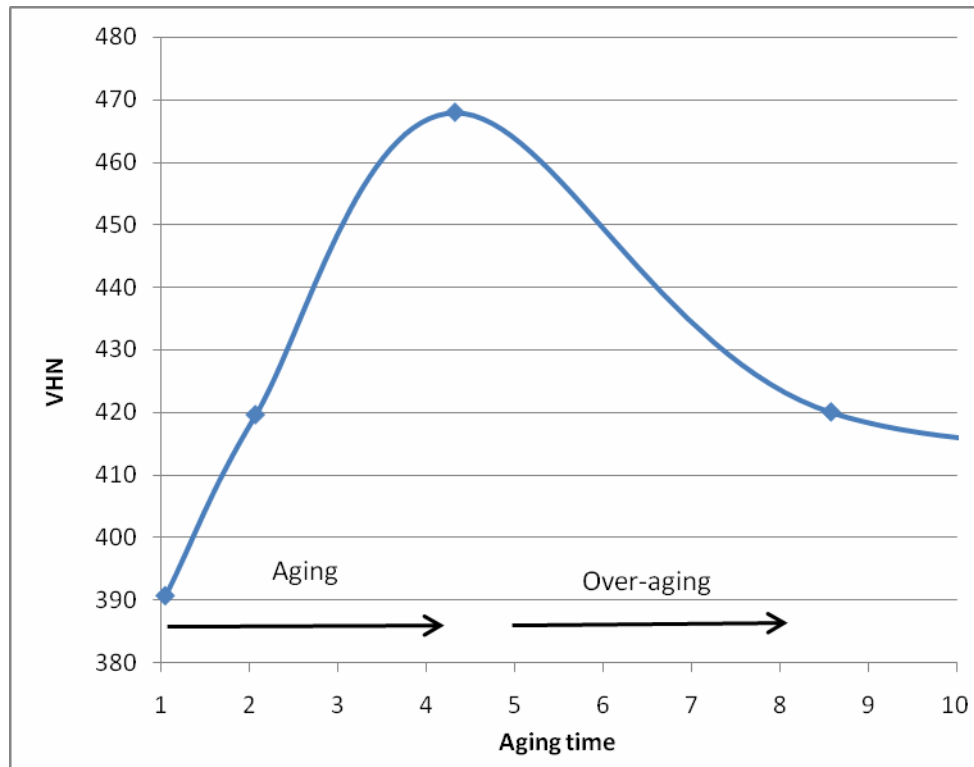


**Figure 23: Typical Dependence of Microhardness of Ni-Based Superalloy on Aging Time**

At first, microhardness measurements were conducted on samples of aged alloys that were previously investigated using room temperature resistivity measurements (**Figure 15** and **Figure 16**). Typical results of these measurements for alloys A3 and A5 are shown in **Figure 24**. Throughout this study each microhardness data-point corresponds to an average of at least 10 measurements, with the error bars representing the standard deviation. The measurements were taken separately in the center, as well as close to the edge of each specimen.

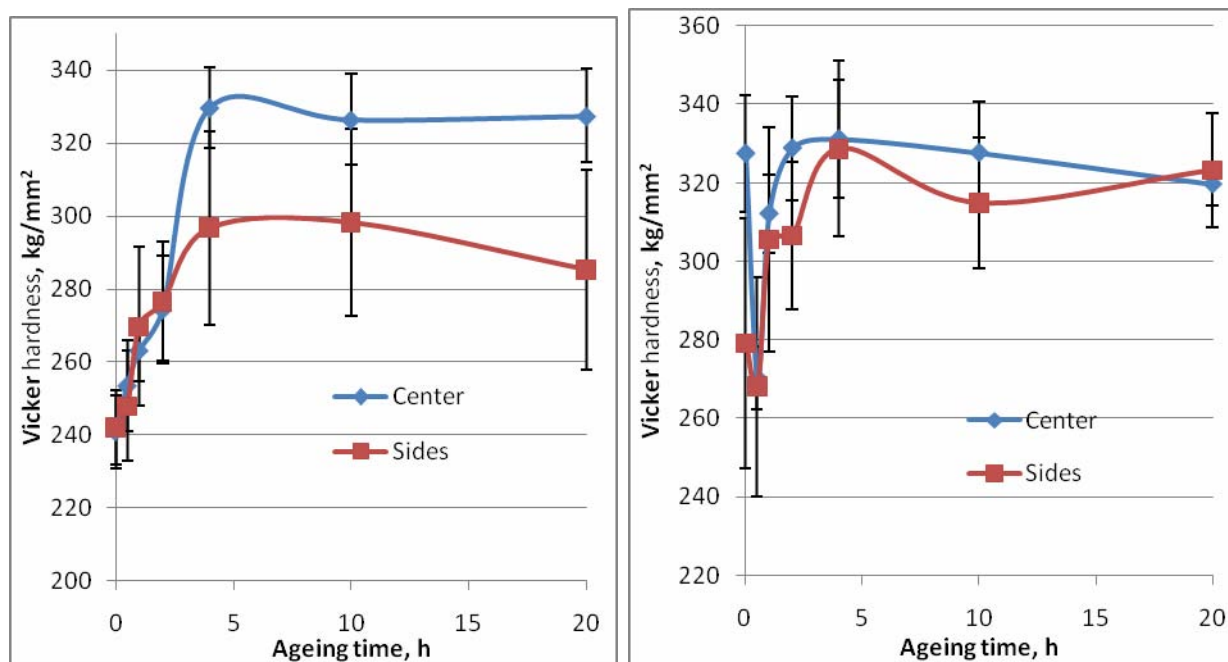


**Figure 24: Vickers Microhardness Values for Alloys A3 and A5 Aged At 700°C For Different Times**

These results indicated that the specimens clearly had inconsistent values of microhardness across their surface, which correlates with the erratic results of the resistivity measurements. Noteworthy was also large scatter of the measurements for each heat treatment (see error bars in **Figure 24**). This could most likely be a result of different cooling rate at the surface and the interior of the sample during quenching, as well as chemical variation of the surface (i.e., loss of alloying elements during high temperature annealing). The problem was apparently further exacerbated by the fact that all specimens were ground on one side after the heat treatment and prior to the resistivity measurements to ensure compliance with the geometrical requirements of the resistivity measurements. The amount of the material removed varied from specimen to specimen (depending on the original dimension). Therefore, in some samples the surface layer had been removed prior to microhardness measurements. In these specimens, measurements taken in the center could represent the interior values, while those at close to the edges might represent the surface values. In other samples, where the amount of material removed during grinding was negligible, both the center and the edges represented the surface. In such samples,

the values of microhardness were very close at the center and at the edges were very close (i.e., A3 aged for 4 and 20 hours, and A5 aged for 1 and 2 hours, **Figure 24**).

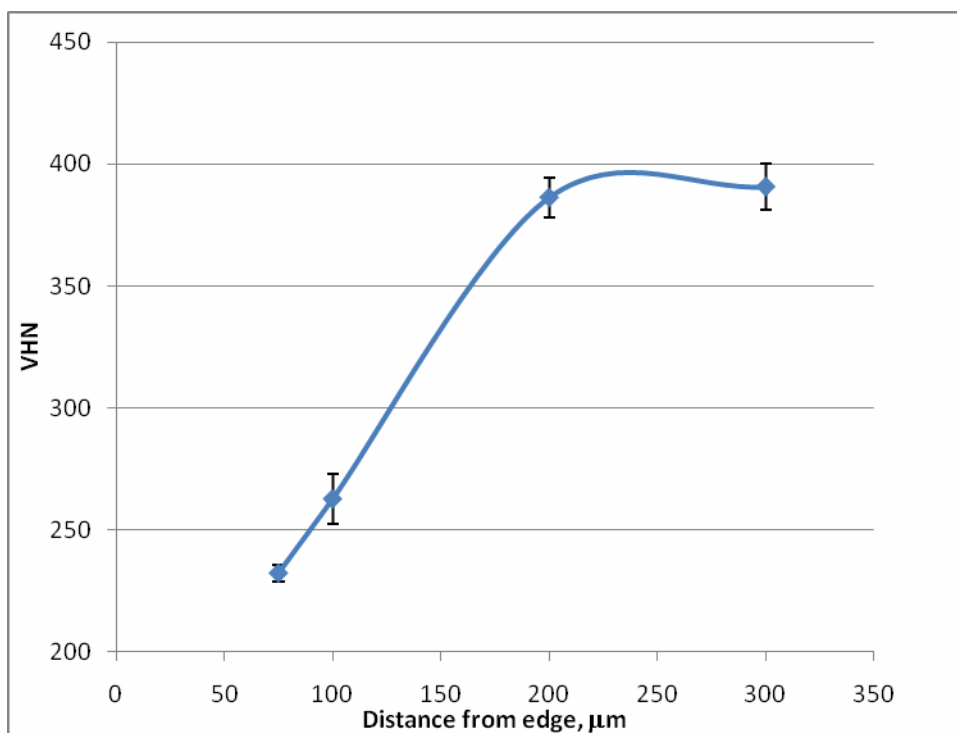


**Figure 25: Vickers Microhardness Values for Rene 88 Alloy Aged at 700°C for 4 Hours Measured at Different Locations from the Edge**

To obtain more reliable and consistent measurements, all samples were sectioned and polished such that representative microhardness data could be collected from the interior of the samples. Measurements taken at different locations with respect to the specimen edge indicated large variation of microhardness within the first 150-300  $\mu\text{m}$  from the surface. An example of this for the Rene 88 alloy aged at 700°C for 4 hours is shown in **Figure 25**. The low microhardness value in the surface region is a likely indication of the loss of the alloying elements during high temperature heat treatment. Such changes in surface chemistry and microstructure are likely to also affect the resistivity measurements, probably accounting for the inconsistent results (**Figure 16 - Figure 22**).

It became clear from these results that reliable and consistent measurements of microhardness could only be obtained from the center regions of sectioned samples, where the alloy composition is not affected by loss of alloying elements and microstructure is not affected by varying cooling rates during quenching. The results of these experiments for alloys A1-A3 and alloys A4-A6 are shown in **Figure 26** and **Figure 27**, respectively.

These results indicate that while the dependence of the microhardness values on aging time for these alloys can be quite complex, it is fairly consistent (especially for alloys A4-A6) and can be rationalized in terms of the main factors affecting the microhardness of these alloys, namely that amount and size distribution of the strengthening  $\gamma'$  phase, and the level of micro-stresses (particularly thermal stresses) that are present in the material. Note also much smaller data scatter, as compared to **Figure 24**.

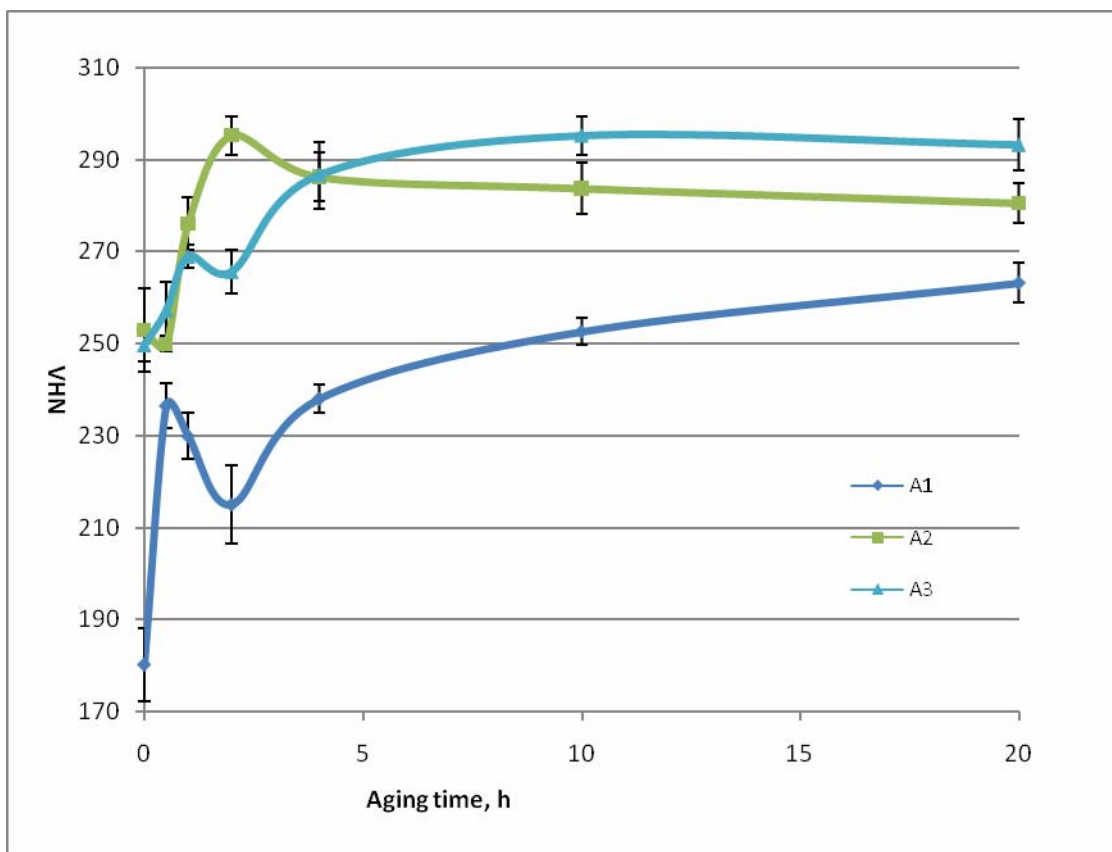


**Figure 26: Vickers Microhardness Values for Alloys A1, A2, and A3 Aged at 700°C for Various Times**



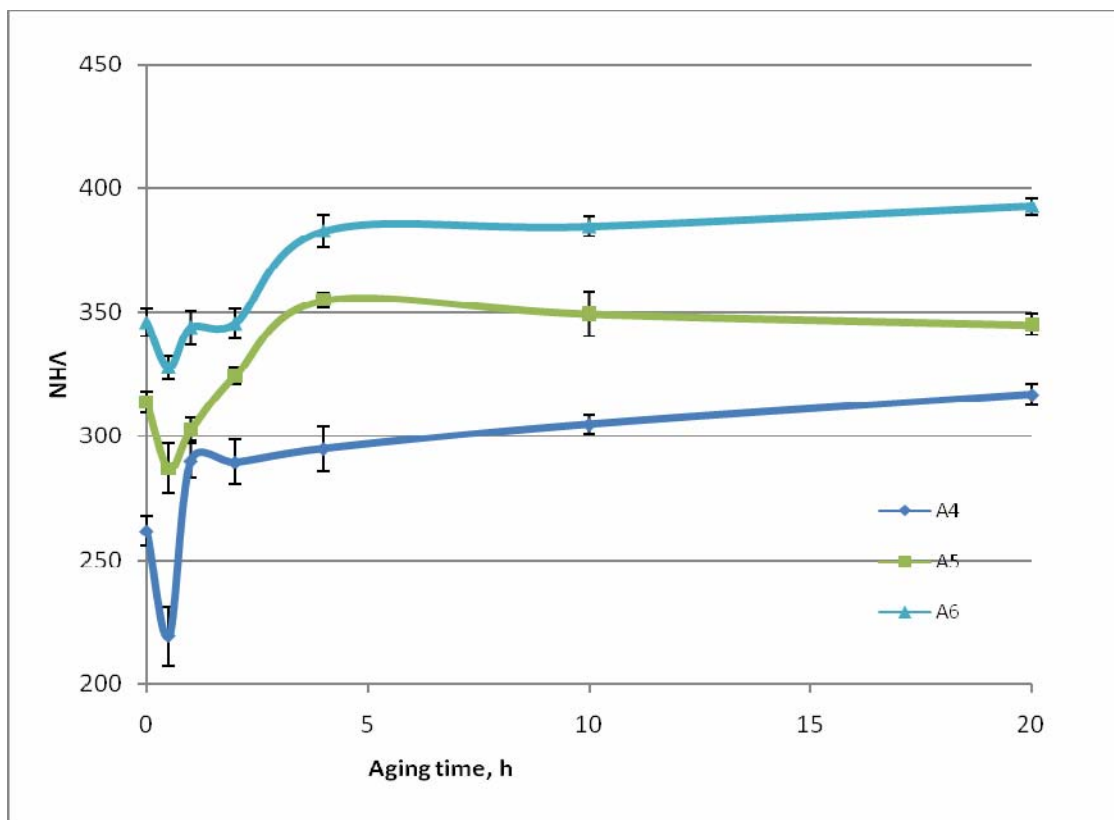


**Figure 27: Vickers Microhardness Values for Alloys A4, A5, and A6 Aged At 700°C for Various Times**

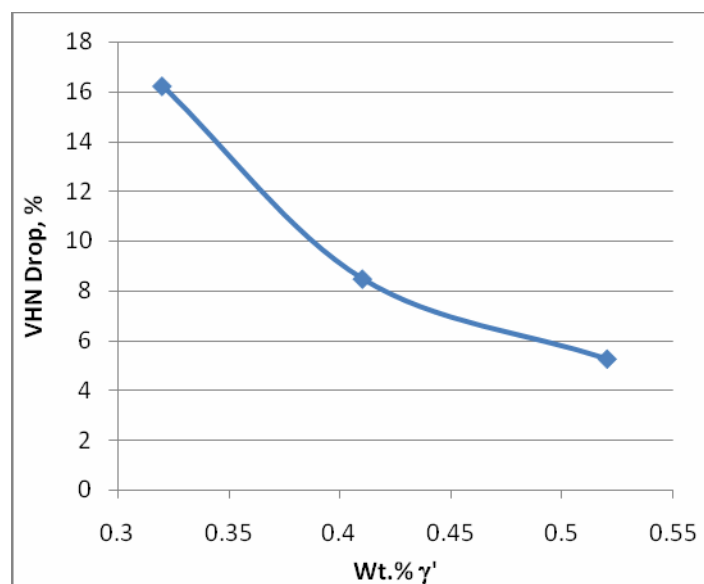


**Figure 28: Initial Drop Of Vickers Microhardness Values for Water Quenched Alloys A4, A5, and A6 Aged At 700°C for 30 Minutes as A Function of Composition**

Thus, the alloys A4-A6 all exhibit very similar dependence of microhardness on aging time, although, as could be expected, the overall hardness progressively increases with the increase of the Al content. After aging for 30 minutes at 700°C, the microhardness of all three alloys drops to its lowest level for each alloy by about 5% to 16% depending on the Al content (**Figure 28**). This lowest hardness value itself is a strong function of the composition. **Figure 29** shows its value plotted against the equilibrium weight fraction of  $\gamma'$  in each alloy, along with the reported literature values of pure Ni and Ni<sub>3</sub>Al [11,12] for comparison. This initial drop in hardness is most likely related to the relaxation of the thermal stresses present in the water quenched sample, which at this initial stage offsets the increase of microhardness associated with precipitation of  $\gamma'$ . This is in-line with the decrease of the initial drop of microhardness with the increase of the Al content, from A4 to A6. Indeed, all alloys were homogenized at and quenched from the same temperature, 1220°C, while their solutionizing temperatures ranged from 900°C to 1200°C (**Table 1**). This initial softening is generally followed by an increase in microhardness, relatively rapid within the next 2 – 4 hours of aging and then more gradual during subsequent aging. Alloy A5, however, shows a gradual decrease of microhardness after the first 4 hours of aging.

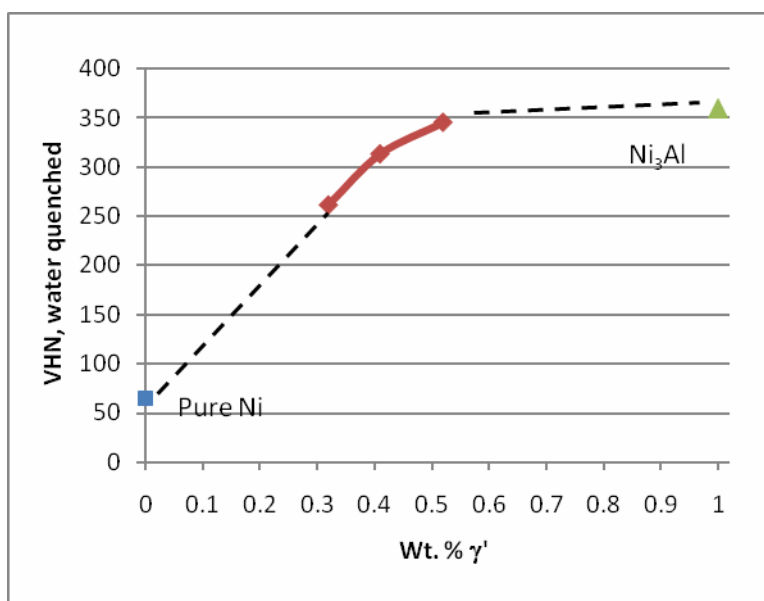


**Figure 29: Vickers Microhardness Values for Water Quenched Alloys A4, A5, and A6 Aged At 700°C For 30 Minutes As A Function Of Equilibrium Weight Fraction of  $\gamma'$**

Among the alloys A1-A3, the pattern is somewhat less consistent, although alloys A1 and A3 clearly have consistent dependence of microhardness on aging time (**Figure 26**). For these alloys, the microhardness increases during the first hour of aging, then drops between 1 and 2 hours before it begins to increase again with subsequent aging. Apparently, unlike A4-A6 alloys, for these compositions the onset of stress relaxation is delayed, so the microhardness first increases due to the precipitation of  $\gamma'$ , then drops due to stress relaxation, and then continues to increase as  $\gamma'$  continues to precipitate. Curiously, in both groups of alloys, the compositions with the medium Al content (A2 and A5) exhibit a decrease of microhardness after the first 2-4 hours of aging.

Based on the experience with, and the results on the arc-melted alloys described above, additional microhardness experiments with commercial alloys IN-718 and Rene88 were conducted. It could be expected that this alloys, having been heat treated to or near their peak mechanical properties (microhardness) might be good candidates for sensor development based on the gradual decline in the microhardness values due to over-aging. These alloys possess high hardness values when aged properly for peak strength, and their strength drops considerably if over-aging occurs [10]. Considerable variation of the target property (microhardness) is an indication of the alloys potential for use as thermal sensor. This would be particularly useful at higher temperatures, where other microstructural changes (e.g., phase precipitation) happen too fast to be used in sensor applications.

Accordingly, samples of engine-grade alloys IN718 (average as-received microhardness  $397 \pm 7$ ) and Rene88DP (average as-received microhardness  $481 \pm 11$ ) alloys were prepared and subjected to additional aging treatments. The Rene88 samples were heat treated at 800°C, 850°C, and 900°C for various time intervals from 1 to 48 hours. The heat treated samples were then sectioned, mounted and polished for the microhardness measurements. The results of these experiments are shown in **Figure 30**.

Large and erratic variations of microhardness observed in these experiments demonstrated were a clear indication of considerable differences in the properties of the as-received material. Thus, it was decided to systematically measure microhardness across a representative cross-section of the bulk piece of Rene 88DP alloy from which all specimens had been cut. The results of the microhardness measurements taken in six different location of an approximately 2 x 2" section of the material are shown in **Figure 31**. These results demonstrate clearly that very large variations in the initial properties exist within the as-received material, and therefore between the individual specimens of the material. The range of these variations exceeds the range of the microhardness values observed for the heat treated specimens in **Figure 30**, and thus clearly accounts for the erratic results.

It became clear, therefore, that due to such large variations in properties, as-received material could not be used for studying the dependence of microhardness of this material on thermal exposure. In order to achieve the initial goal set for this part of the study, i.e., to explore the possibility of using commercial engine-grade (heat treated to or near their peak mechanical properties) Ni-based superalloys as high temperature thermal sensors, the material had to be first homogenized and heat treated in a uniform way, ensuring that all samples to be tested have identical initial microstructure and properties.

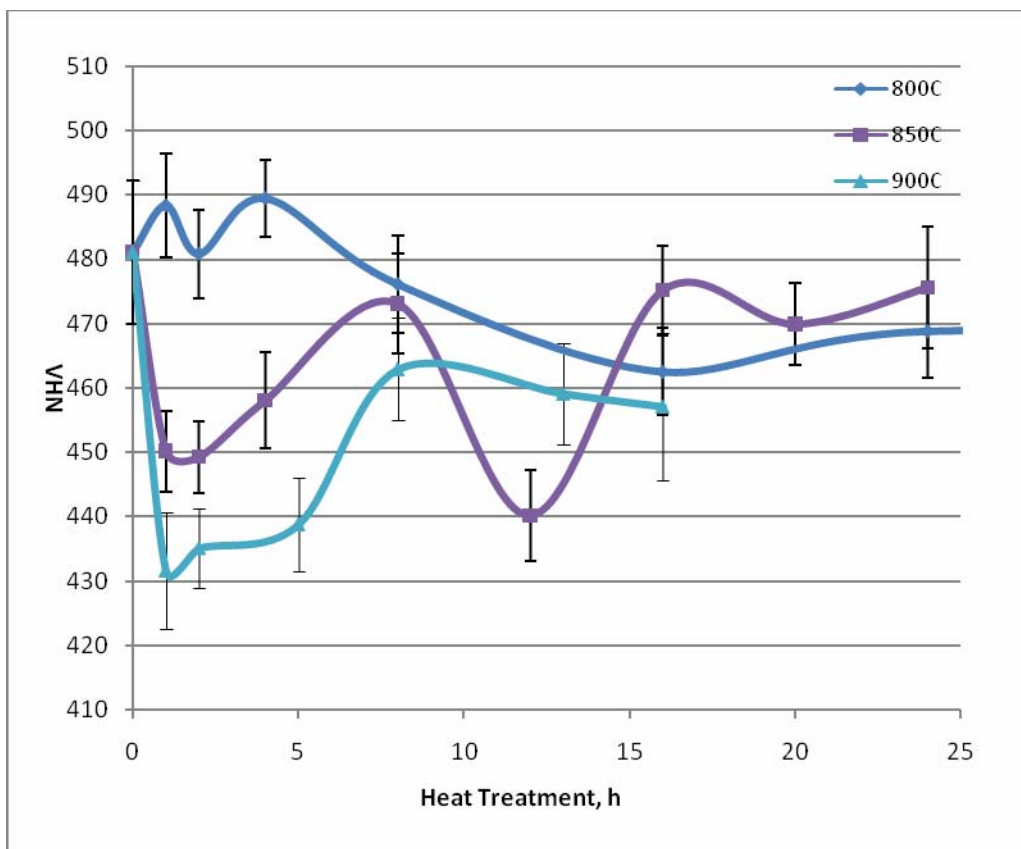


**Figure 30: Vickers Microhardness Of Rene88 DP After Heat Treatments At 800°C, 850°C, and 900°C**

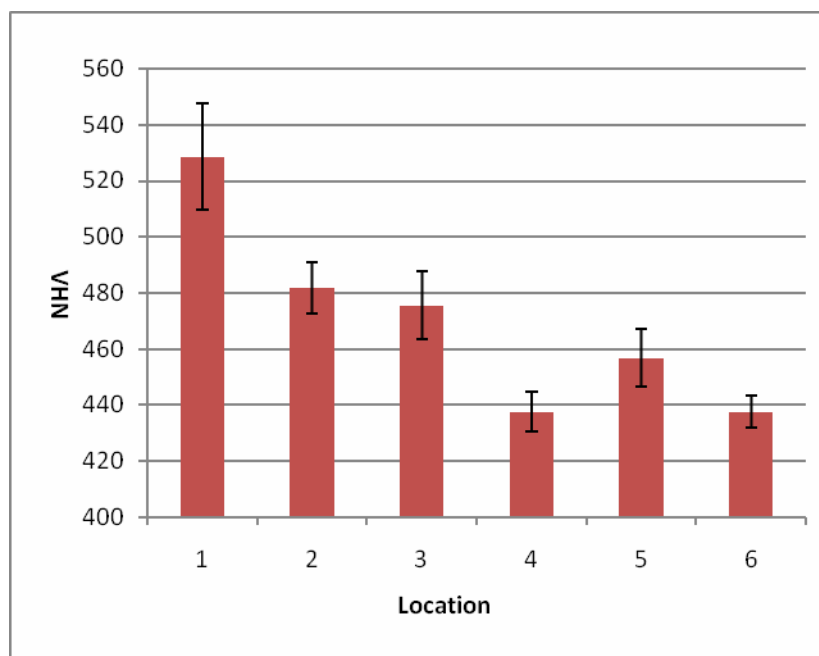


**Figure 31: Vickers Microhardness Of Rene88 DP In As-Received Condition**

As part of this effort, two sets of specimens of Rene88DP alloy were first solutionized at a slightly subsolvus temperature to avoid excessive grain growth, water quenched, and subjected to aging heat treatments at 700°C or 800°C. The results of these experiments are shown in **Figure 32**. It is apparent that the subsolvus solutionizing has not completely removed the fluctuations of microhardness between individual specimens. Another attempt was then made to solutionize the alloy at supersolvus temperatures. The microhardness of so treated specimens after aging at 700°C are shown in **Figure 33**. It is apparent that while the supersolvus solutionizing has considerably improved the consistency of the results, some fluctuations, most likely related to the residual inhomogeneities in the material properties are still apparent. However, in general the dependence of microhardness of Rene88 alloy solutionized and quenched in this manner appears suitable for sensor development.

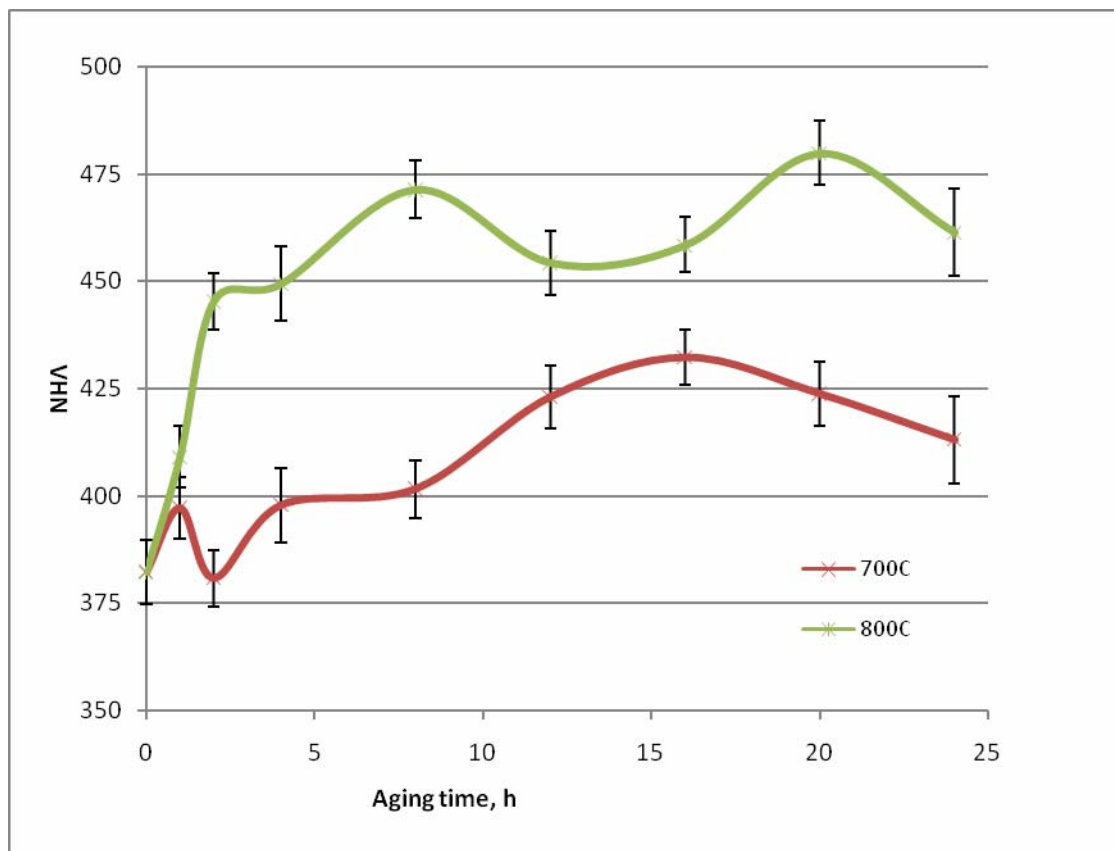


**Figure 32: Vickers Microhardness of Rene88 Solutionized At Subsolvus Temperature after Aging at 700°C and 800°C**

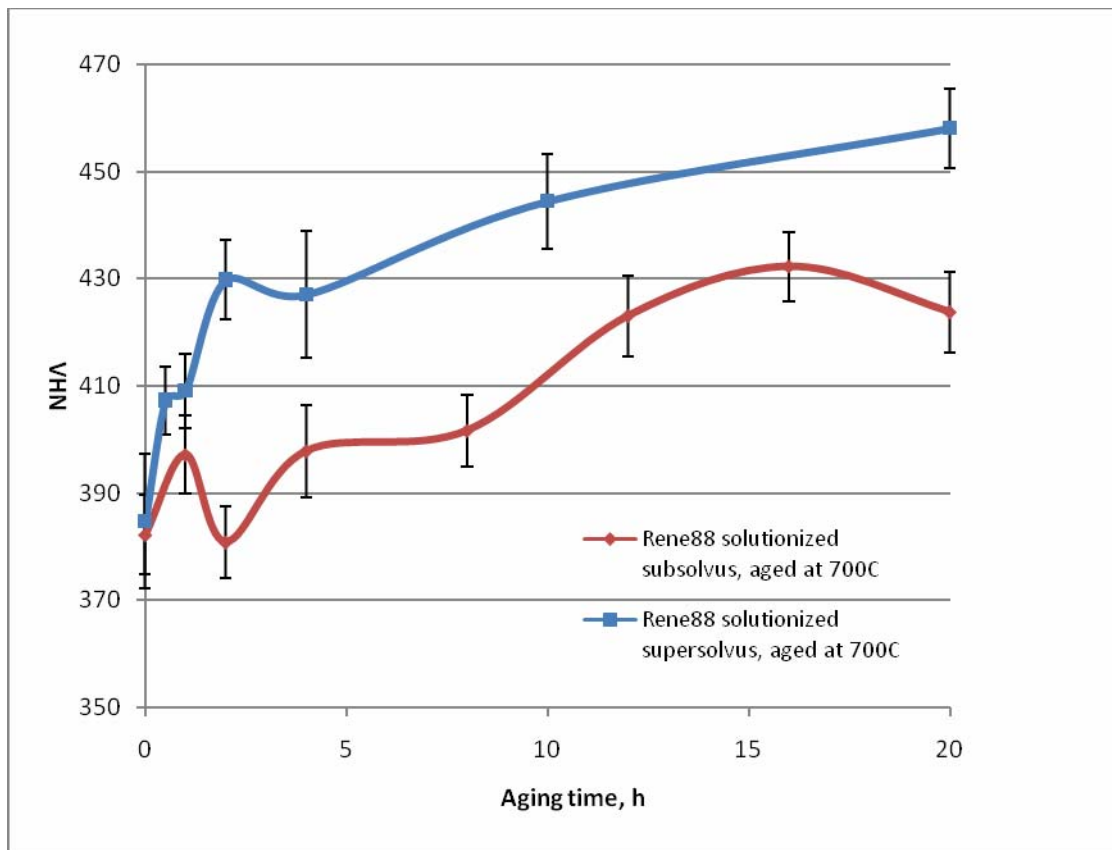


**Figure 33: Vickers Microhardness Of Rene88 Solutionized At Supersolvus Temperature after Aging At 700°C. The Data for Subsolvus Treatment Is Added For Comparison**

Further experiments were conducted with IN718 alloy. **Figure 34** shows Vickers microhardness IN718 alloy solutionized at subsolvus temperature after aging at 550°C, 650°C, and 750°C. Similar to Rene88, it is apparent that after the subsolvus solutionizing the alloy still has considerable variation of microhardness between individual samples (the fluctuations of microhardness in **Figure 34** considerably exceed the uncertainty of the microhardness measurements taken on individual specimens).

**Figure 35** shows Vickers microhardness IN718 alloy solutionized at supersolvus temperature after aging at 550°C, 650°C, and 750°C. Again, similar to Rene88, it appears that the supersolvus solutionizing has considerably improved the consistency of the results and the

dependence of microhardness of IN-718 alloy prepared in this manner may be suitable for sensor development.

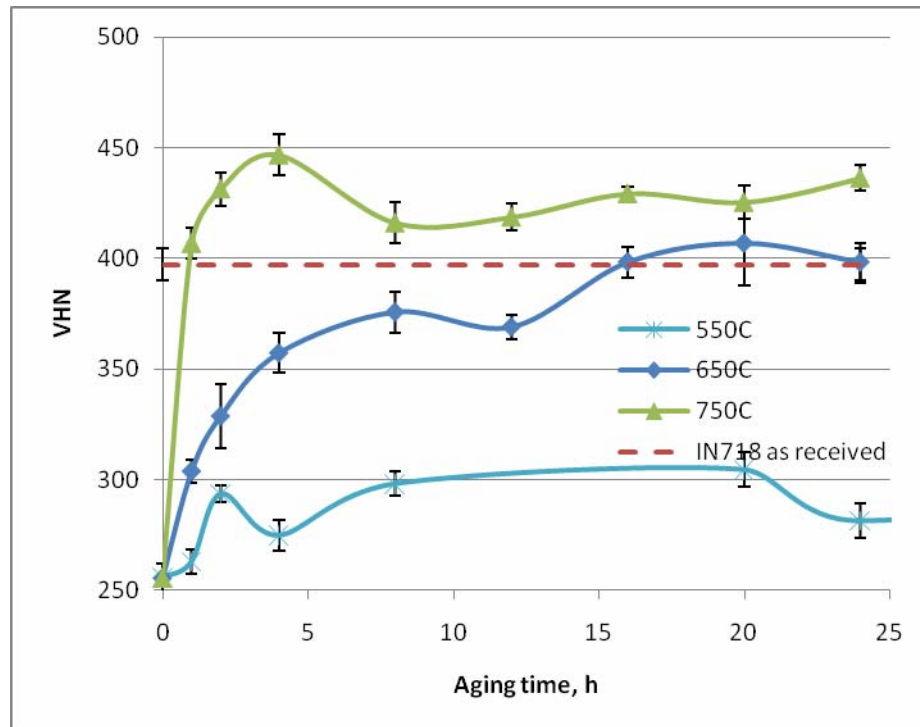


**Figure 34: Vickers Microhardness IN718 Alloy Solutionized at Subsolvus Temperature after Aging at 550°C, 650°C and 750°C**



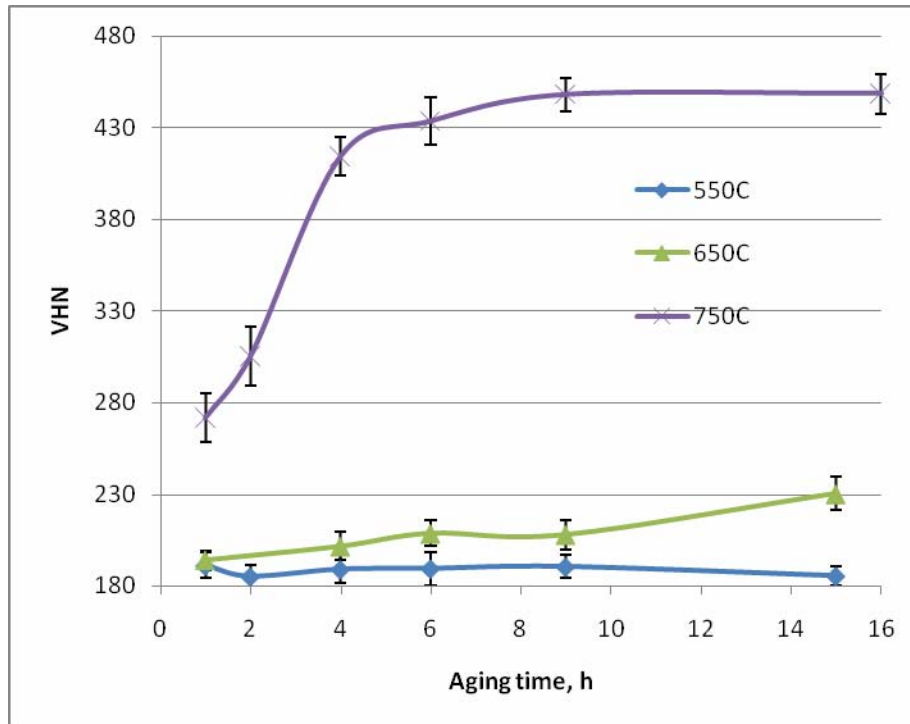


**Figure 35: Vickers Microhardness IN718 Alloy Solutionized at Supersolvus Temperature after Aging at 550°C, 650°C and 750°C**

In addition, samples of IN718 alloy that were previously aged at 700°C and used for resistivity measurements (**Figure 17**) were sectioned, and microhardness measurements were taken. **Figure 36** shows the correlation between Microhardness and resistivity of these samples. While considerable data scatter is evident, overall it can be seen that a correlation between the two properties does exist for this alloy. Indeed, many of the key factors that affect resistivity – dislocation density, residual stress, precipitate size and volume fraction, etc., are also the key factors that influence the plasticity of these alloys [13].

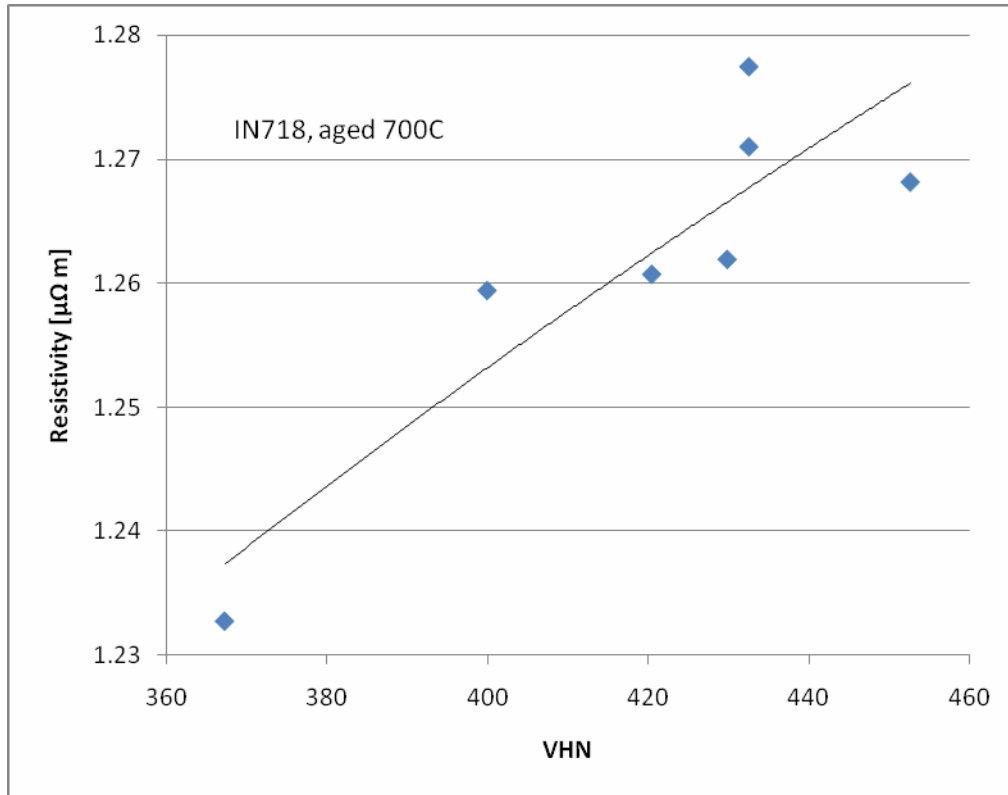


**Figure 36: Correlation Between Microhardness and Electrical Resistivity of IN718 After Aging at 700°C**

### 2.2.6. Thermal History Sensor Development

The results in **Figure 26** and **Figure 27** demonstrate that the microhardness values of the alloys selected in this study may be used to monitor the extent of thermal exposure. It was decided, therefore, to expand the temperature range of the microhardness for selected, most promising compositions. Based in the results in **Figure 26** and **Figure 27** alloys A1, A4, and A5 were selected for further investigation. Indeed, as can be observed in **Figure 26** and **Figure 27**, the alloys A1 and A4, water quenched and aged at 700°C for 2 hours, can be expected to exhibit subsequent monotonic increase of microhardness due to continuing precipitation of  $\gamma'$ . On the contrary, alloy A5, water quenched and aged at 700°C for 4 hours, can be expected to exhibit subsequent monotonic decrease of microhardness, presumably due to coarsening of  $\gamma'$  precipitates (over-aging).

Consequently, specimens of A1, A4, and A5 alloys were solutionized at 1220°C for 2 hours, water quenched, and subjected to the “initializing” aging at 700°C for 2 hours (alloys A1 and A4), or 4 hours (alloy A5). These “initialized” alloys were then designated A1-i, A4-i, and A5-i, to distinguish them from the original alloys. The “initialized” specimens were then aged at 600°C and 800°C, sectioned, polished, and the microhardness measurements were taken in the middle of the cross-section for each specimen. A minimum of 10 data-points was taken for each measurement. The results of these experiments are shown in **Figure 37**, **Figure 38**, and **Figure 39**.

As expected, the alloy A1-i exhibited monotonic increase of microhardness, with the rate of the change in microhardness increases with the increasing annealing temperature, **Figure 37**. However, given the relatively small difference between 600°C and 700°C rates, more accurate measurements would be required to reliably distinguish these two temperature regimes based on this alloy.

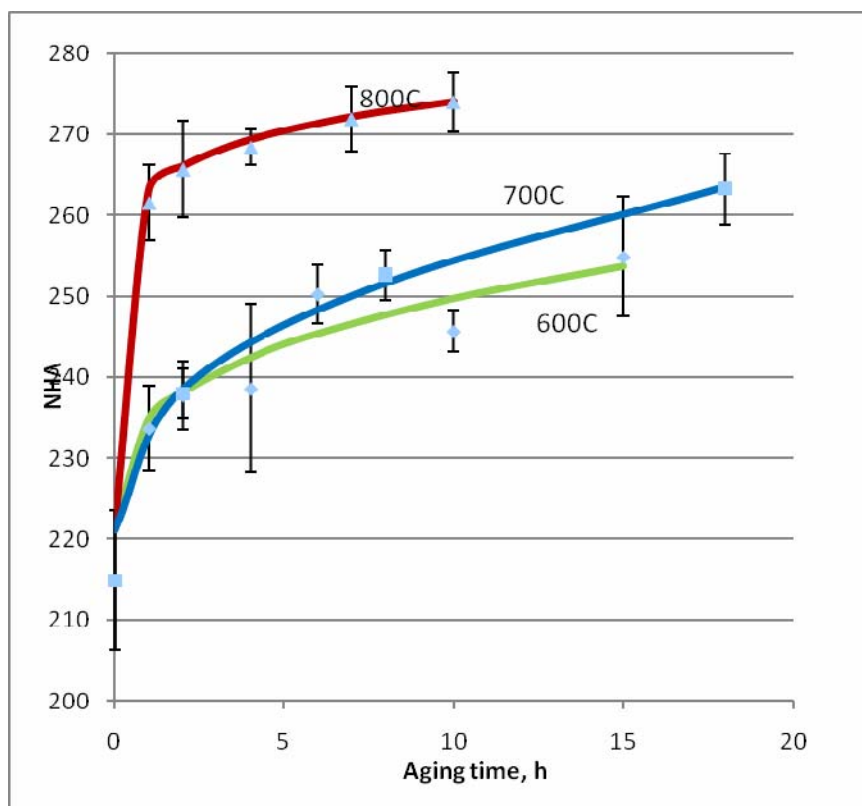


**Figure 37: Vickers Microhardness of Alloy A1-i After Aging at 600°C, 700°C, and 800°C**

A similar observation can be made regarding A5-i alloy. As expected, this alloy demonstrated the behavior typical of the over-aging regime, with a gradual decrease of microhardness with aging for all 3 temperatures, Figure 31. Once again, the rate of the change in microhardness increased with the increasing annealing temperature, though the difference between 600°C and 700°C rates was much smaller than between 700°C and 800°C. Even though better statistical data are needed to reliably distinguish between exposures to these two temperature regimes, it can be stated that together, the alloys A1-i and A5-i can be combined into a thermal history sensor that can be useful at temperatures between 600°C to 800°C. At or below 600°C the microhardness of A1-i will continue to increase (although at slower rate than at 600°C), while the microhardness of A5-i will remain the same. At 800°C, alloy A1-i has a very fast rate of microhardness increase, reaching microhardness values that they alloy would only attain at lower temperatures if exposed to much longer times (over 20 hours).

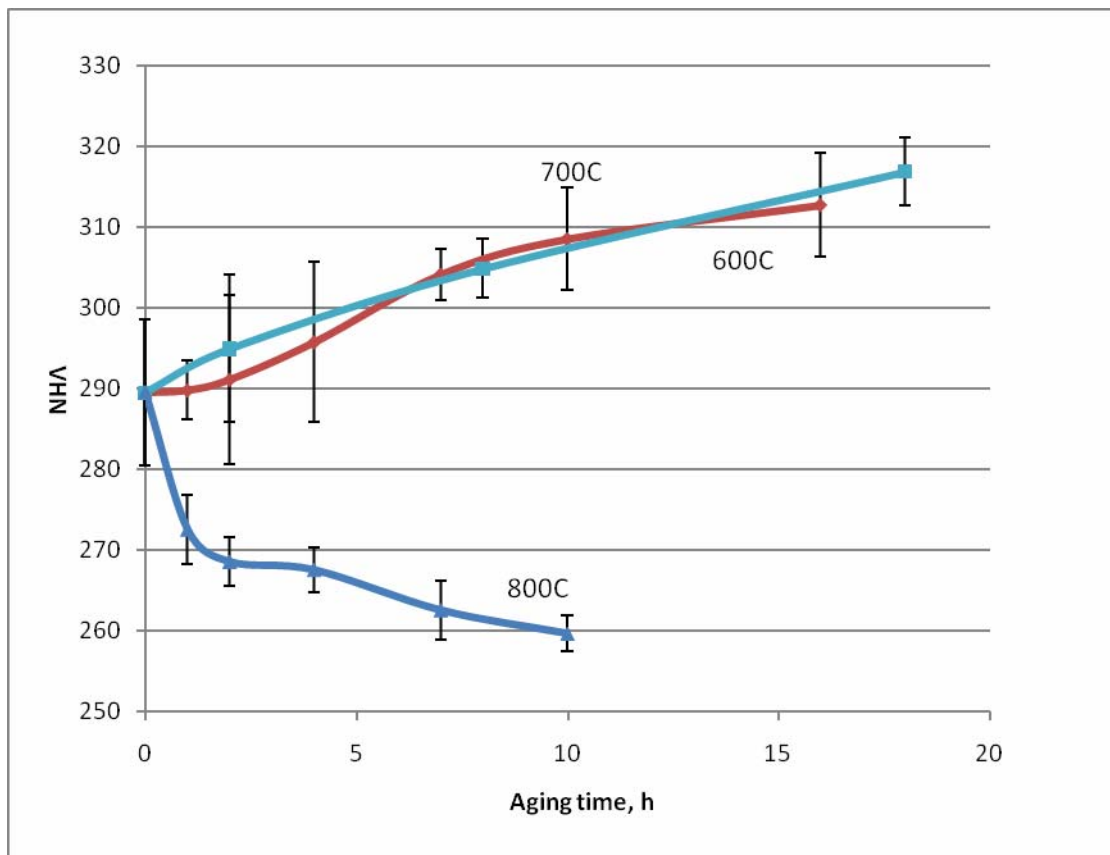


**Figure 38: Vickers Microhardness Of Alloy A4-i After Aging At 600°C, 700°C, and 800°C**

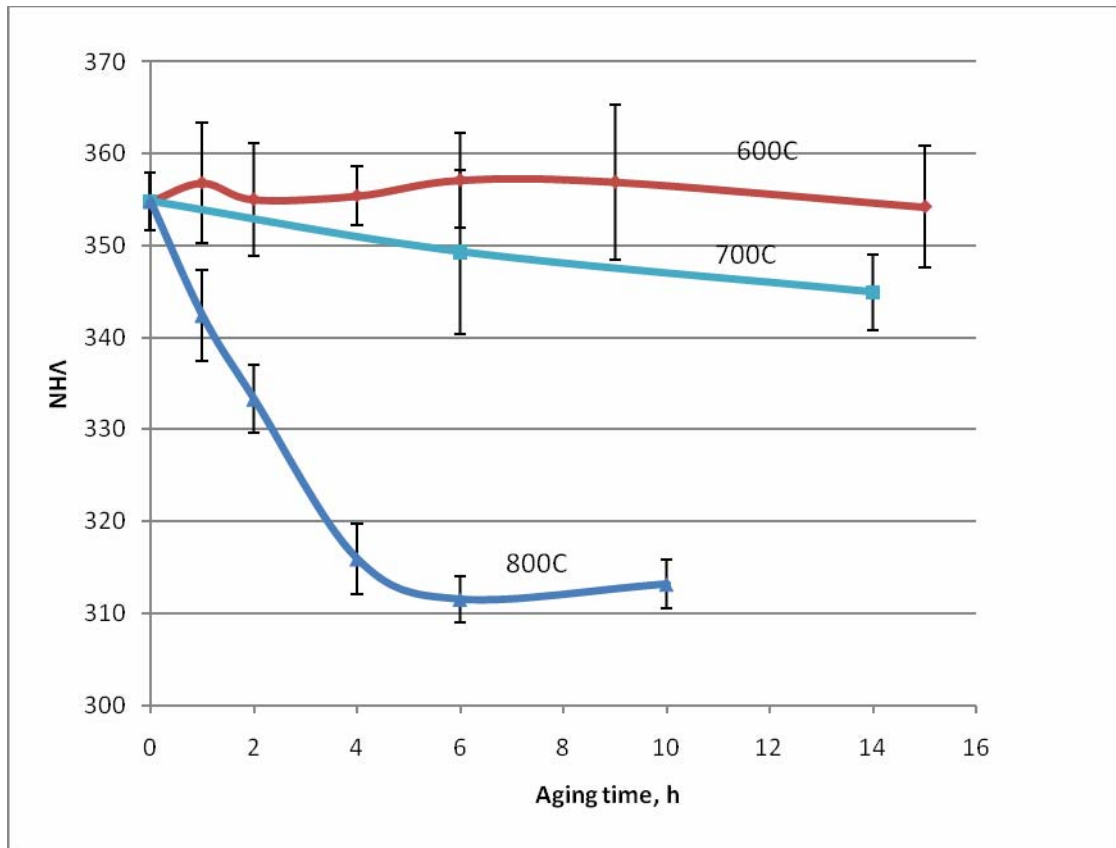


**Figure 39: Vickers Microhardness Of Alloy A5-i After Aging At 600°C, 700°C, and 800°C**

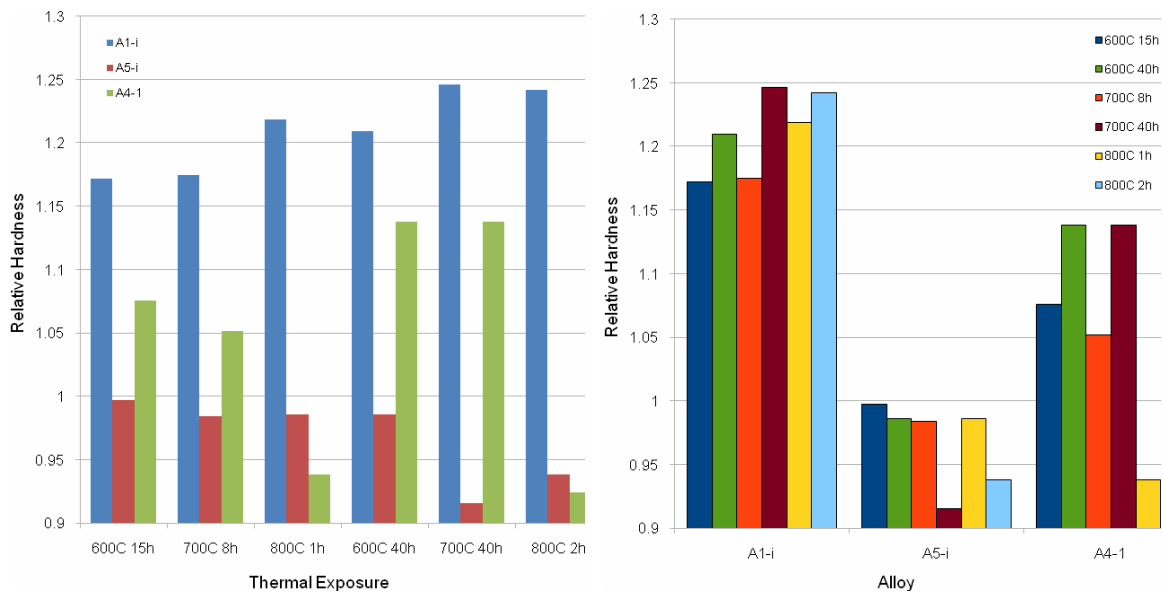


**Figure 40: Relative Microhardness Of Alloys A1-i, A4-i, and A5-i After various Thermal Exposures between 600°C and 800°C**

**Figure 40** depicts the response of a hypothetical sensor comprised of alloys A1-i, A4-i, and A5-i after various thermal exposures between 600°C and 800°C. It shows that while alloy A1-i would fail to distinguish between, for example, exposure to 600°C for 15 hours and exposure to 700°C for 8 hours, it would give a clear indication if the sensor was exposed to a short (1-2 hours) temperature spike to 800°C. At the same time, while alloy A5-i would fail to distinguish between 1 hour excursion to 800°C and 8 hours exposure to 700°C, or 40 hours exposure to 600°C, it would give a clear indication if the sensor was only exposed to a temperatures of or below 600°C or saw prolonged exposures to 700°C. Similarly, while alloy A1-i cannot distinguish between exposures to 700°C for 40 hours and 800°C for 2 hours, it can register the difference between long term (40 hours) exposures to 600°C and 700°C. On the contrary, A4-i would likely fail to distinguish between long term (40 hours) exposures to 600°C and 700°C, its response to the 800°C 2 is unique. Thus, a sensor comprised of these three alloys may have the ability to distinguish between different thermal exposure regimes that would not be distinguishable with a single alloy. In the right-hand side of **Figure 40**, these results are also shown group by alloy, making it easier to compare the response of each sensor component alloy to different thermal exposures.

It was proposed in this project, to introduce an empirical parameter similar to Larson-Miller parameter (LMP) [14] to describe the change of properties of Ni-based superalloys with time and temperature. The LMP parameter is expressed as

$$LMP = \frac{T}{1000} [B + \log(t)] \quad (2)$$

where T is the temperature in Kelvin, t is the time in hours and the parameter B is a material parameter. Many physical properties may be represented as a linear, or at least a monotonic function of LMP, provided the parameter B is chosen appropriately. Thus, assuming this is also true for microhardness of Ni-based superalloys, we can write:

$$LMP = C + D \cdot VHN \quad (3)$$

where C and D are linear fit parameters, and VHN is the Vickers hardness number. It should be noted that the form of the equation (2) does not allow one to use the initial value of the property under analysis ( $t=0$ ). To avoid this problem, the equation (3) was modified:

$$LMP = \frac{T}{1000} [B + \log(t + t_0)] \quad (4)$$

It follows that

$$\log(t_0) = \frac{1000 \cdot LMP(0)}{T} - B \quad (5)$$

The parameter  $t_0$  now can be determined for each temperature from the equations (3) and (5), and the initial value of the microhardness.

**Figure 41** shows the variation of Vickers microhardness of alloys A1-I and A5-I with LMP. The empirical LMP constant B for each alloy was optimized to achieve the best possible data convergence and linearity of the LMP vs. VHN plots, and are listed in **Table 14** along with the linearization parameters C and D. From these plots, it is clear that for these 2 alloys there is a systematic variation of the properties with LMP in the studied temperature range, which can be described by a linear dependence.

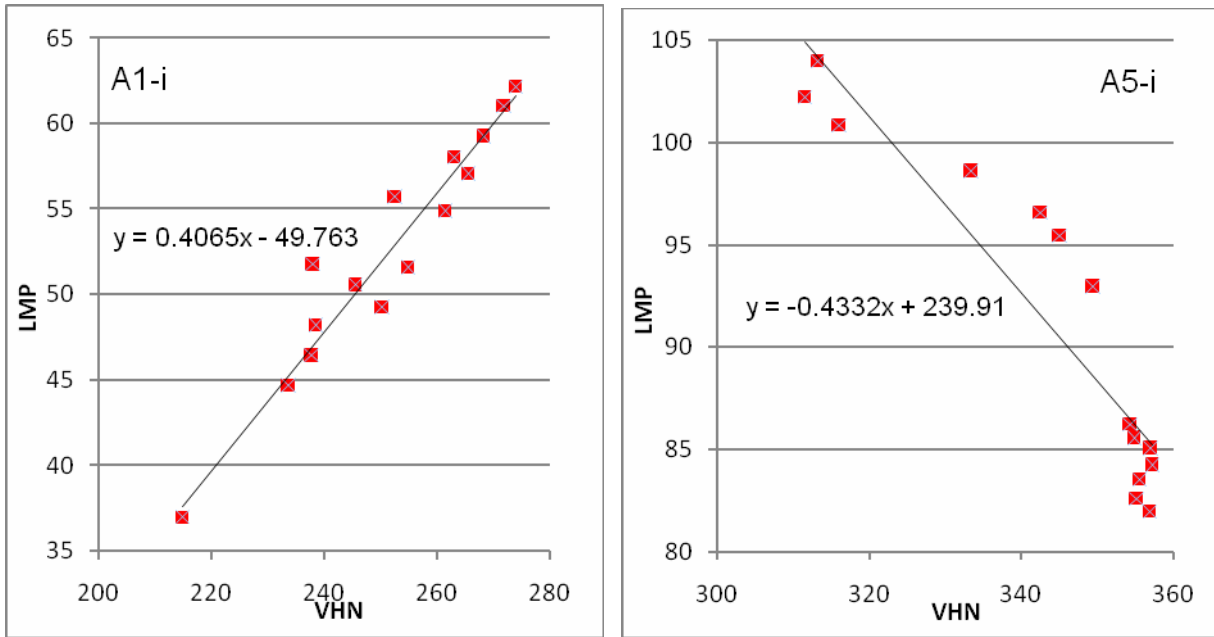


**Figure 41: LMP vs. Microhardness Plots Of Alloys A1-i and A5-i After various Thermal Exposures between 600°C and 800°C**

**Table 14: Empirical LMP Parameters A and B, and Linearization Parameters C and D for Alloys A1-i and A5-i**

Parameters		Alloy	
		A1-i	A5-i
B		7.3	11.8
C		-49.8	239.9
D		0.41	-0.43
t <sub>0</sub> , h	600°C	0.31	3.20
	700°C	0.17	0.86
	800°C	0.10	0.29

Thus, for these alloys, the LMP parameter can indeed be defined in such a manner that it becomes a simple linear function of the microhardness, and if the extent of thermal damage is defined in terms of the Larson-Miller Parameter, microhardness measurements can be used to evaluate it.

Moreover, in a sensor comprised of two different alloys, actual temperature and duration of the thermal exposures can be extracted from the microhardness measurements. Thus, if the microhardness of the two alloys  $VHN_{A1}$  and  $VHN_{A5}$  after a thermal exposure are measured, the



LMP values for each alloy,  $LMP_{A1}$  and  $LMP_{A5}$  can be obtained using equation (3) and the parameters C and D for each alloy, **Table 14**. Hereafter, the effective temperature and time of the thermal exposure can be evaluated by plotting equations (4) for each alloy using the LMP parameters B and  $t_0$  listed in **Table 14**. An example of such evaluation is shown in **Figure 42**. The curves in the left plot in **Figure 42** were calculated for  $VHN_{A5i} = 330$  and  $VHN_{A5i} = 265$ , which correspond to the thermal exposure to  $\sim 750^\circ\text{C}$  for  $\sim 7.5$  hours. The curves in the right plot were calculated for  $VHN_{A5i} = 355$  and  $VHN_{A5i} = 245$ , which correspond to the thermal exposure to  $\sim 605^\circ\text{C}$  for  $\sim 7$  hours. Finally, the bottom plot was calculated for  $VHN_{A5i} = 330$  and  $VHN_{A5i} = 262$ , which correspond to the thermal exposure to  $\sim 775^\circ\text{C}$  for  $\sim 3$  hours.

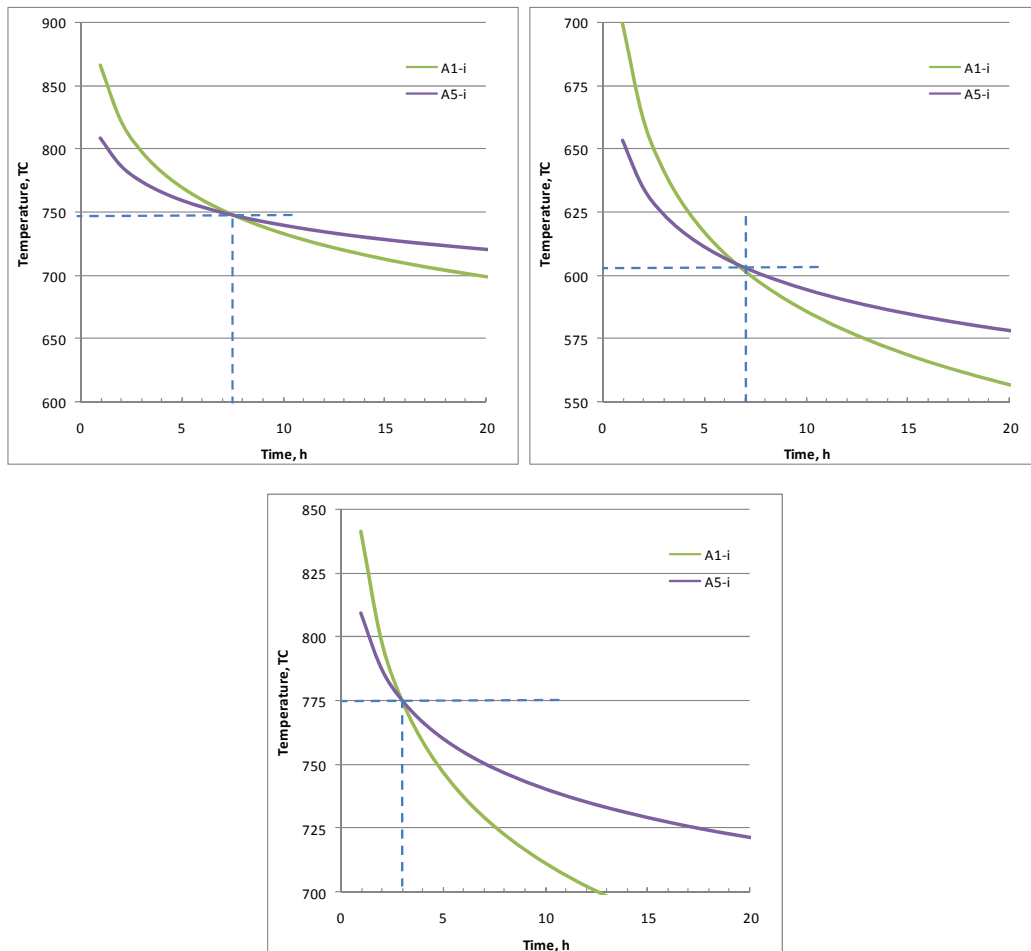


**Figure 42: Evaluation of Thermal Exposure From The Microhardness Of Alloys A1-i and A5-I Using Larsen-Miller Parameter**

An attempt was also made to apply similar approach to the microhardness data obtained for IN-718 alloy solutionized at supersolvus temperature after aging at 550°C, 650°C and 750°C (**Figure 35**). However, for this alloy it was not possible to optimize LMP parameter B such that the data points would converge into a linear dependence of LMP on VHN. However, it was possible to find B such that all data would form a logarithmic LMP vs. VHN plot, **Figure 43**.

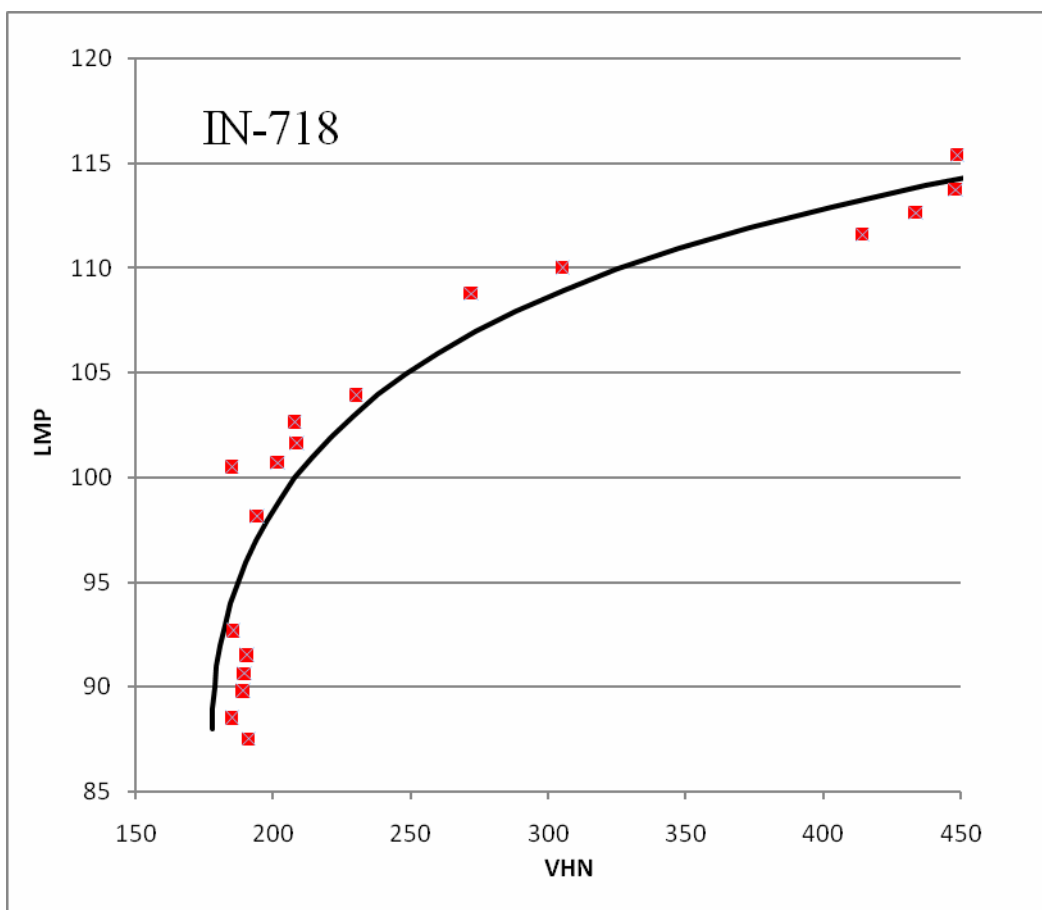


**Figure 43: LMP vs. Microhardness Plots for IN-718 Alloy After various Thermal Exposures between 550°C and 750°C**

It should be emphasized that for the approach being proposed in this study, a linear dependence of LMP on VHN (or other properties being monitored) is not essential. What is important, however, that this dependence is known and provides a unique correlation between the property being measured (in this case, microhardness), and LMP, such that the value of LMP can always be obtained from the characteristic LMP vs. property plot for the particular alloy. With that in

mind, one can say that the LMP vs. VHN for IN-718 alloy prepared in this particular way, can be used in this approach for  $VHN > 200$ , where reliable reading of LMP can be obtained from the VHN values. The empirical parameter B for IN-718 alloy was  $B=15$ .

Thus, it has been demonstrated that this approach based on the physical properties of alloys (in this case microhardness values) is, indeed, a useful method to assess the extent of thermal damage defined through a Larson-Miller Parameter, as well as evaluate details of actual thermal history, such as duration and temperature of thermal exposure.

### **2.2.7. In Situ Aging and Room Temperature Resistivity Measurements Of Water Quenched Alloys**

In view of the results obtained in the previous sections, it has become apparent that the alloys under investigation do possess a promising potential for use as a thermal history sensor. Consistent and controlled variations of microhardness with aging time were observed. Also, as expected, the kinetics of precipitation in arc-melted Ni-Al-Ti and Ni-Al-Cr alloys was a function of the Al content. Promising results were also obtained with commercial alloys, although large variability in the initial microhardness in the commercial alloys was still a considerable obstacle. It was decided, therefore, to attempt another series of electrical resistivity measurements on alloys A1, A2, A4, and A5. To minimize the possible effect of varying cooling rates during quenching and compositional changes in the surface regions of the specimens during high temperature annealing, all samples were initially cut to identical size, homogenized at  $1220^{\circ}\text{C}$  for 60h, and water quenched. Similar to the previous section, the quenched samples were then subjected to the “initializing” aging at  $700^{\circ}\text{C}$  for 2 hours (alloys A1, A2, and A4), or 4 hours (alloy A5) to remove the thermal stress. The specimens were then additionally ground to remove a  $500\text{ }\mu\text{m}$  surface layer that might have been affected chemically or microstructurally by the high temperature heat treatment. Similar to the previous section, the “initialized” alloys were designated A1i, A2i, A4i, and A5i, to distinguish them from the original alloys.

The samples were then subjected to thermal cycling to temperatures  $600^{\circ}\text{C}$ ,  $700^{\circ}\text{C}$ , and  $800^{\circ}\text{C}$ . The ramp up and ramp down rates were constant at  $300^{\circ}\text{C}/\text{hour}$  and the holding time was also

fixed at 5 hours. The full duration of each thermal cycle, therefore, including the temperature ramps and the soak time ranged from ~8.9 to 10.5 hours, depending on the target temperature. During the experiments, the furnace was continuously purged with flowing at 0.9 liter/min. For each experiment, room temperature electrical resistivity measurements were simultaneously collected on 2 specimens of each alloy. The results of these experiments are presented in **Figure 44** and **Figure 45**.

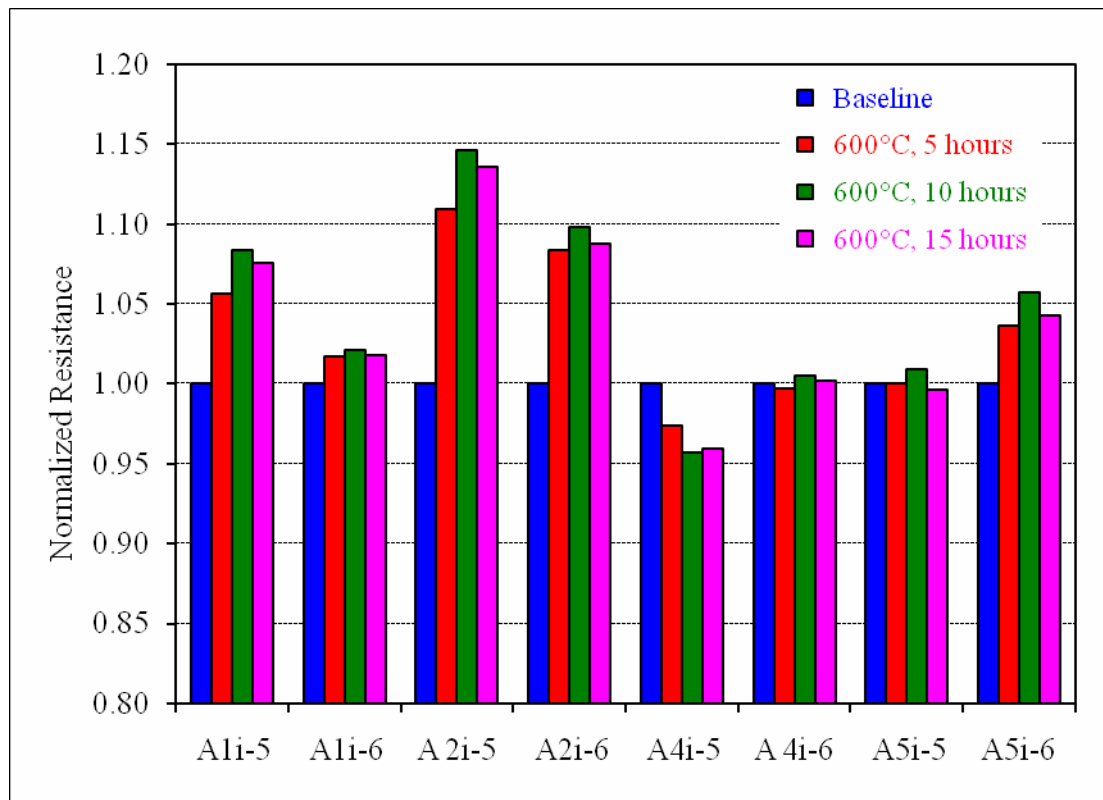


**Figure 44: Normalized Room Temperature Resistance of Alloys A1i, A2i, A4i and A5i After Thermal Cycling at 600°C, 700°C, and 800°C**

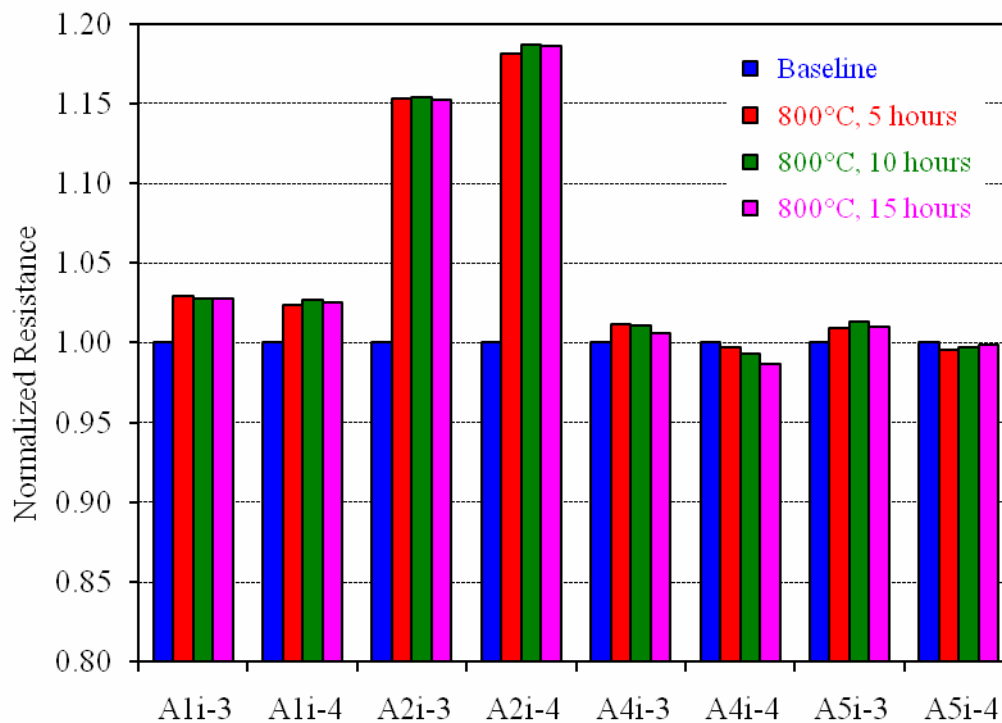
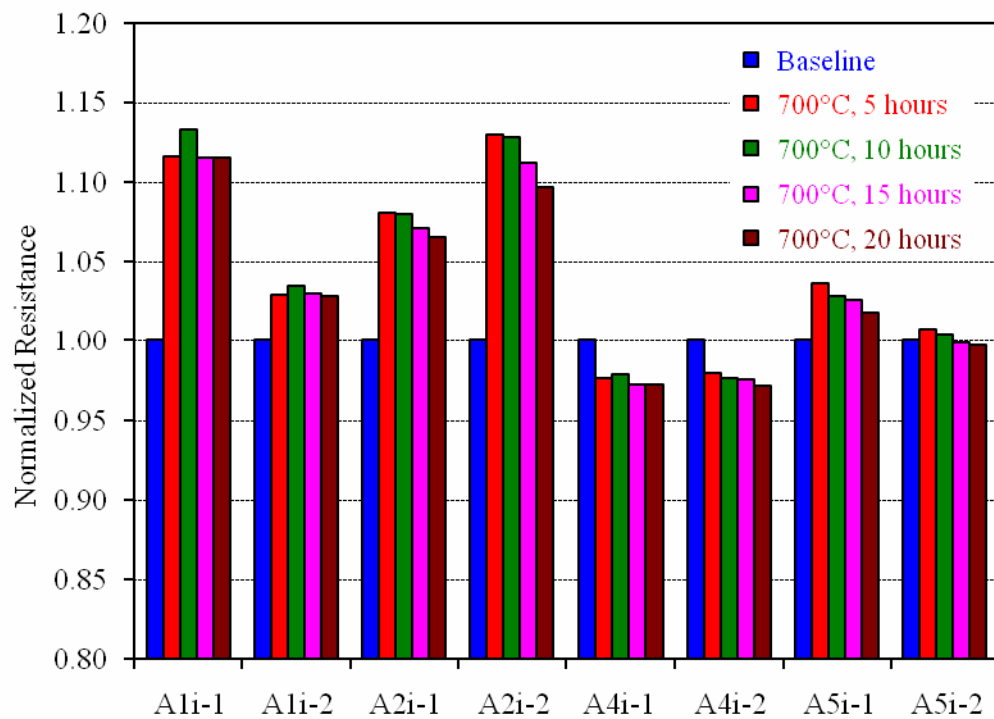


**Figure 44 (Continued).**

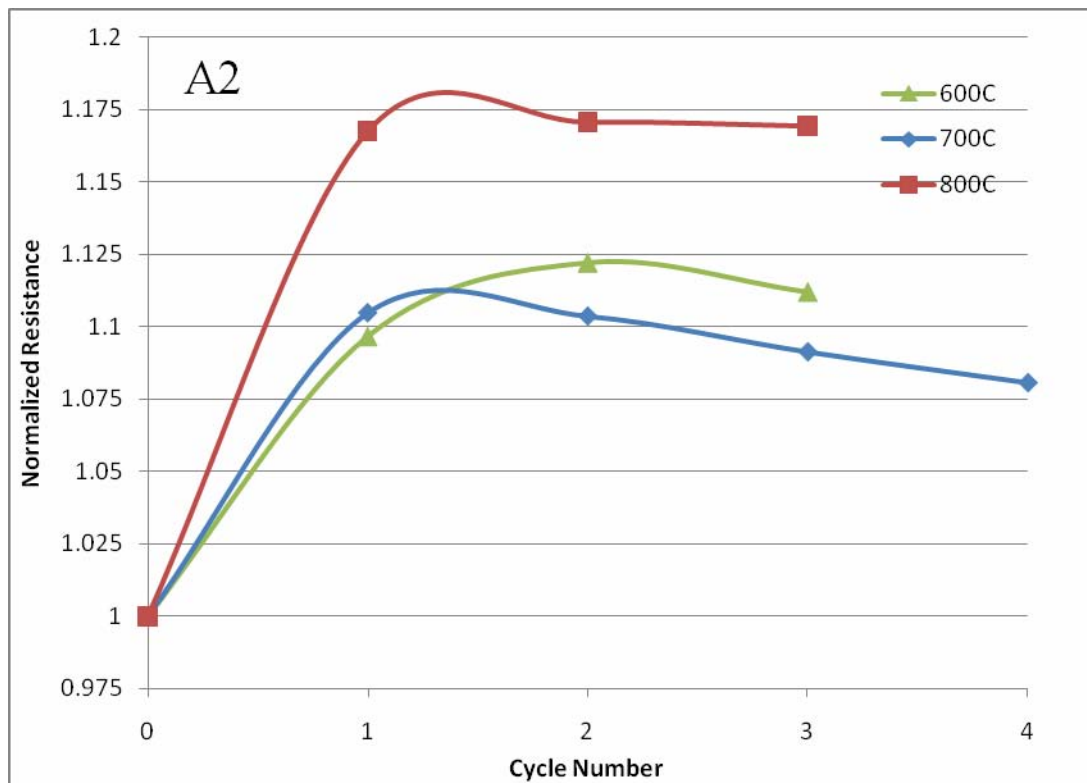
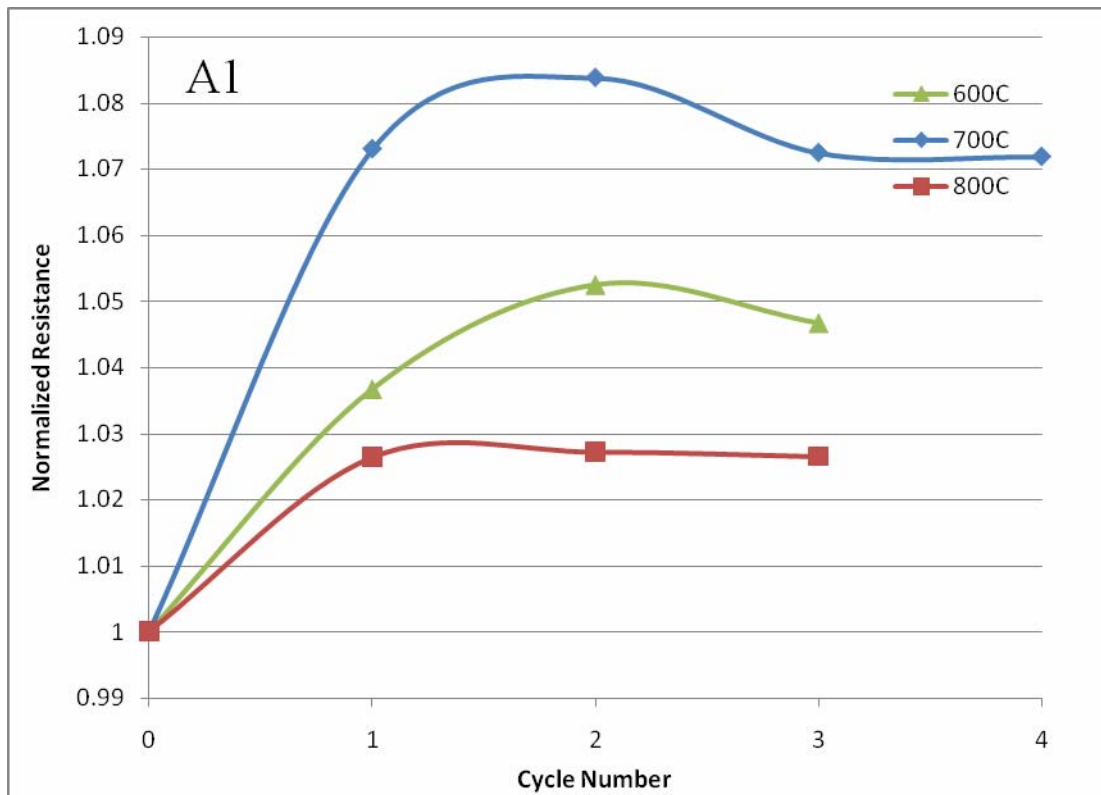


**Figure 45: Average Normalized Average Room Temperature Resistivity of Alloys A1i, A2i, A4i and A5i vs. Cycle Number at 600°C, 700°C, and 800°C**

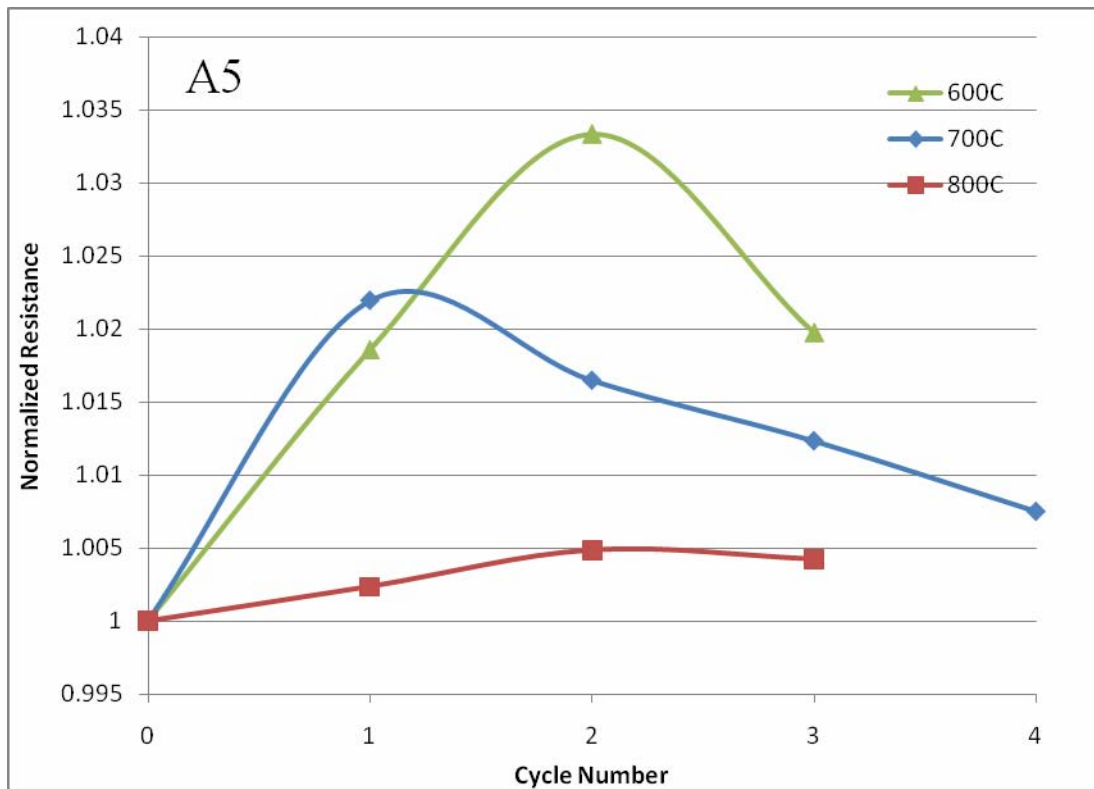
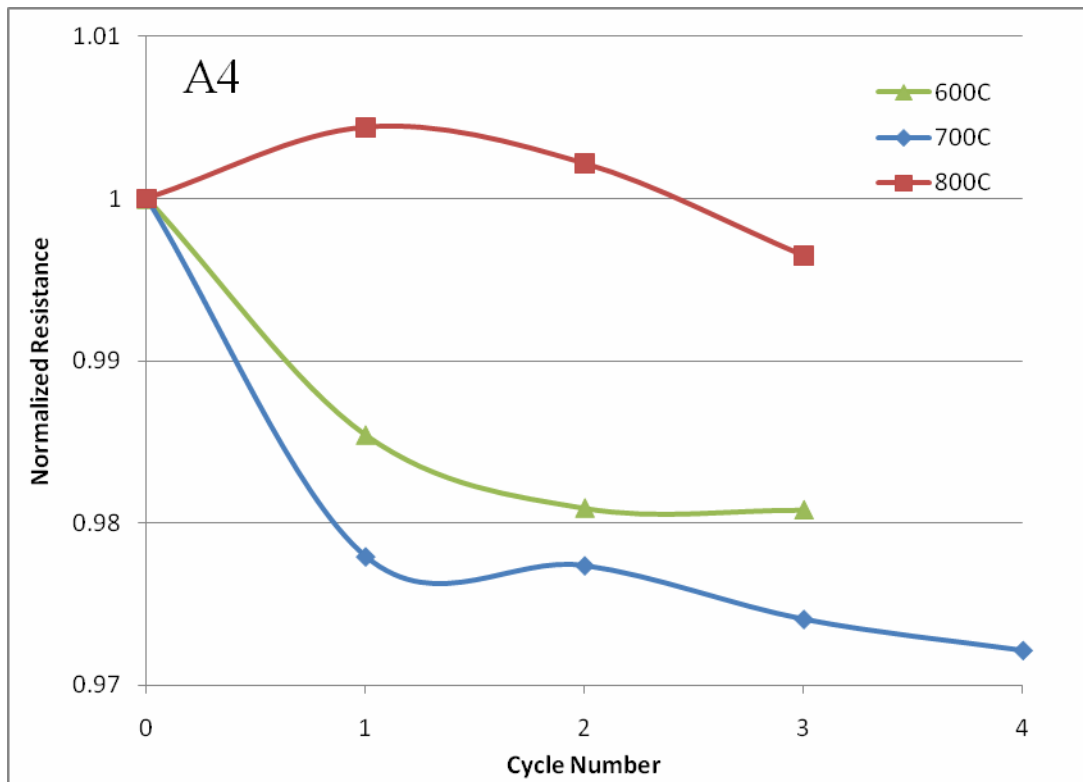


Figure 45 (Continued)

These results indicate that even though in some cases there is a relatively large difference between the response of 2 samples of each alloy tested in these experiments, the trends are generally consistent. Alloys A1i and A2i demonstrated particularly strong variation of resistivity (up to ~13% and ~19%, respectively), while alloys A4i and A5i had up to ~4% and ~6% variation in resistivity, respectively, depending on thermal exposure. It should be noted here, that the method employed to measure the resistivity has very high precision. In the course of these experiments, each sample after each thermal exposure was measured repeatedly four times, the standard deviation between the four measurements never exceeding 0.02%, in most cases being 0.01%. Therefore, even ~4-6% change in resistivity of alloys A4i and A5i could be detected with high accuracy and reliability, and in principle would be enough for sensing applications. The most important issue, however, is to ensure that the alloys are homogeneous and have very strictly controlled composition and initial microstructure, to eliminate the large effects these parameters have on the thermal response of their resistivity. Thus, it is clear from **Figure 44** that even though the response of the individual alloys, especially A1i and A2i, to thermal cycling at 600°C, 700°C and 800°C was qualitatively consistent at all temperatures, quantitatively the variation was sometimes considerably different between two samples tested under identical conditions. For example, among the two A1i specimens tested at 600°C, one had ~8% increase in resistivity after the second cycle, while the other only ~2%. At 700°C, one of the A1i specimens had ~13% increase in resistivity after the second cycle, while the other only ~3%. Similarly, among the two A2i specimens tested at 600°C, one had ~15% increase in resistivity after the second cycle, while the other only ~10%. At 700°C, one of the A2i specimens had ~8% increase in resistivity after the second cycle, while the other had ~13%. Without significantly tightening the margins of compositional and microstructural variations in the initial alloys, to ensure statistically sound results would require very large number of specimens, not only during the research and development cycle, but in the practical use as well. While during the R&D stage this may simply be extremely, perhaps impractically, time and resource consuming, for the service application it would be not just impractical, but definitely prohibitive.



### 3. CONCLUSIONS AND SUMMARY

The effect of thermal exposure on electrical resistivity and microhardness of six model alloys from the Ni-Al-Ti and Ni-Al-Cr systems, as well as two commercial Ni-based superalloys IN-718 and Rene88, was systematically studied in order to evaluate the possibility of using these alloys and their physical properties for the development of thermal history sensor based on transformation-induced property changes in Ni-based alloys.

Based on the experimental results presented, a thermal history sensor, operating on the principle that sensitive variations in microhardness and/or electrical conductivity accompany microstructural changes in Ni-Ni<sub>3</sub>Al-based alloys, has been demonstrated. The operation of such sensor is based on the established correlation between physical properties, such as microhardness and /or electrical resistivity, and the material damage parameter, expressed in the form of Larson-Miller Parameter (LMP). Thus, measuring microhardness and/or electrical resistivity of an alloy, one can get a measure of the incurred material damage, expressed through appropriately defined LMP. From the characteristic LMP vs. property plot for the particular alloy, one can read the value of LMP, and knowing the exposure time, the equivalent temperature experienced at each location can be calculated. Furthermore, it has been demonstrated that with a sensor comprised of two different alloys, the equivalent temperature and duration of the thermal exposures can be extracted independently from the microhardness data.

Thus, it has been demonstrated that this approach based on the physical properties of alloys (in this case microhardness and/or electrical resistivity) is a useful method to assess the extent of thermal damage defined through a Larson-Miller Parameter, as well as evaluate details of actual thermal history, such as duration and temperature of thermal exposure.

The most critical issue for the practical development of a sensor based on this principle is to ensure the structural and compositional homogeneity of the alloys used in the sensor. The problem stems from the fact that the high sensitivity of the chosen physical properties (microhardness and electrical resistivity) to thermal exposure, which is essentially a prerequisite

for their use in a thermal history sensor, comes at a price of their extreme sensitivity to the alloys composition and initial microstructure. The single biggest obstacle during this project was the difficulty to ensure sufficient homogeneity of the alloys used in the course of the study. This applied equally to the model alloys prepared by arc melting specifically for this project, and to specimens of engine-grade commercial alloys as well.

The assurance of the chemical and metallurgical homogeneity of the samples in the initial state is a key attribute to extend this approach to a practical application. A process that yields such homogeneity will need to be identified. Thin film deposition techniques, plasma spray coating methods, laser deposition followed by well defined heat treatment are some processes that are suggested, since samples of small thicknesses will likely be much more uniform than bulk processed materials. Second, use of multiple sensors, by varying chemistries and heat treatments will help eliminate errors in measurement and eliminating multiple time-temperature combinations as possible solutions for a given thermal profile.

## REFERENCES

1. R. Graue, A. Reutlinger and J. Werner, "TPS Health Monitoring on X-38," *Proceedings of SPIE* **3668** (1999) 278-284.
2. R. Ikegami and E. D. Haugse, "Structural health management for aging aircraft," *Proceedings of SPIE* Vol. **4332** (2001) 60-67.
3. R. S. Fielder and K. L. Stinson-Bagby, "High-Temperature Fiber Optic Sensors for Harsh Environment Applications," *Proceedings of SPIE* Vol. **5272** (2004) 190.
4. Z. Huang, W. Peng, J. Wu, G. R. Pickrell and A. Wang, "Fiber temperature sensor for high-pressure environment," *Optical Engineering*, **44** (2005) 104401
5. A. Roberts, R. May, G. Pickrell and A. Wang, "High-temperature optical fiber instrumentation for gas flow monitoring in gas turbine engines," *Proceedings of SPIE* Vol. **4578** (2002) 210-219.
6. T. Hao, F-S. Zhou, X-Q Xie, J-W Hu and W-Y Wang, "Fiber optic high-temperature sensor for applications in iron and steel industries," *Proceedings of SPIE* Vol. **1584** (1991) 32-38.
7. M.P. Jackson, M.J. Starink, and R.C. Reed, "Determination of the precipitation kinetics of Ni<sub>3</sub>Al in the Ni-Al system using differential scanning calorimetry," *Mat. Sci. Eng A* **264** 26-38 (1999)
8. C.K. Sudbrack, K.E. Yoon, R.D. Noebe, and David N. Seidman "Temporal evolution of the nanostructure and phase compositions in a model Ni-Al-Cr alloy," *Acta Materialia* **54** (2006) 3199-3210
9. V.A. Antropov et al., Magnetic susceptibility and electrical resistivity of Ni-Al alloys at high temperatures, *Russian Physics Journal* **25** 208-212 (1982)
10. C. Slama, C. Servant, and G. Cizeron, "Aging of the Inconel 718 Alloy Between 500 and 750°C," *J. Mater. Res.*, **12** 2298-2316 (1997)
11. G.V. Samsonov (Ed.) in *Handbook of the physicochemical properties of the elements*, IFI-Plenum, New York, USA, 1968.

12. W. WANG and K. LU, "Nanoindentation Measurement of Hardness and Modulus Anisotropy in  $\text{Ni}_3\text{Al}$  Single Crystals," *Journal of Materials Research* **17** 2314-2320 (2002)
11. P. Mogilevsky, T.A. Parthasarathy, and M.D. Petry, "Anisotropy in Room Temperature Deformation and Fracture of  $\text{CaWO}_4$  Scheelite", *Acta Materialia*, **52**, 5529-5537 (2004).
12. P. Mogilevsky and T. A. Parthasarathy, "Anisotropy in Room Temperature Microhardness and Indentation Fracture of Xenotime," *Materials Science and Engineering A* **454-455** 227-238 (2007).
13. T A Parthasarathy, S Boone, S I Rao, P Wang, P. Nagy, and M Blodgett, "Investigation of microstructural effects on electrical resistivity and their implications for Eddy Current methods in measuring residual stress in IN718," Aeromat 2009, June 7-11, 2009, Dayton, OH USA.
14. Larson, F.R. and Miller, J.: "A Time-Temperature Relationship for Rupture and Creep Stresses," *Trans. ASME*, **74** 765-775 (1952).